# THE SYNTHESIS OF ZINC, CHLORIDE AND FLUORIDE DOPED NANO HYDROXYLAPATITES BY PRECIPITATION METHOD AND INVESTIGATION OF THEIR MECHANICAL, STRUCTURAL AND BIOLOGICAL PROPERTIES

A THESIS SUBMITTED TO
THE GRADUATE SCHOOL OF NATURAL AND APPLIED SCIENCES
OF
MIDDLE EAST TECHNICAL UNIVERSITY

BY

IDIL UYSAL

IN PARTIAL FULLFILLMENT OF THE REQUIREMENTS
FOR
THE DEGREE OF MASTER OF SCIENCE
IN
BIOMEDICAL ENGINEERING

JULY 2011

Approval of the thesis:

**THE SYNTHESIS OF ZINC, CHLORIDE AND FLUORIDE DOPED NANO HYDROXYLAPATITES BY PRECIPITATION METHOD AND INVESTIGATION OF THEIR MECHANICAL, STRUCTURAL AND BIOLOGICAL PROPERTIES**

submitted by **İDİL UYSAL** in partial fulfillment of the requirements for the degree of **Master of Science in Biomedical Engineering Department, Middle East Technical University** by,

Prof. Dr. Canan Özgen _____
Dean, Graduate School of **Natural and Applied Sciences**

Prof. Dr. Semra Kocabıyık _____
Head of Department, **Biomedical Engineering**

Assoc. Prof. Dr. Zafer Evis _____
Supervisor, **Engineering Sciences Dept., METU**

Prof. Dr. Feride Severcan _____
Co-supervisor, **Biological Sciences Dept., METU**

**Examining Committee Members**

Prof. Dr. Sevgi Haman Bayarı _____
Secondary Science and Mathematics Education Dept., HU

Assoc. Prof. Dr. Zafer Evis _____
Engineering Sciences Dept., METU

Prof Dr. Feride Severcan _____
Biological Sciences Dept., METU

Assoc. Prof. Dr. Ayşen Tezcaner _____
Engineering Sciences Dept., METU

Assist. Prof. Dr. Senih Gürses _____
Engineering Sciences Dept., METU

**Date: 21.07.2011**

**I hereby declare that all information in this document has been obtained and presented in accordance with academic rules and ethical conduct. I also declare that, as required by these rules and conduct, I have fully cited and referenced all material and results that are not original to this document.**

Name, Last name: İdil Uysal

Signature:

# ABSTRACT

THE SYNTHESIS OF ZINC, CHLORIDE AND FLUORIDE DOPED NANO HYDROXYLAPATITES BY PRECIPITATION METHOD AND INVESTIGATION OF THEIR MECHANICAL, STRUCTURAL AND BIOLOGICAL PROPERTIES

UYSAL, İdil
M. Sc., Department of Biomedical Engineering
Supervisor: Assoc. Prof. Dr. Zafer EVİS
Co-Supervisor: Prof. Dr. Feride SEVERCAN

July 2011, 158 pages

This study aimed synthesizing hydroxylapatite (HA) and $Zn^{2+}$, $F^-$ and $Cl^-$ doped HA by solution precipitation method. The synthesized compounds were sintered at 1100°C for 1h. For structural characterization, density of the samples were measured by Archimedes' method. It was observed that $Zn^{2+}$ addition increased the density significantly whereas $F^-$ caused a decrease and $Cl^-$ increased the density with a little amount. XRD was applied to the samples and it was found that co-doping of $Zn^{2+}$ and $F^-$ ions decreased the unit cell volume of HA with $F^-$ addition. Other compositions gave fluctuated results in terms of unit cell volumes. HA phase and a little amount of CaO phase were detected in some samples. FTIR spectroscopy was used to detect whether $Zn^{2+}$, $F^-$ and $Cl^-$ ions were incorporated to the HA structure or not by observing the bands corresponding to the bonds in the molecules. The amount of addition was also detected by FTIR. Results showed that ion incorporation to the HA structure was done successfully. SEM images were

analyzed and grain sizes of samples were calculated by Rietvelt analysis. Grain sizes of the samples increased by $Cl^-$ addition and decreased by $Zn^{2+}$ and/or $F^-$ addition. For mechanical characterization, Vickers microhardness test was applied. Fracture toughness was calculated from Vickers microhardness results. According to the results, the highest microhardness values were found for $F^-$ and $Zn^{2+}$ co-doped samples. It was also shown that fracture toughness decreased by $Zn^{2+}$ addition. However, $Zn^{2+}$ and $F^-$ co-doped samples gave higher fracture toughness results when compared with pure HA. $Cl^-$ addition also decreased the fracture toughness. The best compositions in terms of structural and mechanical properties was chosen as Zn2+ and F- co-doped samples and biological characterization was applied to these samples. Saos-2 cell line was used in biological examinations. For biological characterizations, Alamar Blue™ assay to detect viability and alkaline phosphatase activity (ALP) assay to detect differentiation were done. It was observed that 2 mol.% $Zn^{2+}$ addition increased the cell viability and alkaline phosphatase activity. 1 mol.% $F^-$ addition also improved cell viability and alkaline phosphatase activiy. SEM images were analyzed to observe the morphology of the cells on HA and selected doped HA discs. In accordance with Alamar Blue™ assay and alkaline phosphatase activity assay, cells showed dendritic shapes on 2 Zn and 2 Zn 1 F sample which was the indicator of good material-cell interaction. Dissolution test was also applied by immersing the samples in simulated body fluid (SBF). pH change and SEM images for $Ca^{2+}$ deposition were investigated. Increase in pH change with time was observed. $F^-$ included samples gave the lowest pH change results, especially 2 Zn 1 F. Dissolution pits and some apatitic formations were observed in SEM images.

**Keywords:** Nano Hydroxylapatite, Fluoride, Zinc, Chloride, Structural Properties, Microhardness, Biocompatibility.

# ÖZ

ÇÖKTÜRME YÖNTEMİ İLE ÜRETİLMİŞ ÇİNKO, FLOR VE KLOR İYONLARI İLAVE EDİLMİŞ NANO HİDROKSİLAPATİTLERİN MEKANİK, YAPISAL VE BİYOLOJİK ÖZELLİKLERİ AÇISINDAN İNCELENMESİ

UYSAL, İdil
Yüksek Lisans, Biyomedikal Mühendisliği
Tez Yöneticisi: Doç. Dr. Zafer EVİS
Yardımcı Tez Yöneticisi: Prof. Dr. Feride SEVERCAN

Temmuz 2011, 158 sayfa

Bu çalışma hidroksilapatit'in (HA) ve $Zn^{2+}$, $F^-$, $Cl^-$ eklenmiş HA'in çöktürme yöntemi ile sentezlenmesini amaçlamaktadır. Sentezlenen bileşikler 1100°C'de 1 saat süre ile sinterlenmiştir. Yapısal özelliklerin belirlenmesi için örneklerin yoğunlukları Arşimet yöntemi ile ölçülmüş, $Zn^{2+}$ iyonunun yoğunluğu belirgin bir biçimde artırdığı, $F^-$ iyonunun yoğunluğu azalttığı, $Cl^-$ iyonunun ise hafif şekilde artırdığı gözlemlenmiştir. Örneklerin XRD analizleri yapılmış, bu analizlerin sonucunda $Zn^{2+}$ ve $F^-$ iyonlarının beraber eklendiği örneklerde kafes hacimlerinde $F^-$ iyonunun artışı ile düşüş gözlemlenmiştir. Diğer örnekler kafes hacimlerinde değişimler göstermiştir. Örneklerde HA fazı ve çok az miktarda CaO fazı dışında bir faza rastlanmamıştır. FTIR analizleri, $Zn^{2+}$, $F^-$ ve $Cl^-$ iyonlarının HA yapısı içine katılıp katılmadığını anlamak için ilgili moleküldeki bağların bantları gözlemlenerek yapılmıştır. Ayrıca eklenen iyonların miktarları da FTIR analizi ile incelenmiştir. Sonuçlara göre iyonların HA yapısına başarılı şekilde eklendiği gözlemlenmiştir. SEM görüntüleri yorumlanmış, tanecik boyutları Rietvelt analizi

kullanılarak hesaplanmıştır. Tanecik boyutlarının $Cl^-$ iyonu eklenmesi ile artış gösterdiği, $Zn^{2+}$ ve $F^-$ iyonunun beraber eklenmesi ile düşüş gösterdiği görülmüştür. Mekanik özelliklerin belirlenmesi için Vickers mikrosertlik testi uygulanmıştır. Kırılma tokluğu, Vickers mikrosertlik test sonuçları kullanılarak hesaplanmıştır. Bu sonuçlara göre, $F^-$ ve $Zn^{2+}$ eklenmiş örnekler en yüksek mikrosertlik değerlerini vermiştir. Ayrıca $Zn^{2+}$ iyonunun kırılma tokluğunu düşürdüğü, $Zn^{2+}$ ve $F^-$ iyonlarının beraber eklendiği örneklerde ise saf HA ile karşılaştırıldığında kırılma tokluğunu artırtığı gözlemlenmiştir. $Cl^-$ ilavesi de kırılma tokluğu değerlerini düşürmüştür. $Zn^{2+}$ ve $F^-$ iyonlarının beraber eklendiği örnekler, yapısal ve mekanik özellikleri açısından en iyi örnekler seçilmiş, biyolojik özelliklerin belirlenmesi için yapılan deneyler bu örneklere uygulanmıştır. Biyolojik çalışmalarda Saos-2 hücre hattı kullanılmıştır. Hücre canlılığı tesbiti için Alamar Blue™ deneyi yapılmış, hücre farklılaşması tesbiti için alkalin fosfataz aktivitesi ölçülmüştür. Molce % 2 $Zn^{2+}$ eklenmesinin hücre yaşama kabiliyetini ve alkalin fosfataz aktivitesini artırdığı gözlemlenmiştir. Molce % 1 $F^-$ eklenmesi de hücre yaşama kabiliyetini ve alkalin fosfataz aktivitesini artırmıştır. Hücre morfolojisi için SEM görüntüleri incelenmiştir. Alamar Blue™ deneyi ve alkalin fosfataz aktivitesi ölçümünün desteklediği gibi, 2 Zn ve 2 Zn 1 F örneklerinde hücreler dendritik şekiller oluşturmuşlardır. Dendritik şekiller hücre-malzeme ilişkisinin uyumlu olduğunun göstergesidir. Çözünme testi için örnekler SBF içerisine batırılmış, pH değişimleri ölçülmüştür. Örnekler üzerindeki $Ca^{2+}$ iyonu tortularını gözlemlemek için SEM görüntüleri kullanılmıştır. pH değişimlerinde zamana bağlı artış gözlemlenmiştir. $F^-$ içeren örnekler, özellikle 2 Zn 1 F en düşük pH değişim sonucunu vermiştir. SEM görüntülerinde çözülme çukurları ve bazı apatitik oluşumlar gözlemlenmiştir.

**Anahtar Sözcükler:** Nano Hidroksiapatit, Çinko, Flor, Klor, Yapısal Özellikler, Mikrosertlik, Biyouyumluluk.

## ACKNOWLEDGEMENTS

I would like to show my gratitude to my advisor Assoc. Prof. Dr. Zafer Evis due to his patience, guidance and support throughout this study. This thesis would not be completed unless he was so tolerant. I owe my deepest gratitude to my co-advisor Prof. Dr. Feride Severcan for her concern, guidance and support throughout this thesis and especially in FTIR studies. Her precious ideas and suggestions made this study more valuable.

I would also like to thank to Assoc. Prof. Dr. Ayşen Tezcaner for her support and guidance in biological part of this thesis. She enlightened me with her precious experience and knowledge in *in vitro* studies. I would like to express my gratitude to Prof. Dr. Feride Severcan, Assoc. Prof. Dr. Zafer Evis, Assoc. Prof. Dr. Ayşen Tezcaner and Assist. Prof. Dr. Dilek Keskin for allowing me to work in their laboratories and for providing me an opportunity to expose this thesis.

I am indepted to Şebnem Garip for her precious friendship and also knowlegde and support in FTIR studies. It is a pleasure to thank to Mine Toker for her guidance and precious friendship throughout this study. I would like to thank my lab friends Özlem Aydın, Özge Erdemli, Ayşegül Kavas, Ömer Aktürk, Mert Baki, Yiğit Öcal, Aydın Tahmasebifar, Aslı Deniz and Serap Güngör for providing an entertaining environment in the lab. With their support and friendship, working in the lab became a game.

I would also like to thank Gülen Göktürk for her valuable friendship in Ankara. She made me love Ankara. It is a pleasure to thank to my old friends Mediha Işıtman and Kübra Bulut for their valuable support and friendship.

I would like to thank my aunts Sevgi Uysal and Sevil Şahin for their love and support in my education away from home. I would like to give my greatest thanks to my mother Sevinç Uysal, to my father Savaş Korkut Uysal and to my

brother Arda Uysal for their endless love and support they granted to my entire life. I feel lucky to be the piece of this family.

## TABLE OF CONTENTS

## LIST OF TABLES

TABLES

## LIST OF FIGURES

**FIGURES**

# CHAPTER 1

# INTRODUCTION

## 1.1. Apatites

Apatites are phosphatic minerals that are widely used in chemical industry as a raw material for various phosphorus containing products which can be listed as fertilizers, phosphoric acid, detergents, dentrifrices, pharmaceuticals, rust removers, additives for motor fuels, plasticizers, insecticides and other poisons and friction matches [1]. The raw material is the phosphate rock or phosphorite which is basicly composed of carbonated fluorapatite.

In 1929, Hausen separated apatites into eight different types, which were fluorapatite, alkali containing apatite, chloroapatite, carbonate apatite, sulfate apatite, hydroxylapatite, manganapatite and apatite containing rare earths. However, the list becomes longer (Table 1.1).

**Table 1.1.** Summary of the apatites.

| Mineral Name | Formula | Space Group | Reference |
|---|---|---|---|
| Fluorapatite | $Ca_{10}(PO_4)_6F_2$ | $P6_3/m$ | Hughes et al. (1989) [2] |
| Hydroxylapatite | $Ca_{10}(PO_4)_6(OH)_2$ | $P2_1/b$ | Ikoma et al. (1999) [3] |
| Chlorapatite | $Ca_{10}(PO_4)_6Cl_2$ | $P2_1/b$ | Mackie et al. (1972) [4] |
| Alforsite | $Ba_{10}(PO_4)_6Cl_2$ | $P6_3/m$ | Newberry et al. (1981) [5] |
| Pyromorphite | $Pb_{10}(PO_4)_6Cl_2$ | $P6_3/m$ | Dai & Hughes (1989) [6] |
| Strontium-apatite | $Sr_{10}(PO_4)_6(OH)_2$ | $P6_3$ | Pushcharovskii et al. (1987) [7] |

**Table 1.1.** (continued)

| | | | |
|---|---|---|---|
| Belovite-(Ce) | $Sr_6(Na_2Ce_2)PO_4)_6(OH)_2$ | P | Rakovan & Hughes (2000) [8] |
| Johnbaumite | $Ca_{10}(AsO_4)_6(OH)_2$ | $P6_3/m$ | Dunn et al. (1980) [9] |
| Clinomimetite | $Pb_{10}(AsO_4)_6Cl_2$ | $P2_1/b$ | Dai et al. (1991) [10] |
| Hedyphane | $Pb_6Ca_4(AsO_4)_6Cl_2$ | $P6_3/m$ | Rouse et al. (1984) [11] |
| Mimetite | $Pb_{10}(AsO_4)_3Cl_2$ | $P6_3/m$ | Dai et al. (1991) [10] |
| Morelandite | $Ba_{10}(AsO_4)_3Cl_2$ | $P6_3/m$ or $P6_3$ | Dunn & Rouse (1978) [12] |
| Turneaureite | $Ca_{10}(AsO_4)_3Cl_2$ | $P6_3/m$ | Dunn et al. (1985b) [13] |
| Britholite-(Ce) | $Ce_6Ca_4(SiO_4)_6(OH)_2$ | $P6_3$ | Oberti et al. (2001) [14] |
| Britholite-(Y) | $Y_6Ca_4(SiO_4)_6(OH)_2$ | $P2_1$ | Zhang et al. (1992) [15] |
| Chlorellestadite | $Ca_{10}(SiO_4)_3(SO_3)_3Cl_2$ | $P6_3$ or $P6_3/m$ | Rouse & Dunn (1982) [16] |
| Hydroxylellestadite | $Ca_{10}(SiO_4)_3(SO_3)_3(OH)_2$ | $P2_1/m$ | Hughes & Drexler (1991) [6] |
| Mattheddleite | $Pb_{10}(SiO_4)_3(SO_4)_3Cl_2$ | $P6_3/m$ | Steele et al. (2000) [17] |
| Vanadinite | $Pb_{10}(VO_4)_6Cl_2$ | $P6_3/m$ | Dai & Hughes (1989) [6] |
| Melanocerite-(Ce) | $Ce_5(Si,B)_3O_{12}(OH,F)\cdot nH_2O$ | | Anovitz & Hemingway (1996) [18] |

### 1.1.1. Structure of Apatites

Apatites are the compounds that have the general formula of $X_{10}(YO_4)_6Z_2$, where the X, Y, Z represent some ions. The most common examples of Z can be listed as $F^-$, $OH^-$ and $Cl^-$ which are gained the name of fluorapatite, hydroxylapatite

and chloroapatite to the compound, respectively if X represents $Ca^{2+}$. Due to being sensitive to ionic substitutions, $Ca^{2+}$ ions in the apatite structure can also be partly or completely replaced by some positive charged ions such as $Ba^{2+}$, $Sr^{2+}$ or $Pb^{2+}$. Besides being tolerant to single substitutions, coupled substitutions can also be observed in apatite structure. Some minerals which include pyromorphite ($Pb_5(PO_4)_3Cl$), vanadinite ($Pb_5(VO_4)_3Cl$) and mimetite ($Pb_5(AsO_4)_3Cl$) can be given as examples of coupled substituted apatites. The substitutions occur between the charges with the same sign. However, some substitutions with different charges are observed in apatite structures. In this case, dissimilar charges and vacancies neutralize the apatite molecule. The vacant sites result in non-stoichiometry in the molecule. Generally, the biological apatites and synthetic apatites are included in non-stoichiometric apatites. Non-stoichiometry results in complicated crystal chemistry. After giving these facts, apatite structure gains more general formula which enables different types of substitutions [19]. This formula can be represented as $X_{10}(YO_4)_6Z_2$ with possible parameters X, Y and Z that are listed in Table 1.2.

**Table 1.2.** X, Y, Z in apatite structure [20].

| X | Y | Z |
|---|---|---|
| $K^+$, $Na^+$, $Mn^{2+}$, $Ni^{2+}$, $Cu^{2+}$, $Co^{2+}$, $Sr^{2+}$, $Ba^{2+}$, $Pb^{2+}$, $Cd^{2+}$, $Y^{3+}$, $La^{3+}$, $Fe^{2+}$, $Zn^{2+}$, $Mg^{2+}$, $Ca^{2+}$, $Ce^{3+}$, $Al^{3+}$ | As, P, Si, V, Cr | F, Cl, O, OH, Br |

The basic apatite structure has hexagonal dipyramidal shape as a crystal system with space group $P6_3/m$. Hexagonal dipyramidal shape can be seen in Figure 1.1. $P6_3/m$ denotes that the structure has a primitive lattice with 6 fold symmetry axis, $6_3$ screw axis and is perpendicular to oblique glide plane. Approximate lattice parameters can be given as a=9.4 Å and c=6.9 Å with two formula units per unit cell [19].


a) b)

**Figure 1.1.** a) Hexagonal Dipyramidal shape [21]; b) Axial configuration of hexagonal shape [22].

In the apatite molecule, there are four different crystallographic positions. These are six tetrahedral sites for $P^{5+}$ ions, four Ca sites for $Ca^{2+}$ ions, six other Ca sites that form a hexagonal shape with an ion channel at the center and the channel site which is occupied by two monovalent ions such as $F^-$, $Cl^-$, $OH^-$ [23].

Fluoride ion forms the most symmetric apatite structure. It fits the ion channel well and due to its small radii, most symmetric position for an apatite structure is obtained [23].

### 1.1.2. Physical Properties of Apatites

Density, color, hardness, luminescence and diaphaneity can be listed as some important physical properties for apatites. The apatite density has the range between 3.16 and 3.22 $g/cm^3$ [22]. According to Mohs hardness scale, apatite is approximately 5. Apatites are non-fluorescent materials that have different colors such as white, yellow, green, red and blue. Their diaphaneity is ranged from transparent to translucent.

Any ion substitution results in structural changes in apatites. These structural changes have critical effects on some physical and mechanical properties such as solubility, hardness, brittleness, strain, thermal stability and optical properties like birefringence [24,25].

## 1.2. Calcium Phosphates

Calcium phosphates are the family of minerals which are composed of $Ca^{2+}$ ions with orthophosphates ($PO_4^{3-}$), metaphosphates ($PO_3^-$), pyrophosphates ($P_2O_7^{4-}$). In some compositions, hydrogen and hydroxyl ions can be accompanied into the structure.

Morphology, crystallite size, composition and structure are very important parameters for the calcium phosphate bioactivity, stability and mechanical properties [26].

Calcium phosphates have very low solubility in water. They become insoluble at higher temperatures. Therefore, as temperature increases, precipitation occurs. However, all of them dissolve in acids [19]. Solubility in water and degradation rate are important properties for the biomedical materials due to their effect on the cells. At pH 7.0, the degradation rates of some important calcium phophates can be ordered as α-TCP > monetite > brushite > β-TCP > HA. According to this list, the highly biocompatible compounds, HA and β-TCP has the lowest degradation rate and their solubility at pH 7.4 is very low [27].

Calcium phosphates are used in food industry in baking as a raising agent. Moreover, they gain an importance in biomedical field in bone and dental applications. Calcium phosphates are also used in wastewater treatment to eliminate phoshorus in the water. By using calcium salts, phosphorus is subjected to precipitation in the form of hydroxylapatite, tricalcium phosphate, brushite, monetite, otacalcium phosphate and amorphous calcium phosphate [28].

According to the number of the calcium ions in the molecule, calcium phosphates gain different names. The most important calcium phophate molecules are listed below with their characteristics.

### 1.2.1. Monocalcium Phosphates

Monocalcium phosphate is the compound with one calcium ion and Ca/P ratio of 0.5 [29]. It can be found in two forms. These are monohydrate ($Ca(H_2PO_4)_2 \cdot H_2O$) which is the compound with one water molecule and the

anhydrous salt ($Ca(H_2PO_4)_2$) in the acid with a pH range of 0.0-2.0. The monohydrate form has a triclinic space group, P1 with primitive unit cell parameters a=5.6261, b=11.889 and c=6.4731 Å with α=98.633°, β=118.262° and γ=83.344° [30]. Two formula units are found for each unit cell. Monocalcium phosphate monohydrate is also starting material of hydrothermal synthesis of monetite and hydroxylapatite which can be included in the list of important calcium phosphates. Monocalcium phosphate monohydrate suspension formed hydroxylapatite needle shaped crystals and monetite whiskers by hydrothermal treatment with the conditions 160°C and 1 MPa and 200°C and 2 MPa, respectively [31]. The density of monocalcium phosphate monohydrate was reported as 2.231 $g/cm^3$ [30]. Monocalcium phosphate monohydrate is used in phosphorus containing fertilizer production industry. Moreover, it is used in dry baking powders, food, tooth pastes and some beverages as nutrient, acidulant and mineral supplement [29]. In medicine, it can be used as a component of self-hardening calcium orthophosphate cements. It is very soluble and acidic. Therefore, monocalcium phosphate monohydrate is not found in biological calcifications.

Anhydrous salt form can be obtained when monocalcium phosphate monohydrate is heated to 100°C and one water molecule is released. It has the same space group and have two formula units per unit cell with lattice parameters a=7.5577, b=8.2531 and c=5.5504 Å with α=109.87°, β=93.68° and γ=109.15° [32]. It has the density 2.58 $g/cm^3$ [29]. Monocalcium phosphate anhydrous also is not found in biological calcifications due to its acidity and solubility. Moreover, it does not have any applications in medicine.

Unlike the other calcium phosphates, monocalcium phosphate solubility increases as temperature increases. Therefore, to obtain phosphorus for the agricultural fertilizers from the phosphate rock, sulfuric acid treatment is applied to produce more soluble monocalcium phosphate [33].

### 1.2.2. Dicalcium Phosphates

Another compound from the calcium phosphate family is the dicalcium phosphate which has two positive ion sites that are occupied by one calcium ion and one hydrogen ion. Dicalcium phosphates have Ca/P ratio of 1.0 [29]. These compounds are very important in terms of bone mineralization. Therefore, they are used in bone and teeth as dental cement and restorative material. Besides these practical uses, they are protonic conductors for fuel cell applications [34,35]. Dicalcium phosphates have also two forms. These are dicalcium phosphate dihydrate, brushite ($CaHPO_4 \cdot 2H_2O$) and dicalcium phosphate anhydrous, monetite ($CaHPO_4$).

#### 1.2.2.1. Brushite

Brushite has a monoclinic space group, Ia with body centered unit cell parameters a=5.812, b=15.180 and c=6.239 Å [36]. Its crystal structure is monoclinic prismatic. Monoclinic prismatic shape can be seen in Figure 1.2. Brushite is the intermediate in apatitic mineralization such as precipitation of hydroxylapatite and dissolution processes like dissolution of enamel in acids. The reported density for brushite was 2.318 $g/cm^3$ [37]. The solubility of brushite can be explained with a parabolic function of pH which has the minimum value near 5. Therefore, the solubility range pH of brushite was accepted as 2.0-6.0 [29]. When brushite was heated to 80 °C, the other form, monetite was formed. Monetite had three different phases. Between 320 and 340°C, $\gamma$-$Ca_2P_2O_7$, between 340 and 700°C $\beta$- $Ca_2P_2O_7$ phases were formed. By further heating to 1200°C, $\alpha$- $Ca_2P_2O_7$ phase was observed. The formation of monetite from brushite was a dehydration process which used water as a catalyst at 135°C [38]. However, hydrothermal conversion of brushite to monetite resulted in porosity increase and strength decrease [39].

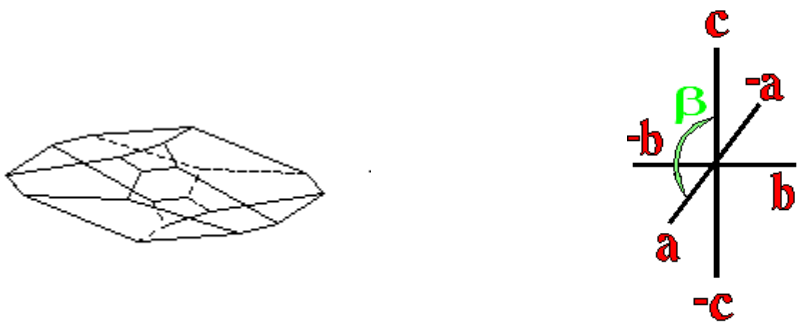


a) b)

**Figure 1.2.** a) Monoclinic prismatic shape; b) Axial configuration of monoclinic shape [22].

Another way to produce brushite was the reaction of TCP powder with an acidic phosphate source such as phosphoric acid and monocalcium phosphate monohydrate. By this method, a mechanically stable implant was formed in situ which degraded over a time period of 6-12 months [40,41]. Brushite showed good biocompatible properties in vivo.

Brushite was found in pathological calcifications such as dental calculi, crystalluria, chondrocalcinosis and urinary stones [29]. It is also used as flame retardant and slow release fertilizer. In food industry, it is used as mineral supplement, texturizer, bakery improver and water retention additive [29].

In medicine, the brushite is used in calcium phosphate cements. The main disadvantage of the brushite based cements is the short setting time which results in low mechanical strength [42]. To increase the setting time, low powder to liquid ratio which results in high porosity and lower mechanical strength and high setting retardant concentration in the cement paste should be adjusted [42-44]. Increasing the concentration of the setting retardant increased the setting time and mechanical strength by smaller precipitated crystals [42-45]. It was also specified that very high retardant concentrations resulted in decrease in mechanical strength (up to 1 molar) [43]. Moreover, brushite is used widely for maxillofacial bone augmentation in the forms of cement and granules [46-48].

Brushite and monetite can be used as solid electrolytes in battery devices. By studying the dehydration process, the role of each water molecule or proton species can be understood. In dehydration of brushite first a chemical surface reaction occurs and an intermediate layer with water molecules is formed. Then, by thermolysis, water molecules are separated from the brushite structure and turns the structure into monetite [32].

### 1.2.2.2. Monetite

Monetite has a triclinic space group, P1 with primitive unit cell parameters a=6.910, b=6.627 and c=6.998 Å with α=96.34°, β=103.82° and γ=88.33° [29,49]. Its crystal structure is triclinic pinacoidal that is respresented in Figure 1.3 [22]. Monetite is the most stable calcium phosphate at a low pH. Therefore, when there is healing or inflammatory site where pH is less than 7.4, monetite structure can be seen. However, when the pH becomes the physiological pH 7.4, monetite transforms into hydroxylapatite. Moreover, it is less soluble and more stable than brushite at temperatures higher than 121°C. However, due to monetite's slow crystal growth rate, brushite is formed easier than monetite. The calculated density of monetite was reported as 2.89 g/cm$^3$ [50]. Like in brushite, the solubility of the monetite depends on pH. Moreover, it was found that the solubility decreased with increasing the temperature.

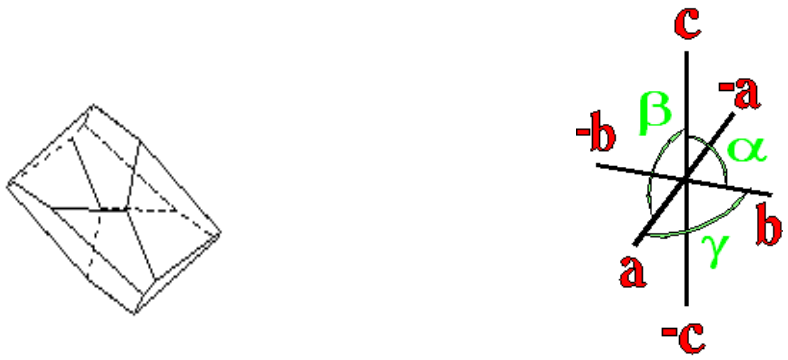


a) b)

**Figure 1.3.** a) Triclinic pinacoidal shape; b) Axial configuration of triclinic shape [22].

Monetite can be synthesized by several methods such as; hydrothermal method [51,52], precipitation from microemulsion [53], crystallization from solution [54], electro and chemical deposition [55-57] and microwave assisted method [24].

Monetite is used in toothpastes, chewing gums and used as acidic regulator, anti-caking agent, dough modifier and emulsifier in food industry, besides usage in biomedical industry [58].

Monetite is biocompatible and biodegradable. However, it is not formed during normal or pathological calcifications [29]. It was also investigated that local application of monetite granules in biocartial cranial defects on rabit calvaria resulted in first phases of bone regeneration. Due to the similarity of solubility products of monetite and serum, monetite could rapidly resorb and transform into bone [59-60]. Monetite is also found in dental and urinary stones [61,62]. It is the major constituent of the resorbable bone cements in addition to brushite. However, due to poor mechanical properties, their applications are limited to non-load bearing applications. Orientation of crystals is also an important factor that affects the mechanical properties [63]. Monetite was also studied as a starting material for hydroxylapatite which could be used as a coating material on metals or carbon fiber reinforced carbon composites. Monetite is converted into hydroxylapatite by hydrothermal treatment in an autoclave by using ammonia solution [64]. Therefore, the monetite is the precursor of the hydroxylapatite which has similar structure with the bone. To control the hydroxylapatite crystal orientation, monetite crystals were studied to be produced in nanosheets [65].

Monetite synthesis by dehydration and recrystallization of brushite is a widely used production method. The reaction is favourable in water and at high temperatures. In addition to these, sterilization process is cheaper for monetite due to its stability at high temperatures. Therefore, monetite becomes a candidate for bone regeneration materials.

There are two types of synthesis methods. One is based on the boiling the brushite powders in the $H_3PO_4$ solution [66-68] and the other is based on heating the brushite in a static air atmosphere at temperatures between 200°C and 250°C

[60-71]. However, these two methods were unable to control the particle size and shape distribution of the brushite particles. Therefore it became difficult to obtain submicron sized particles of monetite [72]. Large monetite crystals with rhombohedral diamond, plate-like, rectangular, needle-like [73], hexagonal prismatic [74] shape were obtained. To produce submicron monetite particles, many methods were proposed such as spray drying, autoclave based techniques and microwave-assisted heating method. By using these methods monetite crystals of spheres, monodispersed nanofibers, bundles of nanowires, nanosheets could be obtained [34, 74-78].

The crystal growth rate of monetite increases with temperature and time. It was studied that, by hydrothermal reaction, monetite crystals were obtained on the hydroxylapatite. The surface defects of hydroxylapatite served deposition sites for the monetite crystals [79].

Microwave assisted method is an useful technique to produce hydroxylapatite with flowerlike morphology by using monetite as the precursor. The transformation from monetite to hydroxylapatite is a dissolution and reprecipitation mechanism. The monetite continuously dissolves into $Ca^{2+}$ and $(PO_4)^{3-}$ ions in the presence of NaOH, because the high pH shifts the thermodynamic equilibrium in the side of ion formation. The hydroxylapatite reprecipitates and crystallizes on the surface of the monetite [24]. As the heating time increases, the nanosheets turn into flowerlike morphology [24].

Moreover, there is also a method which uses the precipitation of $CaCO_3$ powders in ethanol solution at room temperature (RT) by only stirring 3h and obtain submicrometer particles with nanosheet texture. Therefore, an economical and easy way of production of monetite was determined [80].

Low temperature processes result in more consistent materials which do not have varying powder crystallinity [81]. When monetite was mixed with hydroxylapatite, it was found that the mixture had higher solubility in water than pure monetite and hydroxylapatite have. This stemmed from the partial solubilization of the chemicals. As the solubiliziation and reprecipitation increased,

the $Ca^{2+}$ and $(HPO_4)^{2-}$ ion concentrations increased and formation of hydroxylapatite occurred [81].

Besides nanosheets, hydroxylapatite can be synthesized in needle-like shape or in nanorod by using different adjusting modes of the pH and the monetite as the precursor [82]. This production method is also a simple and cost effective one. According to the adjusting modes of the pH, single phase hydroxylapatite crystal or the mixture of a small amount of hydroxylapatite and mainly octacalcium phosphate phase can be obtained.

Tricalcium phosphate is another calcium phosphate compound which has greater importance in terms of biomedical applications due to its role in pathological calcifications. Therefore, tricalcium phosphates were discussed in the next topic in detail.

### 1.2.3. Tetracalcium Phosphates

Tetracalcium phosphate is the group of calcium phosphates that has four calcium atoms. The Ca/P ratio of tetracalcium phosphate is 2 [29]. It has the formula ($Ca_4(PO_4)_2O$). Tetracalcium phosphate has the monoclinic structure with a primitive unit cell $P2_1$ space group and with unit cell parameters of a=7.023, b=11.986 and c=9.473 Å with β=90.90° [29,83]. Tetracalcium phosphate has four formula units per unit cell. It has the density of 3.051 $g/cm^3$ [83]. Tetracalcium phosphates are more soluble than hydroxylapatite in the aqueous media. Therefore, it can not be produced by precipitation reaction. The only method used for tetracalcium phosphate production is solid-state reactions at temperatures above 1300°C. Due to its high solubility, it is not stable in aqueous conditions and transforms into hydroxylapatite and calcium oxide quickly. Therefore, tetracalcium phosphates are not found in physiological systems [84]. Tetracalcium phopshates are used in the production of self-setting bone cements by mixing with monetite or brushite. In bone cement, this mixture turns into hydroxylapatite when there is water in the medium. Another application of tetracalcium phosphates as bone cement is the composite of tetracalcium phosphate and collagen. This material can

be used as graft in bone and cartilage tissue. Another advantage of this material is the small replacement time of bone. This provides better fixation after surgery by preventing loosening and micromotion [85]. Moreover, tetracalcium phosphates were used to control the properties of metals by being a by product of the reaction between phosphorus, oxygen and lime in the iron manufacturing.

### 1.2.4. Octacalcium Phosphates

Octacalcium phosphate is another type of calcium phosphate which includes eight calcium atoms with the formula $Ca_8(HPO_4)_2(PO_4)_4 \cdot 5H_2O$. The Ca/P molar ratio of octacalcium phosphate is 1.33 and the water content is variable. Octacalcium phosphate has the triclinic structure with space group of P1, a primitive unit cell and with unit cell parameters a=19.692, b=9.523 and c=6.835 Å with $\alpha$=90.15°, $\beta$=92.54° and $\gamma$=108.65° [29,86]. Octacalcium phosphates have two asymmetric units per unit cells that means in one unit cell, there are two largest structural units which have atoms that are placed asymmetrically. Octacalcium phosphates are stable between pH values of 5.5 and 7.0 in aqueous solutions at 25 °C [29]. The main production methods can be listed as hydrolysis of brushite and precipitation reactions. The production parameters are temperature, the solvent used, pH and time. By adjusting these parameters, octacalcium phosphates with different compositions and morphologies are obtained. Octacalcium phosphate has the density of 2.61 g/cm$^3$ [87]. It is the intermediate of the precipitation reaction of hydroxylapatite and other biological apatites [88]. It has similar structure with hydroxylapatite in terms of apatitic layers [26,89]. This similarity results in ease of transformation to hydroxylapatite. Due to its high solubility, it can nucleate and grow more easily than hydroxylapatite. Octacalcium phosphates can be observed in dental and urinary calculi and other pathological calcifications [90]. It was suggested that octacalcium phosphate was a precursor of biological apatite found in natural and prosthetic heart valves [29].

### 1.2.5. Amorphous Calcium Phosphates

Amorphous calcium phosphate is generally known as the calcium phosphate which has the atomic Ca/P ratio is between 1.2 and 2.2 [29]. It can be predicted that amorphous calcium phosphates have an apatitic structure with very small crystal sizes that result in amorphous appearance [19]. Amorphous calcium phosphates are not found in bone structure. However, some sodium, magnesium, carbonate and pyrophosphate included forms are found in various soft-tissue pathological calcifications [29,91]. According to electron microscopy results, amorphous calcium phosphate particles had spherical shapes. The diameters of these spheres were in the range of 200 to 1200 Å [92]. Amorphous calcium phosphates are stable at pH between about 5.5 and 12 in aqueous solutions at 25 °C [29].

Amorphous calcium phosphates was thought to be formed at the begining of the precipitation. It was the first phase precipitates in the mixing of supersaturated solution consisting of calcium and orthophosphate ions [29]. It had lower surface energy than octacalcium phosphate and hydroxylapatite have [29]. In wet atmospheric conditions, the amorphous octacalcium phosphate transforms into monetite and hydroxylapatite. The temperature has a decreasing effect on the time of transformation [93]. The hydroxylapatite produced from the octacalcium phosphates is generally non-stoichiometric type. When particle size was investigated, it could be said that supersaturation, pH and temperature had direct effects on particle size of amorphous calcium phosphates. The particle size became smaller, if there was high supersaturation. For the identical pH, the particle size increased with increasing the temperature [94]. Moreover, presence of pyrophosphate, carbonate and/or magnesium ions in the solution prevents formation of more crystalline phases and enhanced amorphous calcium phosphate formation [29]. However, fluoride ion has an adverse effect [29].

Amorphous calcium phosphates are used in medicine as a constituent of calcium phosphate cements and as a filling material in dentistry. By using polymers and amorphous calcium phosphates, bioactive composites for dentistry can be obtained [29]. Moreover, some microorganisms can consume amorphous calcium

phosphate due to its solubility and physiological pH of its aqueous solution [29]. Therefore, it can be used in culture medium.

In other fields, such as food industry, amorphous calcium phosphates can be used as a syrup clearing agent and also as an inert filler in pelleted drugs [29].

### 1.3. Tricalcium Phosphates

TCP is a compound in the calcium phosphate family and includes three calcium atoms. TCP has Ca/P ratio of 1.5. TCP has higher solubility than hydroxylapatite. Therefore, it is generally used as a resorbable bioceramic. Due to this property, TCP and hydroxylapatite composites are studied to make hydroxylapatite more degredable. Moreover, they are used as a starting material in bone cement that is made of calcium phosphates due to no heat release during the reaction [95].

There are three polymorphs of the TCP. These are β-TCP, α-TCP and α'-TCP. These polymorphs' stability regions can be listed as below 1180°C, between 1180°C and 1400°C, 1470°C and above, respectively [26, 96, 97].

β-TCP is used in dry powdered food as a texturizer, bakery improver and anti-clumbing agent [29]. It can be used as a dietary and mineral supplement in food. Moreover, it is used as a polymer stabilizer and inert filler in pelleted drugs [29].

#### 1.3.1. Structure of TCP

The structure of TCP can be explained by separating into two parts. These are structure of α-TCP and structure of β-TCP.

##### 1.3.1.1. Structure of β-TCP

X-ray diffraction is used to determine the crystal parameters. There is another method that is used to detect exact crystal parameters which is called high-resolution neutron powder diffraction. According to this method, β-TCP has unit cell parameters a = b =10.4352 Å and c= 37.4029 Å with γ=108.65° [29,98]. Moreover, it was also found that, β-TCP had the crystal structure with a rhombohedral shape and R3c space group [98]. It has the density of 3.08 g/cm$^3$.

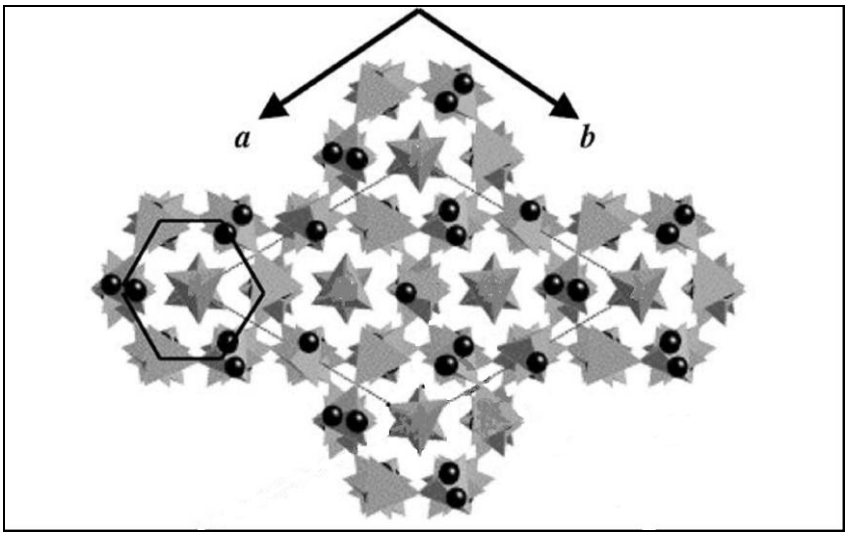


**Figure 1.4.** Projection of the crystal structure of β-TCP on the (001) plane [99].

According to the Figure 1.4, there are two columns which include different configured $CaO_n$ and $PO_4$ groups with n that denotes number of oxygen atoms which can take the values of 3, 6, 7 and 8 [99] . These are the column A and column B. Colum A is at the center of the hexagonal shape. The other column B is represented by the shape with two spheres which form a triangle by having the A column at the center. In Figure 1.5, the column A and the column B with their groups ordered in hexagonal structure in c direction are presented.

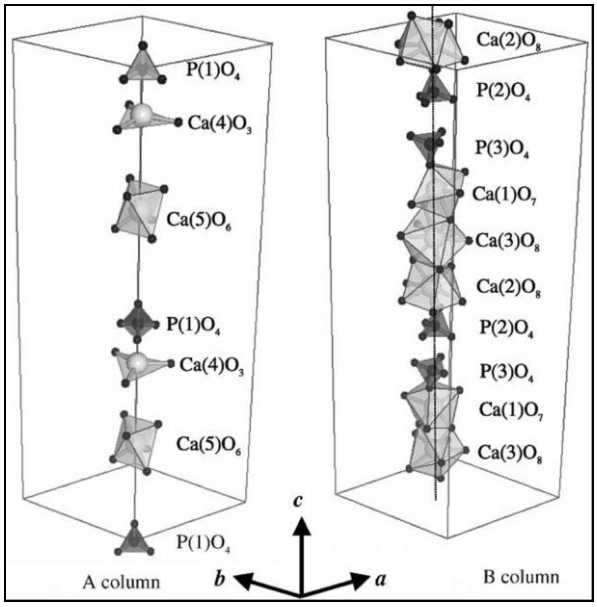


**Figure 1.5.** The configurations of $CaO_n$ and $PO_4$ groups with n=3, 6, 7 and 8 for column A and B in the direction of c [99].

The crystal growth mechanism of β-TCP can be explained by nucleation-aggregation-agglomeration-growth mechanism theory. According to this theory, after the reaction of calcium and phosphate precursors, β-TCP nano sized crystallites are formed by nucleation and growth. Then, due to some molecular attractions between the nanocrystals with different forces, aggregates are formed which minimize the surface free energy. As a last step, agglomerate is formed by further crystal growth providing aggregates gathered. Increase in temperature results in increase in particle size by addition of agglomerates. therefore, secondary particles are formed [99]. In Figure 1.6, this process is summarized.

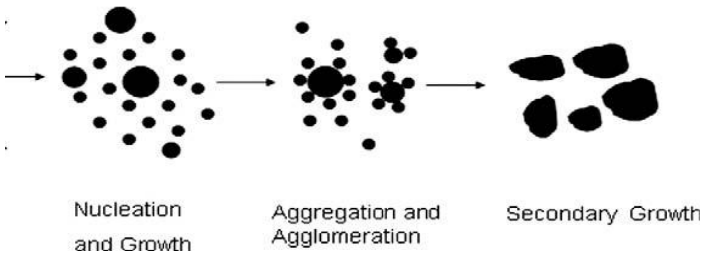


**Figure 1.6.** Nucleation-aggregation-agglomeration-growth mechanism of β-TCP [99].

β-TCP is the most preferable polymorph among the three phases due to its high chemical stability, bioresorption rate and mechanical strength. However, to be used as an implant, its mechanical strength should be improved by densification. Densification is achieved by effective sintering. Reaction routes also affect the phases formed during sintering. α-TCP can be obtained by production with a wet chemical method instead of solid state reactions between 600 and 800°C [100-102]. Doping some compounds also affects the sintering of β-TCP. MgO and $SiO_2$ doping effects on β-TCP sintering were investigated [100,101,103]. According to the findings, MgO increased the β to α phase tranformation temperature whereas $SiO_2$ decreased. Therefore, it can be said that $SiO_2$ inhibits the sintering of β-TCP. Calcium to phosphorus ratio is another parameter that affects the sintering [100,101,103].

When sintering behaviour of pure β-TCP was investigated, it was found that, the sintering rate incrased rapidly between 850°C and 1200°C [102].

Grinding time is also another property which affects the crystal structure of β-TCP. β-TCP transforms into calcium deficient HA by hydrolysis. This reaction can be accelerated by increasing the grinding time [104]. As grinding time increases the amorphous phases in the structure also increases. The grinding results in smaller particle size up to a critical level. After this level is reached, the given energy is used not to reduce the particle size, but to form some defects in the crystal lattice. Nanocrystals are formed within a single particle which leads to the loss of crystallinity. The reactive fraction in the material is the amorphous one. The crystalline fraction remains unreacted during setting process. Therefore, it can be concluded that as the amorphous fraction increases, the solubility of the material increases. Amorphous fraction depends on the grinding time. Then, the increase in the grinding time results in increase in solubility [104].

Moreover, the range of pore sizes is narrowed as the grinding time increases. The porosity increases with increase in the grinding time [104]. In contrast to porosity, compressive strength decreases as the grinding time increases.

### 1.3.1.2. Structure of α-TCP

α-TCP crystals have the monoclinic space group $P2_1/a$ with primivite unit cell lattice parameters of a=12.887, b=27.280 and c=15.219 Å with β=126.20° and [29,105]. This type of crystals have 24 formula per unit cell. It has the density of 2.86 $g/cm^3$ [29].

Generally, α-TCP is used in bone cement due to it is setting to a less soluble phase when it is subjected to water. The reaction occurs at low temperatures which enables using this material in body. The setting reaction which consists of hydrolysis and precipitation includes some steps. First, the α-TCP transforms into dicalcium phosphate dihydrate. Then octacalcium phosphate phase is observed. As a last step calcium deficient hydroxylapatite is formed. The rate of setting reaction is affected by physical properties of phosphate, powder to liquid ratio and some impurities such as inorganic salts, organic and polymeric additives [106-108]. Monovalent ions increase the rate of setting reaction, whereas diavalent ions retard the reaction due to competition with $Ca^{2+}$ ions [109]. As temperature increases, the setting reaction accelerates. Moreover as pH increases, the rate of the hydrolysis reaction decreases. α-TCP enables some modifications in its structure. For example, there was a study which reported the effect of gelatin and $Sr^{2+}$. Gelatin improved the mechanical properties of α-TCP by decreasing the inhibiting effect of $Sr^{2+}$ on crystallization [110].

The hydration kinetics were also observed for α-TCP. It was investigated that, the degree of the reaction was related with the particle size [111]. Moreover, the hydration kinetics of α-TCP can be separated into two rate limiting steps [111]. The first step is controlled by solid-liquid interface. In this step precipitated crystals are begun to form and results in a thin layer around α-TCP particles which enables diffusion rapidly. The second step is controlled by diffusion through the hydrated layer. As the time passes, the hydrated layer becomes thicker which make the diffusion a rate limiting step.

It was also investigated that some porous structures of α-TCP could be obtained by coating of polyurethane and sintering the sample at several temperatures.

According to the results, as sintering temperature increased, porosity decreased. At the temperatures 1400 and 1450°C, microporous structures could be seen [112]. However, when the temperature was increased to 1500 and 1550°C, microporosity could not be seen. Moreover, porosity decreased from 95 % to 90 % [112]. Linear shrinkage increased as sintering temperature increased [112].

### 1.3.2. Doping of Ions into TCP

In a study, $Sr^{2+}$ and gelatin doped α-TCP was investigated as a development in bone cements. $Sr^{2+}$ was known to have a positive effect on osteoblasts. It increases the number of osteoblasts and improves bone formation. Moreover, $Sr^{2+}$ ion decreases osteoclast number and activity and inhibits bone resorption. However, as the $Sr^{2+}$ amount increases, the reactivity of α-TCP decreases due to the substitution of $Sr^{2+}$ ions into $Ca^{2+}$ sites [110]. Therefore, it can be said that $Sr^{2+}$ retards and also inhibits the hydrolysis reactions of α-TCP. $Sr^{2+}$ ion is bigger than $Ca^{2+}$ ion. Therefore, it deforms the structure of α-TCP. As a result, the crystallinity decreases and the solubility increases. $Sr^{2+}$ also results in morphology changes [110].

Moreover, there are studies which investigated the biological effects of iron-doped α-TCP for spinal applications. It was observed that iron doped α-TCP showed good resorption than pure α-TCP in 6 months [113]. It also increased the resorption rate of the α-TCP cement and new bone formation. The resorption rate increased is due to the increase in activity of macrophages [113].

### 1.3.3. Mechanical Properties of TCP

#### 1.3.3.1. Mechanical Properties of β-TCP

β-TCP has the most preferred chemical stability, mechanical strength and bioresorption rate among the other TCP phases when it is used in biomedical applications. To increase the mechanical strength of β-TCP, the densification process should be taken into account. Sintering temperature is strongly related to the densification process. The shrinkage rate of β-TCP is close to zero up to 800ºC [110]. However, between 850 and 1200ºC, it increases sharply [110]. Above

1200ºC the shrinkage rate becomes close to zero again [110]. At this point the transformation from β-TCP to α-TCP occurs. This transformation prevents further densification. Moreover, α-TCP transformation results in the expansion of the sample volume which decreases the density of the compound. Microcrack formation is also observed due to expansion of the sample volume in α-TCP. These microcracks decrease the strength of the material. Therefore, it can be said that, α-TCP is not a good candidate for surgical implants. There were also studies which investigated the effect of pyrophosphate ($Ca_2P_2O_7$) on β-TCP sintering temperature. It was found that addition of small portions of pyrophosphate (3% wt.) increased the phase transformation temperature of β-TCP to α-TCP by 50ºC. At 1200ºC, the doped β-TCP had higher density than pure β-TCP [109]. Up to 1300ºC, only β-TCP phase was present in pyrophosphate doped TCP. Above 1300ºC, the microcrack formation was seen. This resulted in a decrease in the density of doped β-TCP [110].

Some parts of the body such as periodontal bone defects repair or sinus lift requires implants that have resorbable property. The resorbable material should be easily replaced with the bone minerals. β-TCP is a good candidate for this type of applications. Moreover, β-TCP can be used as bone fillers in socket preservation and sinus augmentation applications [114]. However, it should posses adequate mechanical strength. To achieve the desirable mechanical strength, densification of β-TCP gains importance. Besides densification, crystallinity, purity and appropriate stoichiometry affect osteointegration and bioactivity [115].

#### 1.3.3.2. Mechanical Properties of α-TCP

Mechanical properties of α-TCP are highly depended on its porosity, sintering temperature, particle size and precursor type used to synthesize it. Therefore, it is difficult to give exact values for Young's modulus shear modulus, bulk modulus and Poisson's ratio which can be calculated from the elastic constants of the samples.

For shear modulus, α-TCP gave a value of 35.94 GPa in a study whereas in another study 91.3 GPa was obtained [116,117]. Young's modulus of TCP had also different values in different studies. Two examples can be given for these values such as 103.97 GPa and 188.6 GPa [115,116]. Poisson's ratio was defined as 0.45 [117]. However, some computer programs were used to predict the elastic constants and some mechanical properties. The calculated parameters could be listed as Young's modulus (102.4 GPa), shear modulus (40.1 GPa), bulk modulus (75.9 GPa) and Poisson's ratio (0.275) [118]. When these results were compared with β-TCP results, it could be said that, β-TCP was a stronger material than α-TCP. It was also supported by the fact that β-TCP had more stronger bonded phosphate groups than α-TCP have [118].

### 1.3.4. Biological Properties of TCP

Osteogenic differentiation and osteoconduction can be achieved by TCP scaffolds. It was also investigated that TCP had osteoinductive properties in vivo. Sintering temperature has also effect on biological properties. The synthesis of some proteins by macrophages such as tumor necrosis factor α, interleukin, prostaglandin E2 are higher when sintering temperature is low [119]. However, synthesis of some proteins such as cytokine or PG can not be stimulated by TCP when sintering temperatures are 900 or 1200 °C [119].

#### 1.3.4.1. Biological Properties of β-TCP

β-TCP never occurs in biological calcifications [29]. However, magnesium substituted form called whitlockite is found in dental calculi and urinary stones, dentinal caries, salivary stones, arthritic cartilage and some soft tissue deposits [29].

β-TCP is widely used for bone substitution due to its quality of fusion in terms of resorption capacity, limited loss of correction and bioactivity. When this material was compared with allograft substitutes for idiopathic scoliosis, it was found that, β-TCP had higher resorption rate. It was investigated that TCPs were resorbed totally in 2 years whereas allograft particals could be seen in the x-ray

detection for the same period. In terms of loss of correction, it was found that there was no more loss of correction after 6 months for β-TCP, whereas for allografts the loss of correction lasted for 2 years [120]. When β-TCP was resorbed in vivo, the pores were replaced by connective tissue and then bone tissue. The resorption percentage was found as 40, whereas the replacement of the biological tissue had the percentage of 80 [120]. The replacement and resorption were seen both inside the pores and at the outer surface of the material. The results were consistent with the theoretical mineral content of woven bone in early stages of endochondral ossification. The dissolved ions from the β-TCP were detected with radioactive labelling. It was found that these ions were reused by osteoblast cells to form the extracellular bone matrix. β-TCP is generally used in non-load bearing applications. However, if the porosity and mechanical strength are adjusted, it can also be used in load-bearing applications [120].

The composite of β-TCP and poly-L-lactic acid was produced to enhance the properties of β-TCP. It improved modulus of elasticity and tensile strength [120]. The biological activity of this material was also observed in vivo and in vitro. According to in vitro experiments, as the β-TCP weight percentage increased, the osteogenous cell proliferation and extracellular bone matrix formation increased. In vivo experiments indicated that β-TCP containing materials had faster degradation kinetics and resulted in less inflammatory reactions when compared with pure poly-L-lactic acid. In terms of osteogenesis, pure β-TCP gave the same results with β-TCP/poly-L-lactic acid composite which included 60 % β-TCP by weight [120].

β-TCP is also used as a bone morphologic protein carrier to induce bone formation in the body. The studies combining β-TCP with some degredable polymer such as p-dioxanone and polyethylene glycol and recombinant bone morphogenic proteins were very common. This protein alters the bone inducing capacity of the β-TCP which is known to be a biodegradable and osteoconductive material [121]. The porosity of β-TCP is also important in terms of carrying capacity [122].

β-TCP is used as a constituent of calcium phosphate bone cements. HA and β-TCP biphasic components are widely used as a bone substitution bioceramics [122].

When compared with demineralized bone matrix and calcium deficient HA, β-TCP gave lower seeding efficacy values of bone marrow stromal cells [123]. However, in terms of protein content and alkaline phosphatase activity, it showed similar results with demineralized bone matrix and calcium deficient HA [123].

#### 1.3.4.2. Biological Properties of α-TCP

α-TCP can not be seen in biological calcifications [29]. However, it is widely used as a constituent of the bone cement material. Pure α-TCP has some drawbacks that prevents α-TCP to be a good candidate for biomedical field. The most important one is its quick resorption rate [29]. Therefore, there were many studies which used more than one calcium phosphates for the bone cement production to improve the cement properties. One of them was α-TCP/ DCPD/ TeCP system. In vivo studies showed that this system was very biocompatible. In 6 months the newly bone started to form and covered the implant surface [109]. In 1 year, new bone surface totally covered the implant [109]. Another important parameter investigated was resorption rate. The resorption took place in two steps. These were dissolution and digestion by phagocytotic cells. This system was resorbed faster than HA, because HA had more stable structure due to sintering process [109].

α-TCP can be also used as a drug carrier. In a study, simvastatin was loaded on α-TCP and its effect on bone formation was observed. It was investigated that, in simvastatin loaded group, cell migration and new bone surrounded the defective tissue. α-TCP particles were fully surrounded by regenerated bone. The newly formed bone was reached at the middle of the α-TCP particles. Some contact regions with α-TCP, new bone produced marrow spaces. In α-TCP without simvastatin, it was also seen newly bone formation. However, the group with simvastatin was more effective. When these two were compared with the control group, which had the defect site and was without any treatment, it could be seen that, osteoblasts form a flattened surface on the newly formed bone and in the

middle of the defect, there was connective tissue. In terms of cell numbers α-TCP groups gave slightly higher results when compared with the control group. However, the α-TCP with simvastatin drug had significantly higher results in terms of cell numbers and newly formed bone amount [124].

It was investigated that α-TCP had positive effects on cell proliferation and differentiation. The effect on differentiation on mesenchymal cells is unknown. However, it was hypothesized that it was related to the release of $Ca^{2+}$ and $PO_4^{3-}$ ions due to dissolution. α-TCP has high solubility among most of the bioceramics. Therefore, the release of $Ca^{2+}$ and $PO_4^{3-}$ ions is higher in α-TCP which is an inhibitor of alkaline phosphatase activity. α-TCP increases the cell proliferation which results in decrease in alkaline phosphatase synthesis [125,126]. Osteocalcin production was also investigated for α-TCP. Osteocalcin is produced by osteoblasts and osteocytes and responsible for matrix mineralization. Therefore increase in osteocalcin production is an indicator of cell differentiation. It was observed that α-TCP had an increasing effect on osteocalcin production [127].

The composite of HA and α-TCP which was named as the silicon stabilized α-TCP which was used as a starting material in production of bioresorbable porous ceramic scaffolds for artificial bone grafts [29].

### 1.4. Hydroxylapatite

Hydroxylapatite has the molecular formula $Ca_{10}(PO_4)_6(OH)_2$. In stoichiometric HA, the Ca/P ratio is 1.67. However, by doping some ions into HA structure, this ratio changes which results in non-stoichiometric HA.

HA can be produced by several methods. These methods can be listed as solution precipitation and coprecipitation, solid state reactions, sol-gel techinque, emulsion and microemulsion technique, hydrothermal reactions, hydrolysis and solution mediated reactions [128]. According to the production methods, HA with different mechanical, structural and biological properties can be obtained.

### 1.4.1. Structure of HA

There are two crystal structures of hydroxylapatite. These are hexagonal structure and monoclinic structure.

#### 1.4.1.1. Hexagonal Structure

Hexagonal HA crystal structure posses $P6_3/m$ space group symmetry, with the lattice parameters of a = b = 9.432 Å and c = 6.881 Å [129]. The structure is composed of six tetrahedral phosphate group that are surrounded with six Ca atoms. There is another site for four Ca atoms which is the center of an equilateral triangle on screw axis. There are two $OH^-$ molecules in the structure which is located in the columns on the screw axis. These $OH^-$ molecules point out reverse directions. The steric interferences between these adjacent $OH^-$ ions results in ability to substitutions of different ions such as $Cl^-$, $F^-$ by omitting $OH^-$ ion [129].

#### 1.4.1.2. Monoclinic Structure

Monoclinic HA crystal structure posseses $P2_1/b$ space group with unit cell parameters a = 9.421 Å, b = 2a = 18.842 and c = 6.881 Å [129]. The cystal structure of monocilinic HA is the same with hexagonal HA, except the directions of OH groups. In monoclinic structure, OH groups point out the same directions and they reverse in the other direction. This structure makes monoclinic HA the most thermodynamically stable and most ordered structure. Monoclinic HA has also more stoichiometric structure than hexagonal HA due to difficulty in substitution of ions caused by OH orientation.

### 1.4.2. Doping of Ions into HA

As it was mentioned before, hexagonal HA enabled some ion incorporations. The ions and their available site are represented in Table 1.2. Moreover some ions with their substitution sites and their effects on lattice parameters and crystallinity of HA are represented in Table 1.3.

**Table 1.3.** Qualitative effects of some substituents of HA on the lattice parameters and crystallinity of apatites [130, 131].

| Substituent | Ionic Radii (Å) | Lattice Parameters (Å) | | Crystallinity |
|---|---|---|---|---|
| | | a-axis | c-axis | |
| **$Ca^{2+}$ substitutions** | 0.99 | 9,438 | 6,882 | |
| Strontium ($Sr^{2+}$) | 1.12 | increase | increase | no change |
| Barium ($Ba^{2+}$) | 1.34 | increase | increase | decrease |
| Lead ($Pb^{2+}$) | 1.20 | increase | increase | decrease |
| Potassium ($K^{+}$) | 1.33 | no change | no change | no change |
| Sodium ($Na^{+}$) | 0.97 | no change | no change | no change |
| Lithium ($Li^{+}$) | 0.68 | no change | no change | no change |
| Magnesium ($Mg^{2+}$) | 0.66 | decrease | decrease | decrease |
| Cadmium ($Cd^{2+}$) | 0.97 | decrease | decrease | decrease |
| Manganese ($Mn^{2+}$) | 0.80 | decrease | decrease | decrease |
| Zinc ($Zn^{2+}$) | 0.74 | increase | increase | decrease |
| Aluminium ($Al^{3+}$) | 0.51 | increase | increase | decrease |
| **$OH^{-}$ substitutions** | | | | |
| Fluoride ($F^{-}$) | 1.31 | decrease | no change | increase |
| Chloride ($Cl^{-}$) | 1.81 | increase | decrease | no change |
| **$PO_4^{3-}$ substitutions** | | | | |
| Carbonate ($CO_3^{2-}$) | | decrease | increase | decrease |

### 1.4.2.1. Doping of $Zn^{2+}$ Ions into HA

Zn ion has +2 charge and replaces with $Ca^{2+}$ ions. It increases the bioactivity of HA [132, 133]. Moreover, it results in osteoclastic inhibition [132]. Increase in $Zn^{2+}$ concentration makes the HA solubility higher [134]. Increase in solubility enables cell attachment. It was also known that when HA was doped with 2% by moles $Zn^{2+}$, an increase was seen in cell attachment when compared with pure HA [133]. Moreover, another study reported that between 0.6 and 1.2% by weight $Zn^{2+}$ doped in HA, helped cell proliferation [135]. Addition of $Zn^{2+}$ increases the alkaline

phosphatase activity which is the indicator of cell functionality [136]. Moreover, $Zn^{2+}$ doping into HA causes decrease in grain sizes [137].

#### 1.4.2.2.Doping of $F^-$ Ions into HA

$F^-$ ion is found in enamel layer, blood plasma and saliva. It has an important role in bone and tooth metabolism [138]. $F^-$ ion competes with $OH^-$ ion. It decreases the solubility of the HA and increases HA density after sintering. The increase in density results in improvement in strength and hardness by two or four fold when compared with pure HA [139].

Crystallinity is improved by addition of $F^-$. Therefore, it is used in osteoporosis therapy [139-141]. Moreover, $F^-$ doped HA increases collagen synthesis and alkaline phophatase activity thus affects the cell proliferation indirectly. Biocompatibility also increases when compared with pure HA. However, no significant change was observed in cell attachment [142,143].

#### 1.4.2.3. Doping of $Cl^-$ Ions into HA

$Cl^-$ ion is an ion similar to $F^-$. These two are located in the same group in periodic table. The effect of these two ions on HA is also very similar. $Cl^-$ ion also competes with $OH^-$ ion.

Biological effects of $Cl^-$ ion are also known [144]. $Cl^-$ ion increases the acidity of the bone surface. This change on the bone surface results in osteoclast activation. In the bone resorption process, decrease in pH results in increase in solubility of alkaline salts of bone mineral and increase the secretion of acid hydrolases which is used to digest organic matrix by osteoclasts [144]. The mechanism of acidification depends on the proton pump and chloride ion channel that is located on the cell membrane of the osteoclasts. As a result of coordination between these proton pump and chloride ion channel, transcellular movement of HCl into bone resorption area is provided.

$Cl^-$ effect on structural properties was also investigated. Chloroapatite that is obtained by $Cl^-$ substitution of all $OH^-$ sites, has bigger a and smaller c lattice

parameters than pure HA and fluoroapatite have [144]. Moreover unit cell volume of the chloroapatite is bigger than pure HA and fluoroapatite [144].

### 1.4.3. Co-doping of Various Ions into HA

Co-doping of HA is a common technique to alter the mechanical and biological properties of HA [144-148].

In a study, $F^-$ and $Cl^-$ co-substitution in HA was investigated. The precipitation method was used for synthesis. Unit cell parameters showed that the apatite structure was remained. There was an increase in c-axis parameter as the concentration of ions increased [144]. The crystal size was calculated as 50nm which was in accordance with bone mineral [144].

There was another study which investigated the photoluminesent properties of $Sb^{3+}$ and $Mn^{2+}$ co-doped HA. These two ions were substituted with $Ca^{2+}$ ion. The samples were prepared by hydrothermal synthesis method. By adjusting the ratio of $Sb^{3+}/Mn^{2+}$, luminescent properties of HA could be improved [145].

The co-doping of $Mg^{2+}$ and $CO_3^{2-}$ ions alters the cell viability on HA. However, cell differentiation results showed that pure HA was superior to $Mg^{2+}$ and $CO_3^{2-}$ co-doped samples [146].

$Mg^{2+}$ and $F^-$ co-doped samples were synthesized [147]. Their effects on structural, mechanical and biological properties were observed [147]. According to the results, $Mg^{2+}$ addition did not have a significant effect on the density of HA [147]. However, when $Mg^{2+}$ was doped with $F^-$ ion, the density of HA increased. As $Mg^{2+}$ concentration increased, density started to decrease. Moreover, increase in $Mg^{2+}$ addition triggered the β-TCP formation when the samples were sintered at 1100°C for 1h [147]. Grain sizes of the samples decreased as expected. The microhardness values were also investigated and it could be said that $Mg^{2+}$ ion resulted in decrease in Vickers microhardness [147]. However, with $F^-$ addition, microhardness values improved [147]. Osteoblast adhesion was also investigated for the samples. It was found that up to a limit, $Mg^{2+}$ addition increased osteoblast

adhesion [147]. However, when $Mg^{2+}$ and $F^-$ were co-doped, the osteoblast adhesion increased as the amounts of doping increased [147].

In another study, $Y^{3+}$ and $F^-$ ion incorporation together was investigated in terms of structural and mechanical properties [148]. Three different sintering temperatures were used in experiments. Densities of the samples decreased with $Y^{3+}$ addition when they were sintered at 900°C and 1100°C [148]. In terms of mechanical test, diametral strength test was applied. The composition with 2.5 mol.% $Y^{3+}$ and 2.5 mol.% $F^-$ gave the highest value for the diametral strength when compared with 5 and 7.5 mol.% $Y^{3+}$ and 2.5 mol.% $F^-$ doped samples [148].

### 1.4.4. Mechanical Properties of HA

HA is a ceramic material which has different properties according to the sintering temperatures and duration. Therefore, mechanical properties such as bending, compressive and tensile strengths are represented in ranges [149]. According to the results, compressive strength of HA was between 120 and 150 MPa, bending strength was between 38-250 MPa and tensile strength was between 38 and 300 MPa [149]. These results were also affected by porosity, impurity etc.

Modulus of elasticity had the range from 35 to 120 GPa for dense HA which was sintered at 1000-1100°C [149]. These results showed that HA is a brittle material. Low fracture toughness values are also the indicator of the HA brittleness [150]. Moreover, it was also investigated that fracture toughness of HA increased with decreasing porosity. It showed almost a linear trend. When dense HA was sintered between 1100 and 1150°C, fracture toughness increased with temperature. However, no significant change was observed when dense HA was sintered between 1150 and 1250°C [130]. Above 1250°C, fracture toughness value dropped down and showed a smaller value than fracture toughness at 1100°C [130].

Some properties like density, grain size, Young's modulus and bending, compressive, flexural, torsional and dynamic torsional strengths of dense HA increase when sintering temperature increases from 1150 to 1350°C [130]. HA sythesized by gel-casting method was also investigated by sintering at different

temperatures. It was observed that the samples sintered at 1250°C showed the highest flexural strength with the value of 86.6 MPa [150]. Moreover, the measured Young's modulus was 138 GPa [150]. Above this temperature, strength value decreased. This was due to the abnormal grain growth of the samples. At lower temperatures (1100-1200°C) flexural strength decreased due to low relative density and increase in porosity. Hardness values were also investigated. The hardest material was obtained with the value 4.45 GPa when sintering temperature was 1200°C. Above that temperature there was a slight change in hardness whereas below that temperature hardness decreased dramatically due to retardation in densification Vickers microhardness was also measured and found as 4.5 GPa for dense HA [130].

The porous HA shows anisotropic biomechanical properties and the values can be given in a wide range [151]. A study about the anisotropy of HA crystals showed that in the crystallographic direction of (0001), Young's modulus (150.4 GPa) and hardness (7.06 GPa) values gave higher results than Young's modulus (143.6 GPa) and hardness (6.41 GPa) of HA in the direction of (1010) [152].

In a study bending strength was measured in air (500 MPa) and in water (454 MPa) for a single crystal of HA [153]. These values were about 2.5 times higher than bending strength for dense HA (113-196 MPa) [153].

In another study, elastic properties of HA were investigated by measuring the speeds of ultrasonic waves. According to this study, Young's modulus, shear modulus and compressive strength increased as sintering temperature increased from 1140°C to 1340°C whereas Poisson's ration decreased [154]. When these values were normalized, it can be seen that between 1200 and 1280°C, there was a plateu region before further increase. This stemmed from the fact that three different process took place at the same time in microstructure development [154]. These processes were growth of HA grains, densification and pore shape change.

#### 1.4.4.1. Mechanical Properties of Doped HA

HA has a brittle nature. However, by addition of some ions, its mechanical properties can alter.

There were studies in which $Mg^{2+}$ and $Zn^{2+}$ ions were used as dopants [155]. Different amounts of these ions were doped into HA. In terms of density, it was observed that MgO doped HA with 1 wt. % had the higher density than with same amount of ZnO doped samples [155]. When, the percentage increased, the density started to decrease. In terms of Vickers hardness, it can be said that both $Mg^{2+}$ and $Zn^{2+}$ improved the hardness of HA [155]. According to compressive test results, HA sintered at 1300ºC had the compressive strength of about 210 MPa whereas ZnO doped samples had about 280 MPa and MgO doped samples had 223 MPa [155]. Therefore, it was concluded that doping of ZnO and MgO improved the mechanical properties of HA.

Silver is another element that can doped in HA. It was investigated that, as silver ion concentration increased, the surface hardness of the layers HA doped with silver ions decrased [156].

Strontium is another ion that can be doped into HA. This ion alters the crystallinity of HA by substitution $Ca^{2+}$ via inhibiting β-TCP formation [157]. The strontium doped samples have higher density and low porosity. When the compressive strength was measured, it was found that 10 mole% addition of strontium ion increased compressive strength of pure HA by 4 fold. For pure HA this value was found as 0.25 MPa, whereas for 10 mole% strontium doped HA this value was 0.94 MPa [157].

### 1.4.5. Biologial Properties of HA

HA is a biocompatible and bioactive material that can make chemical bonds with bone [158]. However, some properties of HA increase the rate of vascularization and bone ingrowth. Porosity is one of the important properties that affect the biological properties of bone when an optimum value is obtained [158].

Surface topography that is highly related with porosity has an important role in osteoblast proliferation, adhesion and cell phenotype [158]. Moreover, surface enegy is dependent on surface topography. Some proteins that are useful for bone cell attachment are highly affected by the surface energy.

Highly porous HA with pore diameter of 400 μm, increases cell infiltration and migration [158]. In two weeks, cell spreading and proliferation of bone progenitor cells can be seen. These cells start to fill the pores of HA. Within one month of incubation, cells starts to produce their own environment by filling some pores and leaving some channels for media flow. Moreover, it is recommended that for the proper capillary bed formation, the pore size of the implants should be greater than 300 μm [158].

In vitro testing was also done for HA. According to these tests, HA with the pore size from 400 to 1600 μm resulted in bone regeneration and bone morphogenic protein attachment at the interface which was the indicator of osteoinductive characteristics of HA [159].

Crystallinity is another property that affects the biological porperties of HA. HA scaffolds with micro and nano crystals were investigated in terms of biology. It was observed that connective tissue ingrowth and new bone formation were seen after 12 weeks [158]. Between the control group without HA scaffold and with micro and nano crystalline HA scaffolds, it can be seen that nano crystalline HA scaffolds had higher bone area percentage [158]. Moreover, the formed bone in the control group showed trabecular bone properties.

To enhance the biological properties, the HA scaffolds should be modified. One common modification is the addition of some bone morphogenic proteins to increase the cell attachment thus better implant fixation.

#### 1.4.5.1. Biological Properties of Doped HA

In a study, the effect of ZnO and MgO dopants were investigated in terms of biodegradability. It was investigated that HA had the highest weight loss. Moreover

in doped samples no weight loss was seen up to 14 days [155]. The least degradation was seen in MgO doped HA [155].

Silver can also be doped in HA. This element has an ability to inhibit bacterial adhesion. It is strongly toxic for many micro-organisms. Therefore, it is very useful in medical applications. However, it exibits low toxicity in human body [156]. Silver can be doped by various methods such as sol-gel, ion implantation, electrochemical deposition, thermal spraying, ion exchange, coprecipitation and sputtering. In a study, silver doped HA prepared by sol-gel method was investigated in terms of biological properties [158]. According to the results, silver doped HA samples had lower contact angle which meant having higher hydrophilicity than pure HA. Moreover, it was found that less bacterial adhesion was observed in samples doped with silver. However, in terms of cell proliferation and differentiation silver doped samples and pure samples gave the same results [158].

Magnesium was also doped into HA and biological properties were tested. According to the results, $Mg^{2+}$ doping resulted in increase in viability. For HA the value was 75% whereas for $Mg^{2+}$ doped HA viability value became 81% [146]. There was also an increase in alkaline phosphatase activity which was an indicator of cell differentiation in $Mg^{2+}$ doped samples.

The biological properties of strontium doped HA were also investigated. In a study the material was applied as coating for implants. The interaction with osteoblasts and osteoclasts was observed. According to the results of osteoblast proliferation, alkaline phosphatase activity, collagen type 1 production and osteocalcin production increased as strontium amount in HA samples increased [159]. It was also found that strontium doping with a concentration higher than 3 at.% resulted in osteoclast inhibition [159]. However, in another study, there was no significant difference in alkaline phosphatase activity and $Ca^{2+}$ incorporation except 20 μg/ml and 100 μg/ml strontium doped HA [160]. In these two concentrations, decrease in alkaline phosphatase activity and $Ca^{2+}$ incorporation were seen.

Manganese incorporation into HA was also investigated in terms of biological properties. It was found that DNA content, cell viability and total protein amount decreased when manganese was doped into HA [161] . However, it was concluded that up to 7 days, it helped cell spreading [161]. After 7 days, direct contact with this material affected cells negatively.

Silicon can also be doped into HA. In a study, surface morphologies of silicon doped and undoped HA were investigated [162]. It was found that dissolution of silicon doped HA formed a Ca and Si rich environment on the surface of the material [162]. This environment enhanced cell proliferation and differentiation.

Yttrium, cadmium, zinc and magnesium were doped separately into HA and their biological properties were investigated [163]. According to the results, yttrium gave highest results in terms of vitronectin, collagen and calcium adsorption. Moreover, as yttrium concentration increased the calcium adsorption amount also increased. It was also investigated that HA doped with cadmium, magnesium, zinc and yttrium gave higher osteoblast adhesion results than undoped HA gave. Yttrium had the highest osteoblast adhesion among these and as the yttrium amount increased in the samples, osteoblast adhesion also increased [163]. This was due to the fact that yttrium gave the highest results in terms of some protein adsorptions (vitronectin and collagen). These proteins modified the material surface and made easy for the osteoblasts to attach. Moreover, by yttrium effect, these proteins performed conformational changes which made the surface bioactive.

Gadolinium(III) ($Gd^{3+}$) and neodymium(III) ($Nd^{3+}$) are two elements that have good electrical conductivity and have a potential for biomedical field. These two elements were doped into HA. Their cytotoxicity was also investigated by using different concentrations. It was found that there was no cytotoxic effect of neodymium [164]. However, for gadolinium with 0.004 mole concentration had cytotoxic effects. This was due to the fact that gadolinium was a toxic element when it was not incorporated into HA structure. By doping it became stable and did

not have toxic effects. When the amount of $Gd^{3+}$ was high, all ions could not incorporated in the HA structure [164]. Moreover, it was also investigated that when sintering was applied to these materials, other phases appeared in some samples which brought cytotoxicity.

In a study, the differences in osteoblast adhesion in different materials with different dopants such as $Mg^{2+}$, $Zn^{2+}$, $La^{2+}$, $Y^{3+}$, $In^{3+}$, $Bi^{3+}$ were investigated. It was found that doping HA with +3 charged element resulted in better osteoblast adhesion than doping it with +2 charged element [165]. $In^{3+}$ and $Y^{3+}$ gave the best results in terms of osteoblast adhesion. However, for long time adhesion, $Zn^{2+}$ was successful.

## 1.5. Bone

Bone is the main constituent that forms the skeletal system. There are 206 bones in an adult. Bones have five types. These are long, short, flat, irregular and sesamoid bones.

In the body bone has many functions. These functions can be listed into two groups. These are mechanical and metabolical. Mechanical functions can be listed as movement, posture, protection and sound transduction [166]. The metabolical functions are listed as blood cell production, mineral storage, growth factor storage, fat storage, acid-base balance, detoxification [166].

### 1.5.1. Structure of Bone

At the lowest level bone can be thought as a composite material which includes fibrous protein, collagen, calcium phosphate crystals, some other proteins, water, polysaccharides, cells and blood vessels.

Bone has three main parts which can be listed as living part, organic part and inorganic part. Living part is composed of cells of different types. Organic phase is called osteoid and secreted by osteoblast cells. It is 25 % of the bone structure by weight and 50% by volume [167]. It contains 90% collagen Type 1 and 10%

amorphous ground substance which consists of glycoproteins and glycosaminoglycans [167]. Inorganic phase of the bone is 75% by weight and 50% by volume of the total [167]. The inorganic phase is composed of calcium crystals mainly in the form of HA. During bone formation, the organic phase is secreted by osteoblasts. This matrix is then started to mineralize. Hydroxylapatite crystals precipitate between the collagen fibers in an orderly fashion. After a few days, the collagen part becomes 70% mineralized. After several months the organic part becomes fully mineralized [167].

There are two different types of bones in terms of their mechanical properties. These are compact and cancellous bone. Various characteristics of the compact and spongy bone are compared in Table 1.4.

**Table 1.4.** Comparison of cortical and spongy bone [168].

| **Properties** | **Cortical bone** | **Spongy bone** |
|---|---|---|
| Skeletal mass | 80% | 20% |
| Bone surface | 33% | 67% |
| Surface/ volume ratio ($mm^2/mm^3$) | 20 | 2.5 |
| Soft tissue content | ~10 % | ~75 % |
| Turnover period | Long | Short |
| Function | Biomechanical, supportive and protective | Supportive and mineral homeostasis |

### 1.5.2. Mechanical Properties of Bone

In this section mechanical properties are investigated for the compact bone and spongy bone.

#### 1.5.2.1. Mechanical Properties of Compact Bone

Compact bone is formed and becomes thickest where stress is applied from a limited range of directions. All of the osteons in the compact bone are ordered in the same directions and make the structure strong in that direction. However, the structure is weak and can easily bent at the direction perpendicular to the alignment of osteons. [168].

Moreover, when compression force is applied in the direction of osteon alignment due to body weight on the medial side of the bone, the tension is experienced on the lateral side. Therefore, high stress is applied on both sides of the bone which stimulates the compact bone formation.

##### 1.5.2.1.1. Elasticity

The compact bone is assumed to be transversely isotropic or orthotropic which means different properties along the direction of the each axis. It was accepted that there were three directions in a transversely isotropic material. These were radial, circumferential and longitudinal relative to the long axis of the bone. [169, 170]. The stiffness of the length of the bone was found to be 1.6 to 2.4 times greater than the width [168].

Another mechanical property of bone is the viscoelasticity. Bone is a slightly viscoelastic material [167]. Demineralization has a dramatic effect on yield strength. It results in decrease by about 48% of yield strength when the mineral content of bone is reduced by half. When the tissue is fully demineralized, there is no yield strength observed [167].

##### 1.5.2.1.2. Strength

Strength is another property that changes according to the directions. It was found that the bone became stronger and resistant to failure when it was loaded longitudinally rather than circumferentially. In Table 1.5, the values corresponding to Human Haversian system is represented. According to Table 1.5, bone is stronger when it is loaded in compression than loaded in tension [167].

**Table 1.5.** Strength properties of human haversian bone (MPa) [167].

| **Strength Properties** | | **Logitudinal** | **Circumferential** |
|---|---|---|---|
| **Tension** | Strength | 133 | 53 |
| | Yield Stress | 114 | 141 |
| | Ultimate Strain | 0,031 | 0,007 |
| **Compression** | Strength | 205 | 131 |
| | Ultimate Strain | 0,019 | 0,05 |
| **Shear** | Strength | 67 | 67 |

There is no specific value for fatigue properties. Type of bone and load, the amount and time of application, and temperature affect the values of fatigue properties. However, it has been shown that, the greater the density of the bone is, the longer the fatigue life of the bone becomes [168].

#### 1.5.2.2. Mechanical Properties of Cancellous Bone

Mechanical properties of cancellous bone are less well understood. However, it was investigated that, spongy bone was found low stressed areas and stressed areas from many directions. Cancellous bone is lighter that the compact bone. Therefore, it reduces the weight of the skeleton and helps muscles indirectly. Moreover, it is less stiff and much weaker than compact bone.

Porosity is another important property that affects the mechanical features of the cancellous bone. Cancellous bone is highy porous, inhomogenous and anisotropic. Therefore, the measured elasticity of modulus values were quite different. The range of elasticity of modulus for cancellous bone was found between 1 and 20 GPa [167]. Moreover, cancellous bone has the energy absorption ability [168].

### 1.5.3. Cells, Organic and Inorganic Parts of Bone

Bone can be thought as a composite of organic and inorganic materials with different types of cells embedded in.

#### 1.5.3.1. Bone Cells

There are four different type of bone cells. These are osteocytes, osteoclasts, osteoblast and osteoprogenitor cells.

Osteocytes are the most abundant type of cells. They have two main functions. The first function is maintaing the protein and mineral content of the surrounding matrix by secreting chemicals that dissolve the matrix [167, 168]. As the matrix is dissolved, minerals are released. Then, osteocytes make a new matrix. Therefore, hydroxylapatite crystals can be embedded in this new matrix. The second function is repairing of damaged bone [167,168]. Osteocytes can easily be converted into less specialized type of cells such as osteoblasts and play an active role in synthesis of new matrix [167].

Osteoblasts are the cells that produce new bone matrix called osteoid by making and releasing proteins and other organic components. This process is called osteogenesis [167, 168]. Osteoblasts also stimulate the deposition of calcium salts by increasing the concentration above their solubility limits. Therefore, this type of cells stimulate the transformation of osteoid to bone [167, 168].

Osteoclasts are cells responsible for osteolysis process [167, 168]. This process includes matrix decomposition by acids and proteolytic enzymes. After the dissolution of the matrix, the stored minerals are released. The balance between osteoblasts and osteoclasts is very important due to their opposing activities.

Osteoprogenitor cells are another cell type which are differentiated into osteoblasts. When there is a fracture, they become active and forms osteoblast population [167,168].

### 1.5.3.2. Organic Content of the Bone

As it was mentioned earlier, the organic part of the bone was composed of collagen type I with a percentage of 90, and amorphous ground substance that was primarily composed of glycoproteins and glycosaminoglycans with a percentage of 10 [171].

The non-collagenous proteins of the bone have some important roles in initiation and control of mineralization and reconstruction. It was also known that, this proteins especially glycoproteins had an important role in binding the collagen and mineral together [171]. The non-collagenous proteins in bone can be separated into five main groups. These are glycoprotein, glycoaminoglycan, gamma-carboxyl glutamic acid, RGD-containing glycoprotein and serum protein [171].

### 1.5.3.3. Inorganic Content of the Bone

Inorganic phase of the bone is composed of mainly amorphous HA which has the formula of $Ca_{10}(PO_4)_6(OH)_2$. However, it has more specialized structure. Bone mineral can also be classified as calcium deficient apatite and hydroxide deficient apatite. It has crystal size of about 20×40×200 Å [172]. Due to its small size bone mineral crystal can be easily substituted by some vaious ions. These ions can be classified as anions and cations. Cations found in the bone structure are $Mg^{2+}$, $Sr^{2+}$, $Fe^{2+}$, $Pb^{2+}$, $Na^{+}$, $K^{+}$ whereas the anions are $CO_3^{2-}$, $F^{-}$, $HPO_4^{2-}$ and $H_2PO_4^{-}$. The mineral part constituents are summarized in Table 1.6 with their amounts in wt % range for healthy adult bone ash [171, 173].

The closest synthetic structure to bone mineral structure was accepted as dahllite crystals which was carbonated hydroxylapatite with general formula $Ca_5(PO_4,\ CO_3)_3OH$. However, it was investigated by atomic force microscopy (AFM) that the crystals of bone was plate like shaped whereas the carbonated hydroxylapatite had an hexagonal structure [173]. It was suggested that octacalcium phosphate was converted into the bone mineral due to its similarity to the apatitic structure and plate-like shaped crystals [173]. One difference between octacalcium phosphate and bone mineral is that octacalcium phosphate has an hydrated layer in

one axis. This hydrated layer grows slowly during the formation of crystals. Therefore, a structure similar to the apatitic structure is formed [174].

Bone mineral formation is not well understood process. However, it was suggested that first brushite was formed. After formation of brushite, it was resdissoved and amorphous calcium phosphate formation was seen. The amorphous calcium phosphate was converted into octacalcium phosphate. As a last step, it was converted into hydroxylapatite which was the most insoluble phase among calcium phosphates [175].

**Table 1.6.** The chemical composition range of healthy adult bone ash [29,173].

| **Ions** | **Range of amount (wt%)** |
|---|---|
| Calcium | 32.6-39.5 |
| Phosphorus | 13.1-18.0 |
| Water | 10 |
| Carbonate | 3.2-13.0 |
| Magnesium | 0.32-0.78 |
| Sodium | 0.26-0.82 |
| Chloride | 0.13 |
| Pyrophosphate | 0.07 |
| Citrate | 0.04-2.67 |
| Potassium | 0.03 |
| Fluoride | 0.020-0.207 |

### 1.5.4. Presence of Ions in Bone

There are many different ions that incorporate into bone structure. Most of these ions are found in trace amounts. The examples of these ions are $F^-$, $Sr^{2+}$, $Cu^{2+}$, $Si^{2+}$ and $Zn^{2+}$. Among these ions, $F^-$ and $Sr^{2+}$ are found only in mineral phase, $Cu^{2+}$ and $Si^{2+}$ ions are found only in organic phase and $Zn^{2+}$ is found in both organic and

mineral phase [176]. Some metal ions that can be incorporated into the bone structure are magnesium, aluminium, boron, cadmium, chromium, lead other than strontium and silicon.

The magnesium is an element with 2+ ionic charge. The 50-60 % of total $Mg^{2+}$ is found in bone. It is 0.5-1% of the bone ash [176]. Two thirds of the skeletal Mg content is incorporated into the HA structure and can be released during bone resorption. $Mg^{2+}$ has direct and indirect effects on bone crystallization. As a direct effect, it can be said that, $Mg^{2+}$ ions compete with calcium ions in growth of HA and amorphous calcium phosphate and retard this process. Moreover, in vivo studies showed that as $Mg^{2+}$ content icreased, the crystal size decreased. Besides the crstal size, crystallinity index also decreased as $Mg^{2+}$ content increased [176].

The indirect effect of $Mg^{2+}$ on bone crystallization is related with osteocalcin formation and osteocalcin binding to HA. Osteocalcin inhibits the transformation of HA from brushite and nucleation of mineral formation. $Mg^{2+}$ has positive effect of osteocalcin. Therefore, as $Mg^{2+}$ amount decreases, osteocalcin amount decreases, which results in altered mineralization. However, this ion can also close the available HA binding sites of osteocalcin which inhibits the function of osteocalcin and thus increase mineralization [177].

$Al^{3+}$ is another metal ion that competes with calcium and inhibits the mineralization. The amount of $Al^{3+}$ in the bone is very low and has a value 5-7 mg/kg in dry bone [178]. Moreover, $Al^{3+}$ has a positive effect on osteoprogenitor cells and osteoid nodules.

The metal boron has not a significant effect on soft tissue calcium amounts, bone mineral density, bone weight and bone Ca, Mg and P amounts. However, it was investigated that this metal ion increased calcium absorption.

Cadmium is another important metal that can be incorporated into the bone structure. It was reported that cadmium defiency resulted in decrease in mechanical properties of bone. Moreover, it decreases the calcium absorption with increasing calcium loss and thus bone resorption. By direct interaction with bone cells, it decreases the mineralizing ability of them. Moreover, by inhibiting some proteins, it

decreases collagen production. This metal changes the morphology of bone cells and decrases the amount of osteoblasts and osteoclasts. Therefore, it can be concluded that cadmium has an inhibitory effect on HA nucleation and growth. It is found in blood with a concentration 0.23-0.29 parts per billion [178]. More than this value results in toxicity, thus kidney damage would occur.

Lead also incorporates into the bone structure. This ion exactly behaves like $Ca^{2+}$ ion. However, higher values results in toxicity. 90% by weight of all $Pb^{2+}$ in the body is beared by bones [178]. Little dose of $Pb^{2+}$ in medium of cells was found to increase the calcium ion concentration. If the dose was increased, it resulted in supression of alkaline phophatase, endochondrial bone formation, collagen type II and X production. It was also reported that, $Pb^{2+}$ compete with $Ca^{2+}$ in binding to osteocalcin which regulates the bone mineral dynamics. It also inhibited the release of osteonectin in cells [178]. Moreover, it was also investigated that $Pb^{2+}$ increased the intracellular concentrations of cAMP and $Ca^{2+}$ which stimulated the osteoclast-like cells [178].

Silicon is another element that is found in bone structure. It was reported that silicon increased the mineralization whereas $Si^{4+}$ deficiency resulted in some deformations in bone shapes [178].

Strontium use the same metabolic pathways with $Ca^{2+}$. It replaces $Ca^{2+}$ and inhibits mineralization and bone formation. Moreover, increase of strontium amounts results in delay in natural progression of osteoid to bone. However, non-toxic amounts of $Sr^{2+}$ used in osteoporosis treatment. It was found that, appropriate amount of $Sr^{2+}$ raised the trabecular calcified bone volume by reducing bone resorption [178]. Moreover, high amounts of $Sr^{2+}$ depressed the bone $Ca^{2+}$ content and deposition rate.

### 1.6. Aim of the Study

In this study, synthesis of nano HA doped with $Zn^{2+}$, $F^-$ and $Cl^-$ ions and investigation of their structural, mechanical and biological properties were aimed. By investigating the structural mechanical and biological properties of synthesized

compositions, a suitable material for biomedical applications such as metal implant coating, tissue engineering, bone substitution should be obtained. Precipitation method was used to synthesize the pure and doped HAs. The samples were dried and sintered at 1100 °C for 1h.

Density of the samples were also measured by using Archimedes' principle. To observe the structural properties, X-ray diffraction (XRD), Fourier Transform Infrared Spectroscopy (FTIR) and Scanning Electron Microscopy (SEM) methods were applied. Phase changes, crystallinity and lattice parameters were observed by XRD method. The specific bonds in the samples and doping amounts were determined by FTIR. By detection of the bonds, it was proved that HA structure is obtained. Moreover, by the detection of $Zn^{2+}$, $F^-$ and $Cl^-$ related bands, ion incorporation to the HA structure were proved. Microstructure of the crystals were observed and grain sizes were determined by SEM. Mechanical properties were investigated by Vickers microhardness test. Microhardness and fracture toughness of the samples were determined by using Vickers microhardness test. After the structural and mechanical investigations, the best composition in terms of structural and mechanical properties was chosen. The chosen compositions should gave the highest density, stability, Vickers microhardness and fracture toughness values and the lowest grain size values. The biological properties of the chosen composition were investigated.

Alamar Blue™ assay and Alkaline Phosphatase Activity (ALP) assay were done to observe biological properties. Saos-2 cell line was used for in vitro tests. Cells were seeded on the pure HA and doped HA disks. Alamar Blue™ assay was applied to determine cell viability and proliferation. ALP assay was used to determine osteogenic activity of the cells. Moreover, SEM pictures were used to observe the cell morphology. Dissolution test was also done in simulated body fluid (SBF) and the changes were observed by SEM.

This study investigated $Zn^{2+}$ and $Cl^-$ co-doped samples in terms of some mechanical and structural properties for the first time. It was important due to the fact that there was little information about $Cl^-$ doped HA in literature which

included chlorapatite, $F^-$ and $Cl^-$ co-doped HA. Moreover, $Zn^{2+}$ and $F^-$ co-doped samples were also synthesized and investigated in terms of structural, mechanical and biological properties for the first time. This study also included very detailed FTIR observations of HA different from other studies.

# CHAPTER 2

# MATERIALS AND METHODS

## 2.1. Materials

### 2.1.1. Materials Used in Pure HA and $Zn^{2+}$, $F^-$, $Cl^-$ Doped HA Synthesis

The precursors used to synthesize pure HA were calcium nitrate tetrahydrate ($Ca(NO_3)_2 \cdot 4H_2O$) (Merck, Germany) and diammonium hydrogen phosphate ($(NH_4)_2HPO_4$) (Merck, Germany). For doped samples, besides these precursors additional compounds were required. $Zn^{2+}$ doped samples were prepared with zinc nitrate hexahydrate ($Zn(NO_3)_2 \cdot 6H_2O$) (Riedel-deHaën, Germany). $F^-$ doped samples were prepared with ammonium fluoride ($NH_4F$) (Aldrich, Germany). Calcium chloride dihydrate ($CaCl_2 \cdot 2H_2O$) (Fisher Scientific, USA) were used for $Cl^-$ doped samples. The pH adjustment was made by ammonia solution ($NH_4OH$) (Merck, Germany).

### 2.1.2. Materials Used in Cell Culture Studies

In cell culture studies, for cell proliferation medium Dulbecco's Modified Eagle Medium with high glucose and fetal bovine serum (FBS) were obtained from Biochrom, Germany. For Alamar Blue™ assay, Alamar Blue™ was provided by Invitrogen, USA. Penicilin-streptomycin was obtained from PAA Laboratories GmbH, Austria. For differentiation medium, L-ascorbic acid, β-glycerophosphate and dexamethasone were purchased from Sigma, Germany. Dimethly sulfoxide (DMSO) (molecular biology grade) for cell freezing medium was the product of AppliChem, Germany. Trypsin-EDTA used for cell detachment was obtained from PAA laboratories GmbH, Austria. For SEM specimen preparation, gluteraldehyde, cacodylic acid and hexamethyldisilizane (Sigma-Aldrich, Germany), 96 % ethanol

(Ryssen, France) and 100 % ethanol (Merck, Germany) were used. For Alkaline Phosphatase Activiy (ALP) assay and Bicinchioninic Acid (BCA) assay, Triton X-100, sodium azide, p-NPP, p-nitrophenol, bichiconic acid and cupric sulfate were provided from Sigma, Germany. Bovine Serum Albumin (BSA) was the product of PAA Laboratories GmbH, Austria .

For dissolution tests, SBF was prepared by using NaCl, $MgCl_2 \cdot 6H_2O$, $MgSO_4 \cdot 7H_2O$ from Merck, Germany, $NaHCO_3$, KCl, $CaCl_2 \cdot 2H_2O$, HCl from Riedel-deHaën, Germany, $K_2HPO_4$ obtained from Fluka, Switzerland and Tris ($(CH_2OH)_3CNH_2$) obtained from Bio-rad, France.

## 2.2. Methods

### 2.2.1. Synthesis of HA Samples

#### 2.2.1.1. Synthesis of Pure HA Samples

Precipitation method was used to produce pure HA samples. The precursors for this method were calcium nitrate tetrahydrate ($Ca(NO_3)_2 \cdot 4H_2O$) and diammonium hydrogen phosphate ($(NH_4)_2HPO_4$). These two powders were dissolved separately in distilled water with different amounts to obtain a theoretical Ca/P ratio of 1.67 and stirred 1h. At the end of 1h stirring, some ammonia solution ($NH_4OH$) was added to the solution with diammonium hydrogen phosphate ($(NH_4)_2HPO_4$) and the solution was left for stirring for 10 minutes. Then, calcium nitrate tetrahydrate ($Ca(NO_3)_2 \cdot 4H_2O$) solution and some ammonia solution were added dropwise. Ammonia was added to adjust the pH level between 11 and 12. Then, the final mixture was left for stirring and the heater was turned on to speed up the reaction. The final mixture was heated until it was boiled. After boiling for 10 minutes, the heater was turned off and the boiled mixture was left for stirring overnight. The prepared mixture was then left for aging for 1 day. After 1 day, the mixture was filtered using a vacuum filter. By filtration with a fine filter paper, a wet cake was obtained. The wet cake was dried overnight at 200ºC to remove excess water and ammonia. The dried samples were sintered at 1100ºC for 1h.

### 2.2.1.2. Synthesis of Doped HA Samples

In addition to precursors (calcium nitrate tetrahydrate and diammonium hydrogen phosphate), zinc nitrate hexahydrate ($Zn(NO_3)_2 \cdot 6H_2O$) for $Zn^{2+}$ doped samples, ammonium fluoride ($NH_4F$) for $F^-$ doped samples, calcium chloride dihydrate ($CaCl_2 \cdot 2H_2O$) for $Cl^-$ doped samples were used. 15 different compositions were prepared. These compositions were grouped into four. These are F group, 2Zn F group, Cl group, 2 Zn Cl group. $Zn^{2+}$ amount was kept constant in all compositions with the value 2 mol.%. Table 2.1 summarizes the amounts of doping by mole percentage and naming for all samples.

**Table 2.1.** Naming, percentages of doping by mole and Ca/P ratio for prepared samples.

| Sample Name | Mole % $Zn^{2+}$ | Mole % $F^-$ | Mole % $Cl^-$ | Ca/P |
|---|---|---|---|---|
| Pure | 0 | 0 | 0 | 1.67 |
| 2 Zn | 2 | 0 | 0 | 1.63 |
| **F group** | | | | |
| 1 F | 0 | 1 | 0 | 1.67 |
| 2.5 F | 0 | 2.5 | 0 | 1.67 |
| 5 F | 0 | 5 | 0 | 1.67 |
| **2 Zn F group** | | | | |
| 2 Zn 1 F | 2 | 1 | 0 | 1.63 |
| 2 Zn 2.5 F | 2 | 2.5 | 0 | 1.63 |
| 2 Zn 5 F | 2 | 5 | 0 | 1.63 |
| **Cl group** | | | | |
| 1 Cl | 0 | 0 | 1 | 1.67 |
| 2.5 Cl | 0 | 0 | 2.5 | 1.67 |
| 5 Cl | 0 | 0 | 5 | 1.67 |
| **2 Zn Cl group** | | | | |
| 2 Zn 1 Cl | 2 | 0 | 1 | 1.63 |
| 2 Zn 2.5 Cl | 2 | 0 | 2.5 | 1.63 |
| 2 Zn 5 Cl | 2 | 0 | 5 | 1.63 |

To obtain doped samples, the precursors calcium nitrate tetrahydrate and diammonium hydrogen phosphate were used. For $Zn^{2+}$ addition, zinc nitrate

hexahydrate was added to calcium nitrate tetrahydrate solution. The compound calcium chloride dihydrate was added to calcium nitrate tetrahydrate solution for $Cl^-$ addition. For $F^-$ doped samples, ammonium fluoride was added to diammonium hydrogen phosphate solution.

The mole amounts were changed according to doping percentages. For pure HA, 0.075 moles of calcium nitrate tetrahydrate and 0.045 moles of ammonium hydrogen phosphate were used. The 2 mol.% $Zn^{2+}$ doped HA included 0.0735 moles of calcium nitrate tetrahydrate, 0.045 moles of diammonium hydrogen phosphate and 0.0015 moles of zinc nitrate hexahydrate.

The F group without Zn, had 0.0075 moles of calcium nitrate tetrahydrate and 0.0045 moles of diammonium hydrogen phosphate. However, ammonium fluoride mole amounts changed. It was 0.00075 for 1% F, 0.00188 for 2.5% F and 0.00375 for 5% F. The F group with 2% Zn included same amounts of calcium nitrate tetrahydrate, diammonium hydrogen phosphate with mole amounts of 0.0735, 0.045 and 0.0015, respectively. However, ammonium fluoride amounts changed and had the values of 0.00075, 0.00188 and 0.00375 for 1% F, 2.5% F and 5% F, respectively.

The Cl group without Zn, had the same mole amount of diammonium hydrogen phosphate with the value 0.0044. However, calcium nitrate tetrahydrate mole amounts changed due to the presence of $Ca^{2+}$. The calcium nitrate tetrahydrate used in terms of moles could be listed as 0.07493 for 1% Cl, 0.07481 for 2.5% Cl, 0.07463 for 5% Cl. Calcium chloride dihydrate mole amounts were listed as 0.00075 for 1% Cl, 0.00188 for 2.5% Cl and 0.00375 for 5% Cl. The Cl group with 2% Zn included same amounts of diammonium hydrogen phosphate and zinc nitrate tetrahydrate with mole amounts of 0.045 and 0.0015, respectively. However, calcium nitrate tetrahydrate amounts were changed with the mole amounts 0.07343 for 1% Cl, 0.07331 for 2.5% Cl and 0.07313 5% Cl. Moreover, calcium chloride dihydrate mole amounts were also different with the values 0.00075 for 1% Cl, 0.00188 for 2.5% Cl and 0.00375 for 5% Cl.

After stirring the solutions separately for 1h, they were mixed with the same procedure corresponding to the pure HA synthesis. Then, the mixture was boiled up to 10 minutes and left for stirring overnight. After that, the mixture was aged for 1 day. After aging, filtration with fine filter paper using a vacuum filter was applied and wet cake was obtained. The wet cake was dried overnight at 200ºC. The dried samples were sintered at 1100ºC for 1h.

### 2.2.2. Characterization Methods

#### 2.2.2.1. Structural Characterization

##### 2.2.2.1.1. Density Measurements

Archimedes method was used to determine the densities of the samples. This method is based on the formula;

$$d=m/V \tag{2.1}$$

Where d is density, m is mass and V is the volume of the sample.

By using the Precisa Gravimetrics Density Determination Kit, first the dry weight of the sintered samples were measured by putting the sample in the upper part of the kit. Then, the weight of the samples in distilled water were measured by putting the sample in the lower part of the kit. The volume (V) of the samples were calculated by using this formula:

$$V= \text{dry weight-wet weight} \tag{2.2}$$

Then the density formula becomes with d is density;

$$d=\text{dry weight}/(\text{ dry weight-wet weight}) \tag{2.3}$$

The theoretical density of pure HA is 3.156 g/cm$^3$. By using this value, relative densities of the pure and doped HA samples were calculated.

#### 2.2.2.1.2. X-Ray Diffraction Analysis

X-Ray diffraction analysis was performed by a Rigaku DMAX 2200 device. The phases present in the samples and lattice parameters were calculated by using X-Ray diffraction results. Cu-$K_\alpha$ radiation at 40 kV/ 40 mA was used for XRD analysis. The samples were scanned from $20^o$ to $70^o$ in 2θ with a scanning step size of $2.0^o$/min. To compare the positions of diffracted planes Joint Committee on Powder Diffraction Standards (JCPDS) files were used.

##### 2.2.2.1.2.1. Lattice Parameter Calculation from XRD Results

It was mentioned that HA has a hexagonal unit cell structure with lattice parameters of "a" and "c". To calculate these parameters, Rietvelt analysis method was applied by using the General Structural Analysis System (GSAS) computer program.

After finding "a" and "c" parameters, the hexagonal unit cell volumes were calculated by using the formula below [179];

$$V = 2.589(a^2)c \tag{2.4}$$

The fraction of crystalline phase was calculated by using the formula below [180];

$$X_c \approx 1 - (V_{112/300}/I_{300}) \tag{2.5}$$

Where $X_c$ is the fraction of crystalline phase, $V_{112/300}$ is the intensities of the hollow between (1 1 2) and (3 0 0) planes and $I_{300}$ is the intensity of (3 0 0) plane. The hollow between (1 1 2) and (3 0 0) planes disappears completely in non-crystalline samples.

#### 2.2.2.1.2.2. Grain Size Determination from XRD Results

Grain sizes were investigated by using XRD patterns. Rietwelt analysis was applied to the samples and Lorenzian crystallite sizes of the samples were detected. By using the Lorenzian crystallite size obtained from GSAS computer program, the grain sizes of the samples were calculated by using the formula below [181];

$$P = \frac{(18000 \times K \times \lambda)}{(\pi \times L_x)} \tag{2.6}$$

In this formula,

P: grain size; K: 0.85-1.00 (selected as 0.90 here); λ: Cu Kα (1.54056 A); Lx: Lorenzian crystallite size obtained from GSAS computer program.

#### 2.2.2.1.3. Scanning Electron Microscopy (SEM) Analysis

A JEOL JSM-6400 (JEOL Ltd., Japan) SEM at a voltage of 15 kV was used to examine the samples. The samples were displayed with 30000X magnification.

#### 2.2.2.1.4. Fourier Transform Infrared Spectroscopy (FTIR)

FTIR spectra were used to identify the presence of bonds formed in the doped and pure HA structure. For FTIR spectra, the samples were first crushed with a mortar and pestle. Then, the prepared powders were mixed with potassium bromide (KBr) with 1 to 100 weight ratio. The prepared powder mixtures were dried in vacuum by freeze drying for 1 day. Then, the samples were cold pressed for 8 minutes to obtain transparent pellets. The spectra were recorded from 4000 $cm^{-1}$ to 400 $cm^{-1}$ using a 100 scan on Spectrum One Spectrometer (Perkin Elmer, Norwalk, CT, USA). For the analysis of infrared spectral data, Perkin Elmer Spectrum One software package was used.

Statistical analysis of FTIR studies were done by using Minitab Statistical Software, USA.

#### 2.2.2.2. Mechanical Characterization

##### 2.2.2.2.1. Vickers Micro-hardness

Vickers micro-hardness tester (HMV-2, Shimadzu, Japan) was used to determine the micro-hardness of the samples. The sintered samples were embedded in epoxy molds (Struers, Denmark) for easy handling. Then, the samples were polished on papers with grids 180, 240, 320, 400, 600, 800, 1000 and 1200 successively before examination. Final polishing was applied with 1 μm monocrystalline diamond suspension (Buehler Ltd., USA). After the samples were prepared, a diamond indenter was applied with a load of 200 g for 20 seconds onto the surface of the samples. The diagonal indent shape formed after the indentation was measured to determine the micro-hardness of the samples. 15 measurements were performed on three parallels for each sample. For the calculation, the following formula was used:

$$HV = 0.001854\frac{P}{d^2} \tag{2.7}$$

Where;

HV: Vickers hardness (GPa); P: Applied load (N); d: diagonal indent length (mm).

##### 2.2.2.2.2. Fracture Toughness

Fracture toughness of the samples was also calculated from the cracks generated by the indentations applied during the micro-hardness test. Fracture toughness can be calculated by using two different approaches depending on the size of the cracks formed by indentation.

The two shapes of the cracks are presented in Figure 2.1. According to the approaches, Halfpenny shape cracks were formed when the ratio of c/a was greater than 3, whereas the Palmqvist shaped was observed when the ratio of c/a was less than 3.

When Halfpenny shaped cracks were generated, the Evans and Charles equation was used to calculate the fracture toughness [182]:

$$K_{1c} = 0.0824 \frac{P}{C^{1.5}} \tag{2.8}$$

Where; P: applied load (N); C: crack length (m).

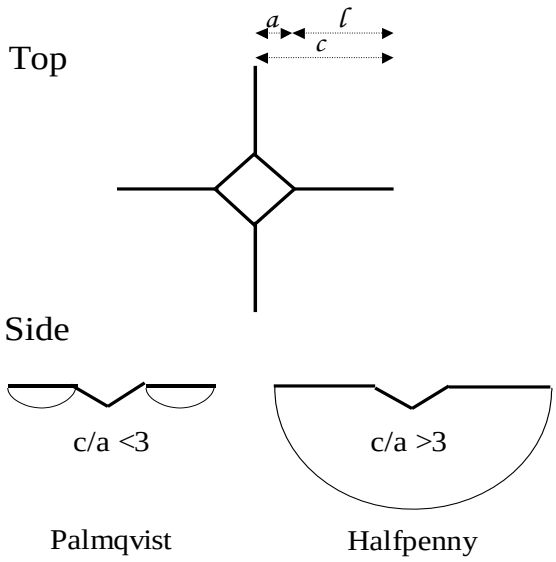


**Figure 2.1.** The top and side representation of the Palmqvist and Halfpenny shape cracks generated by Vickers micro-hardness indentation [183].

If Palmqvist shape crack was observed, Palmqvist equation was used for the calculations [184]:

$$K_{1c} = 0.035 \left(\frac{H^{0.6} E^{0.4}}{\phi^{0.6}}\right)\left(\frac{a}{(c-a)^{0.5}}\right) \tag{2.9}$$

Where:

H: Hardness; E: Young's Modulus; $\phi$: the coefficient related to the material constraint ($\phi \cong 3$).

#### 2.2.2.3. Biological Characterizations

Biological characterizations were done for the selected compositions which gave the best results in terms of microstructural and mechanical properties. From Group 3 2 Zn 1 F, 2 Zn 2.5 F and 2 Zn 5 F compositions were used. In addition to group 3, HA and 2 Zn were also characterized to investigate the effects of incorporated ions on cell proliferation. Saos-2 cell line was used for in vitro cell culture experiments. In terms of biological characterization, Alamar Blue™ dye reduction assay was used to study cell proliferation. Alkaline phosphatase activity measurement (ALP), an early bone differentiation marker, was conducted to determine the effects of composition and incorporated ions on the osteogenic differentiation of these cells on discs. Cell morphology on discs was studied by SEM at days 3 and 14.

##### 2.2.2.3.1. Alamar Blue™ Assay

4 samples for each group were used for Alamar Blue assay.$1x10^5$ number of cells were seeded on each disc. Disks were placed separately to wells of 24 well plates. Cells were incubated at 37ºC in an carbon dioxide incubator (Shel Lab, USA). Differentiation medium (90% high glucose DMEM without phenol red and 10% FBS supplemented with 0.47 mM ascorbic acid, 7.96 mM β-glycerolphosphate and 0.8 μM dexamethasone) was used as culture medium. The viability assay was conducted at days 3, 7 and 15. Culture medium was refreshed every three days.

After decanting culture medium, the cells were washed with phosphate buffered saline (PBS) once and Alamar Blue™ solution (10% Alamar Blue™ reagent in DMEM without phenol red) was added. After 4h of incubation, the medium in each well was collected and fluorescence was read (excitation at 525 nm and emission at 580 nm) in a fluorimeter (Modulu 9200, Turner Biosystem, USA). After the media were collected, cells were washed with PBS once and differentiation medium was added for further culturing.

### 2.2.2.3.2. Alkaline Phosphatase Activity Assay

For ALP activiy measurements, $5x10^4$ cells/disk were seeded on discs and the discs were incubated in osteogenic differentiation medium for 15 days. At days 7 and 15, the cell lysates were obtained by bursting cells with freeze and thaw cycles in 600 µl of PBS containing 0.1 % Triton X-100, 0.1 % v/w sodium azide and 1 % protease inhibitor. The plate was kept on ice for 30 minutes and then thawed. 20 µl lysate and 100 µl p-nitrophenylphosphate substrate solution were mixed. The mixture was incubated at 37°C for 30 minutes. Then, the absorbance at 405 nm was read by microplate spectrophotometer (µQuant MQX200, Biotek, USA). The amount of p-nitrophenol produced was determined using the calibration curve constructed with known concentrations of p-nitrophenol.

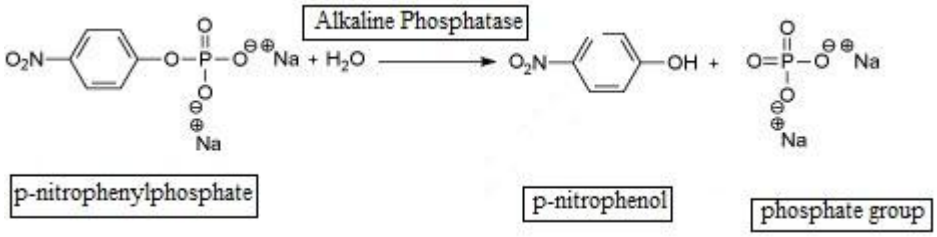


**Figure 2.2.** The conversion reaction of p-nitrophenylphosphate to p-nitrophenol by alkaline phosphatase enzyme.

BCA assay was done to determine the total protein amount in the lysates for the normalization of Alkaline Phosphatase Activity. Shortly, 1 ml $Cu_2SO_4$ solution (2 g cupric sulfate in 50 ml water) was mixed with 50 ml bicinchoninic acid solution to prepare the working reagent solution. 1 ml of the working solution and 50 µl cell lysate were incubated at 37 °C for 30 min. The absorbances of the samples were measured at 562 nm by microplate spectrophotometer (µQuant MQX200, Biotek, USA). The total protein amount was determined using the calibration curve constructed with known concentrations of bovine serum albumin (BSA) (0- 1.2 mg/ml).

#### 2.2.2.3.3. Scanning Electron Microscopy (SEM)

Cell morphologies were observed by SEM. 2 samples from each composition were prepared for SEM analysis. $1x10^5$ cells were seeded on discs and cultured in differentiation culture medium for 1 and 15 days. The cells were fixed with 2.5% gluteraldehyde in PBS solution. After 2h of fixation, the discs were rinsed with cacodylate buffer with (0.155 M, pH 4.7) for 1 minute. Then, the samples were rinsed with increasing concentrations of ethanol for 5 min (70%, 80%, 90% and 100%) .To increase the conductivity in SEM application, the disc samples were immersed in hexamethyldisilazane solution for 20 minutes. After the solution was pulled out and disks were kept at +4 °C until analysis. For further increase in conductivity, the discs were coated with lead by precision etching coating system (PECS) (Gatan 682, USA).

#### 2.2.2.3.4. Dissolution Test

Four discs from each sample were prepared and sintered at 1100°C for 1 h. Discs were then immersed in simulated body fluid (SBF) prepared as described in Table 2.2. All of the samples from each composition were placed separately in 15 ml polypropylene tubes. 10 ml of SBF was poured in each tube. Two of the samples from each composition were placed in a waterbath (Nuve, Turkey) set at 37°C and 60 rpm. The other two were placed in a incubator (Leec, United Kingdom) set at 37°C.

Dissolution of the samples with time was investigated by two different methods. One was measuring pH and the other was SEM observations for apatite formation on discs.

**Table 2.2.** Chemical composition of SBF solution and the sequence of mixing [183].

| Order of addition | Reagent | Amount (g/l) |
|---|---|---|
| 1 | NaCl | 6.721 |
| 2 | $NaHCO_3$ | 2.268 |
| 3 | KCl | 0.224 |
| 4 | $K_2HPO_4$ | 0.174 |
| 5 | $MgCl_2 \cdot 6H_2O$ | 0.305 |
| 6 | $CaCl_2 \cdot 2H_2O$ | 0.368 |
| 7 | $MgSO_4 \cdot 7H_2O$ | 0.123 |
| 8 | $Tris((CH_2OH)_3CNH_2)$ | 6.059 |
| 9 | 1 M HCl | 30 ml |

#### 2.2.2.3.4.1. pH Measurements

pH of the samples were measured by using a pHmeter, (Thermo, USA) at days 3, 7 and 15. pH of SBF solution without a disc was measured as a control. Change in pH at different incubation periods for each sample (either in waterbath or in incubator) was determined by subtracting the pH of the SBF in the control tube from the pH of the SBF in the sample's tube.

#### 2.2.2.3.4.2. SEM Observations for $Ca^{2+}$ Deposition

SEM observations were conducted after 7 and 15 days of incubations in SBF either in a water bath or incubator as described above. At the end of each incubation period, the samples were treated with acetone and 70% alcohol and left for drying at room temperature. The samples were coated with lead by precision etching coating system (PECS) (Gatan 682, USA) before SEM examinations.

# CHAPTER 3

# RESULTS AND DISCUSSION

## 3.1. Structural Analysis

### 3.1.1. Density of the Samples

The density of the samples after the sintering at 1100°C for 1h are represented in Table 3.1.

**Table 3.1.** Density of the samples after the sintering at 1100 °C for 1h.

| Group ID | Sample ID | Sintered Density ($g/cm^3$) | Relative Density (%) |
|---|---|---|---|
| **Group 1** | Pure | 2.902 | 91.9 |
| | 2 Zn | 3.056 | 96.8 |
| **Group 2** | 1 F | 2.728 | 86.5 |
| | 2.5 F | 2.736 | 86.7 |
| | 5 F | 3.024 | 95.8 |
| **Group 3** | 2 Zn 1 F | 3.048 | 96.6 |
| | 2 Zn 2.5 F | 3.052 | 96.7 |
| | 2 Zn 5 F | 3.123 | 99.0 |
| **Group 4** | 1 Cl | 2.985 | 94.6 |
| | 2.5 Cl | 3.091 | 97.9 |
| | 5 Cl | 2.974 | 94.2 |
| **Group 5** | 2 Zn 1 Cl | 2.968 | 94.1 |
| | 2 Zn 2.5 Cl | 3.044 | 96.5 |
| | 2 Zn 5 Cl | 2.894 | 91.7 |

In this study, the density of 2% $Zn^{2+}$ doped sample was found as 3.056 $g/cm^3$, whereas the density of pure HA was found as 2.902 $g/cm^3$. Ergun et al. synthesized 2% by mole $Zn^{2+}$ added HA by precipitation method and sintered the samples at

1100°C for 1h [137]. They measured the density by Archimedes method and found the value 3.160 g/cm$^3$ whereas the theoretical density was found as 3.238 g/cm$^3$ [137]. Moreover, pure HA was synthesized by the same method and the experimental density was found as 3.125 g/cm$^3$ [137].

When $Zn^{2+}$ effect to density is investigated, it can be said that $Zn^{2+}$ addition increased the density of pure HA. The density results of the current study was consistent with other studies.

There were other studies which combined ZnO with TCP. Xue et al. studied TCP doped with $Zn^{2+}$ ang $Mg^{2+}$ ions [185]. According to their results, after sintering at 1100°C, $Zn^{2+}$ addition increased relative density of the TCP up to 83.9% whereas the undoped sample had the relative density of 74.7% of the theoretical density [185]. Moreover, co-doping of $Mg^{2+}$ and $Zn^{2+}$ into TCP increased the relative density up to 81.5% although it was observed that $Mg^{2+}$ addition did not have any effect on density of TCP [185]. Therefore, the reason of this increase can be interpreted as $Zn^{2+}$ addition effect. In this study, the reason of the increase in density is explained as inhibitory effect of $Zn^{2+}$ dopants on phase transformation [185]. $Zn^{2+}$ dopants prevented β-TCP to transform into α-TCP which are more soluble and less stable phases, respectively. However, it was also stated that this inhibitory effect was only valid when the amount of $Zn^{2+}$ content was higher than that is used in current study [185].

In another study, TCP powder was mixed with ZnO powder to obtain $Zn^{2+}$ doped TCP [186]. After sintering the samples at 1250°C for 6h, the results showed that ZnO addition resulted in small improvement in densification of TCP [186]. Moreover, 2.5% ZnO doped sample gave smaller density values than 1% ZnO doped sample [186]. Bandyopadhyay et al. also studied HA doped with ZnO by mixing the powders of these two compounds [187]. After sintering at 1250°C, it was found that ZnO addition increased the density of the HA with a maximum of 92.4% relative density [187]. As the amount of ZnO increased in the samples, density of the samples increased also. Moreover, it was found that effect of ZnO on the density was more significant in HA than in TCP [187].

Effect of ZnO addition on HA synthesized by sol-gel technique and sintered at 1250°C and 1300°C for 6h was investigated by Kalita et al. [155]. Samples sintered at 1300°C gave higher density values than the samples sintered at 1250°C [155]. Moreover, ZnO addition showed an improvement in density of sintered pure HA. Especially the samples doped with 1 wt.% ZnO gave the highest density results [155]. However, as the amount of doping increased up to 2.5 wt.% and 4 wt.%, density of the samples decreased [155].

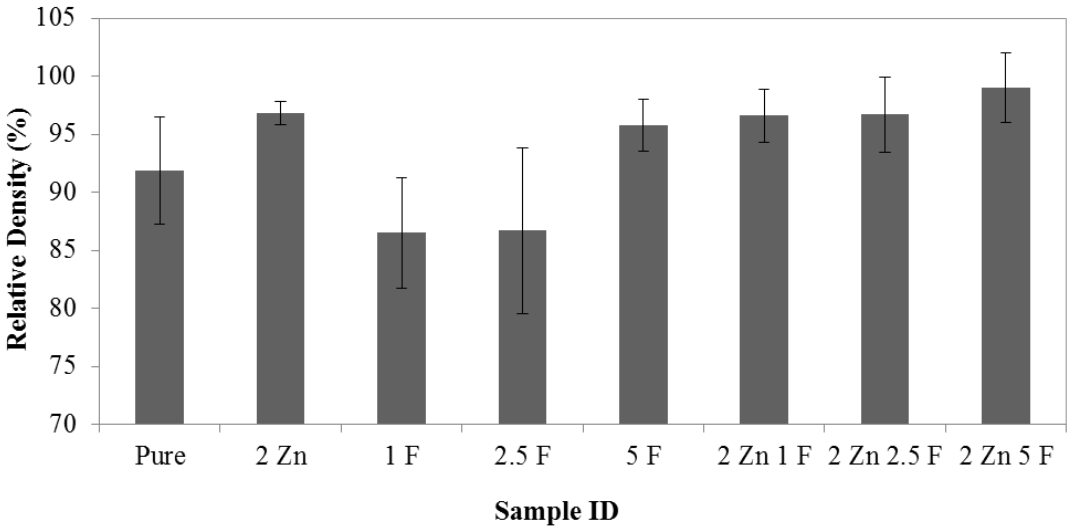


**Figure 3.1.** The effect of $Zn^{2+}$ and $F^-$ ions on relative density of the samples after the sintering at 1100°C for 1h.

When F group is investigated, it can be said that $F^-$ ion addition with an amount of 1 mole% and 2.5 mole% decreases the density of pure HA (Figure 3.1). A slight change in the densities can be seen between 1 F and 2.5 F whereas the density of 5 F increases dramatically. In a study, $Y^{3+}$ and $F^-$ ions were added to HA by precipitation method and sintered at 1100°C for 1h [188]. According to this study, $F^-$ addition decreased the density values of HA [188]. Moreover, as the $F^-$ amount increased in HA, the density values decreased [188].

In another study, $Mg^{2+}$ and $F^-$ ions were doped into HA with the same method and sintered at 1100°C for 1h [147]. In this study, it was investigated that, $Mg^{2+}$ ion

decreases the density of HA [147]. Moreover, when different percentages of $Mg^{2+}$ and 2.5% by mole $F^-$ were added together, the densities of the samples increased and higher values than density of pure HA were obtained [147]. However, as the amount of F in the samples increased, densities started to decrease [147].

Thermal stability of HA increased with the increase in the $F^-$ content [189]. However, when the $F^-$ content increased up to 57 mole% of $OH^-$ ions, porous structures were obtained at all sintering temperatures which resulted in decrease in the density of the samples [189]. In another study, $F^-$ was substituted into the HA with 50 mol.% [190]. The samples were synthesized by precipitation method and sintered at 1250°C for 1h. According to the results, 3.07 $g/cm^3$ of density was obtained for pure HA [190]. This value was 97% of the theoretical density (3.16 $g/cm^3$). For fluoridated HA, density was found as 3.13 $g/cm^3$ which is the 100% of the theoretical density [190]. α-TCP phase was also seen in pure HA at sintering temperature of 1250°C.

It is also investigated that as the $F^-$ content increased, the sinterability of the samples decreased. Moreover, $F^-$ content was increased between about 20 and 80 mol.%, the sintered density and some mechanical properties such as hardness, Young's Modulus and brittleness of HA decreased at a constant sintering temperature [191, 192]. As the sintering temperature increased, other phases different than HA appeared. However, fluoridated samples had one phase which is HA [190]. This means that $F^-$ ion increases the stability of HA. Increased stability results in decrease in dissolution rate and increase in density. The bond between $F^-$ and $OH^-$ also decreased the rate of diffusion which increased the density [188]. From the results of the former studies, it can be concluded that small additions of $F^-$ ion into HA structure increased the density due to increase in stability and decrease in dissolution rate. However, when the amount of $F^-$ ion increased up to 20 mol.% and above porosity appeared which decreased the density of the samples.

Moreover, it can be easily seen that, $Zn^{2+}$ addition significantly increases the density of the $F^-$ doped samples as expected. $Zn^{2+}$ and $F^-$ doped samples show the same trend as $F^-$ doped samples in terms of the amount of doped $F^-$ ions. When the

results were compared with that of pure HA, only the density of 1 F and 2.5 F gave smaller values than that of pure HA.

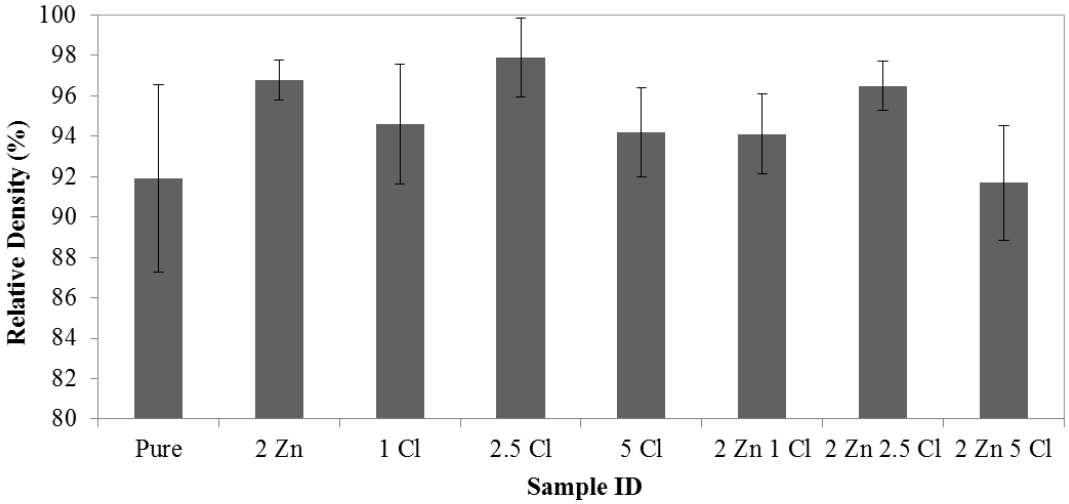


**Figure 3.2.** The effect of $Zn^{2+}$ and $Cl^-$ ions on relative density of the samples after the sintering at 1100 °C for 1h.

When $Cl^-$ amount became 2.5 mol.%, the density continued to increase. However, 5 mol.% addition of $Cl^-$ ion decreased the density under the density value of 1 mol.% $Cl^-$ doped HA. Although $Zn^{2+}$ incorporation and $Cl^-$ incorporation increased the density of pure HA seperately, when these two ions added together to the structure of HA, the density values were supressed. Moreover, in $Zn^{2+}$ and $Cl^-$ co-doped samples, the density increased up to that of 2.5 mol.% doping of $Cl^-$. However, 5 mol.% doping of $Cl^-$ resulted in decrease in density. The smallest density was achieved in 2 Zn 5 Cl (Figure 3.2).

The densities of pure HA and chlorapatite were measured as 2.83 and 2.23 $g/cm^3$, respectively [193]. From these results, it can be said that the densities of $Cl^-$ doped HA samples should be between these values. Moreover, as the amount of $Cl^-$ increased, the density of the samples decreased [193]. However, the densities of $Cl^-$ doped samples obtained in this study was higher than that of pure HA. This was due to the fact that the precursor used in this study was $CaCl_2 \cdot 2H_2O$. This calcium included precursor provided more $Ca^{2+}$ ions to the system which may result in more

dense materials. However, as the amount of $Cl^-$ addition increased, the density values decreased. The decrease may be stem from the fact that 5 mol.% addition of $Cl^-$ may deform the structure of HA, which may result in an increase in porosity. $Zn^{2+}$ and $Cl^-$ incorporation together resulted in lower densities than that of $Zn^{2+}$ or $Cl^-$ doped samples. It was expected that the densities increased further by $Zn^{2+}$ addition. However, these two ions incorporation may contribute to some deformations in the structure and result in porosity. From these results, as it was expected, the lowest density among $Cl^-$ doped samples corresponded to the sample 2 Zn 5 Cl.

### 3.1.2. X-Ray Diffraction Analysis

XRD data is shown in Figures 3.3-3.8. When compared to JCPDS#: 9-432 data for Standard HA, it can be easily observed that all samples possess the XRD pattern of HA.

No other phases such as α-TCP and β-TCP are observed. In some of the samples, small amount of CaO phase is detected. Rietvelt analysis was applied to the samples by using General Structure Analysis System (GSAS) computer program. CaO and HA phases found in the structure of the samples are listed in Table 3.2.

According to the Figures 3.3-3.8, there is no significant broad peaks which are the indicator of poor crystallinity. The fraction of crystalline phases were calculated by using intensity of the peaks which corresponded to (3 0 0) and (1 1 2) system. The results are presented in Table 3.2. According to the results, $Zn^{2+}$ addition decreased the crystallinity, whereas $F^-$ and $Cl^-$ additions increased it. However, as the $F^-$ and $Cl^-$ amount increased, crystallinity decreased. Addition of $Zn^{2+}$ ion dropped the Ca/P ratio of HA from 1.67 to 1.63. Therefore, the lack of $Ca^{2+}$ ions in the structure decreased the crystallinity of the HA [194]. The increase in crystallinity with addition of $F^-$ stemmed from the increase in the stability of the pure HA with addition of $F^-$. However, when the addition amount increased, the fraction of crystallites decreased due to the deformations of the HA structure.

However, all values are higher than that of pure HA except 5 F. It has the same value with pure HA. Co-doping of $Zn^{2+}$ and $F^-$ ions resulted in increase in fraction of crystallite when compared with $F^-$ doped samples surprisingly.

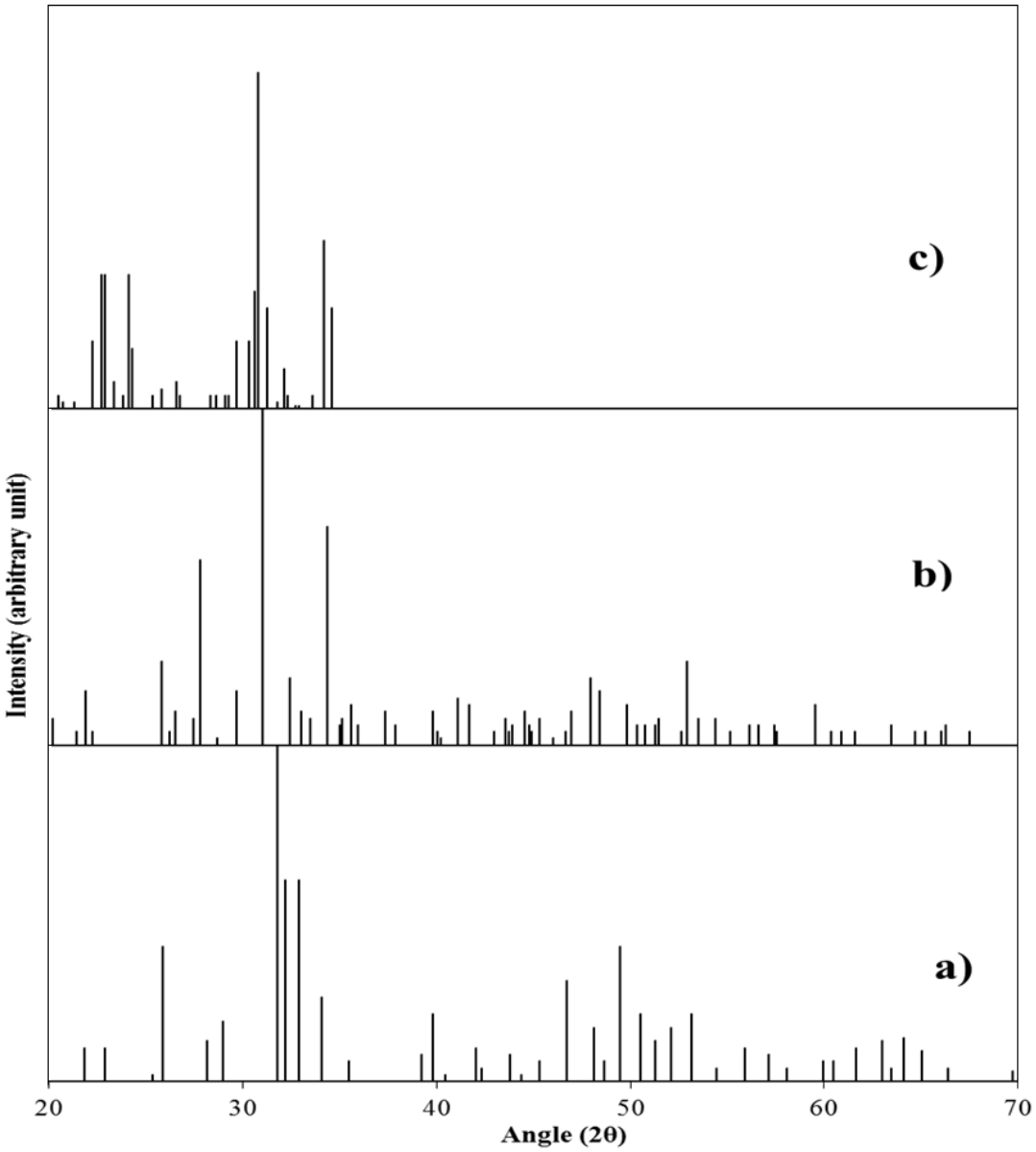


**Figure 3.3.** XRD patterns of a) Standard HA (JCPDS#: 9-432); b) Standard α-TCP (JCPDS#: 9-169); c) Standard β–TCP (JCPDS#: 9-348).

The increase in fraction of crystallite in $Cl^-$ doped samples was due to the fact that the additional $Ca^{2+}$ from the precursor $CaCl_2 \cdot 2H_2O$. However, as the $Cl^-$

amount increased, the fraction of crystallite phase decreased. This can be explained by the deformation in the HA structure by increasing the amount of $Cl^-$ in the sample. Surprisingly, $Zn^{2+}$ and $Cl^-$ doped samples gave higher crystallinity values than $Zn^{2+}$ or $Cl^-$ doped samples.

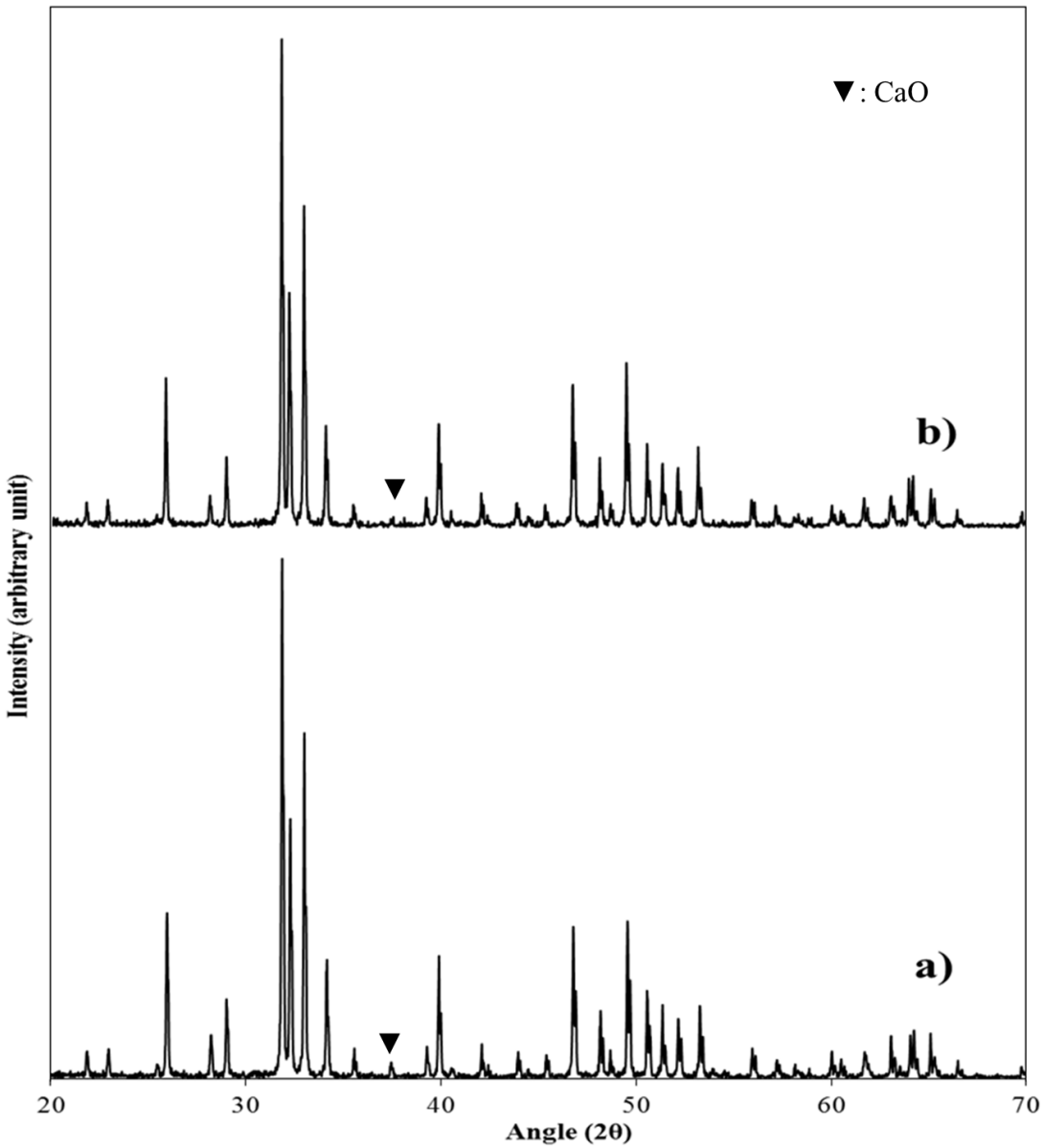


**Figure 3.4.** XRD patterns of the samples sintered at 1100 °C for 1h: a) pure HA; b) 2 Zn.

Co-doping of these two ions increased the crystallinity further. 2 Zn 2.5 Cl sample had the highest crystallinity.

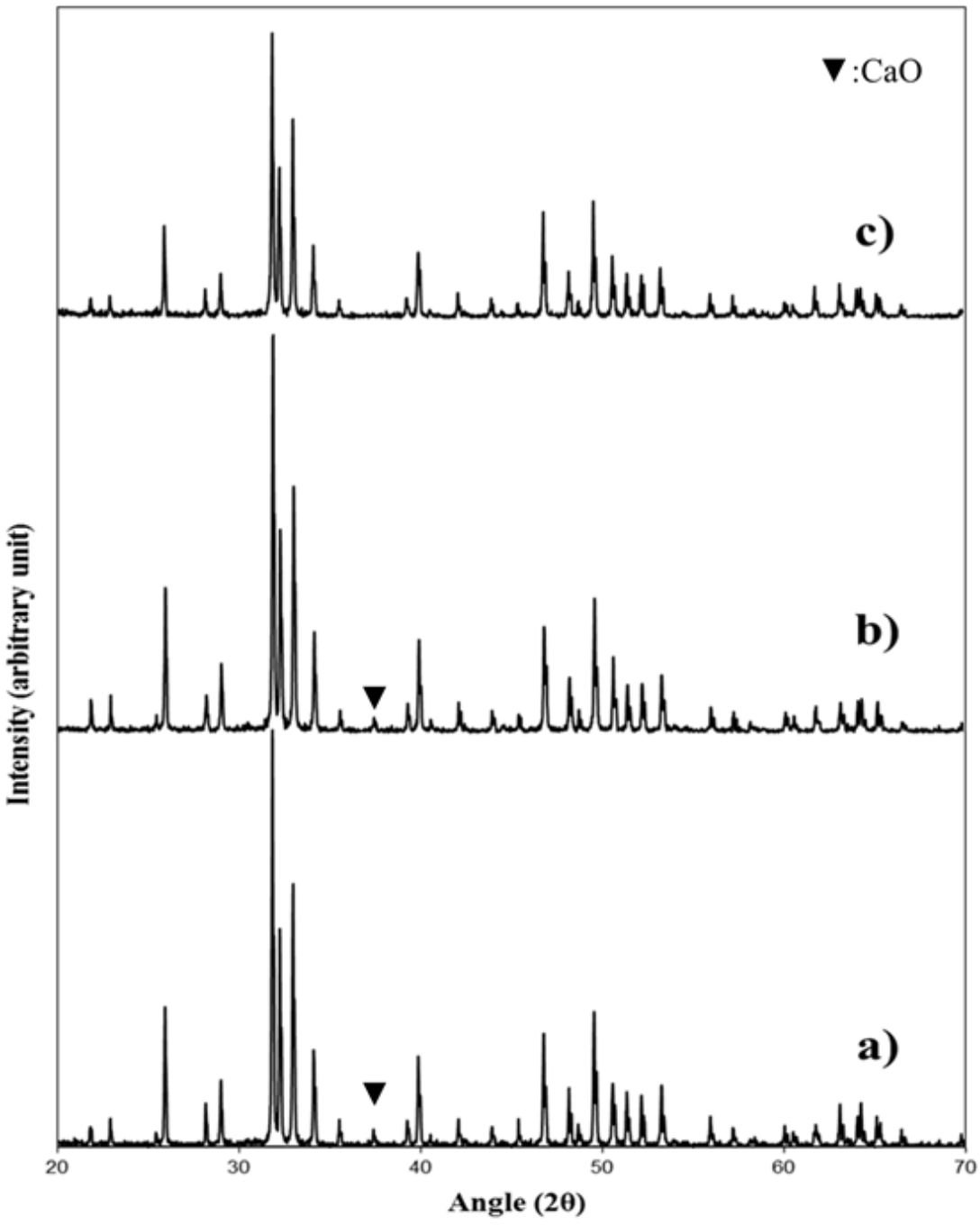


**Figure 3.5.** XRD patterns of the samples sintered at 1100°C for 1h: a) 1 F; b) 2.5 F; c) 5 F.

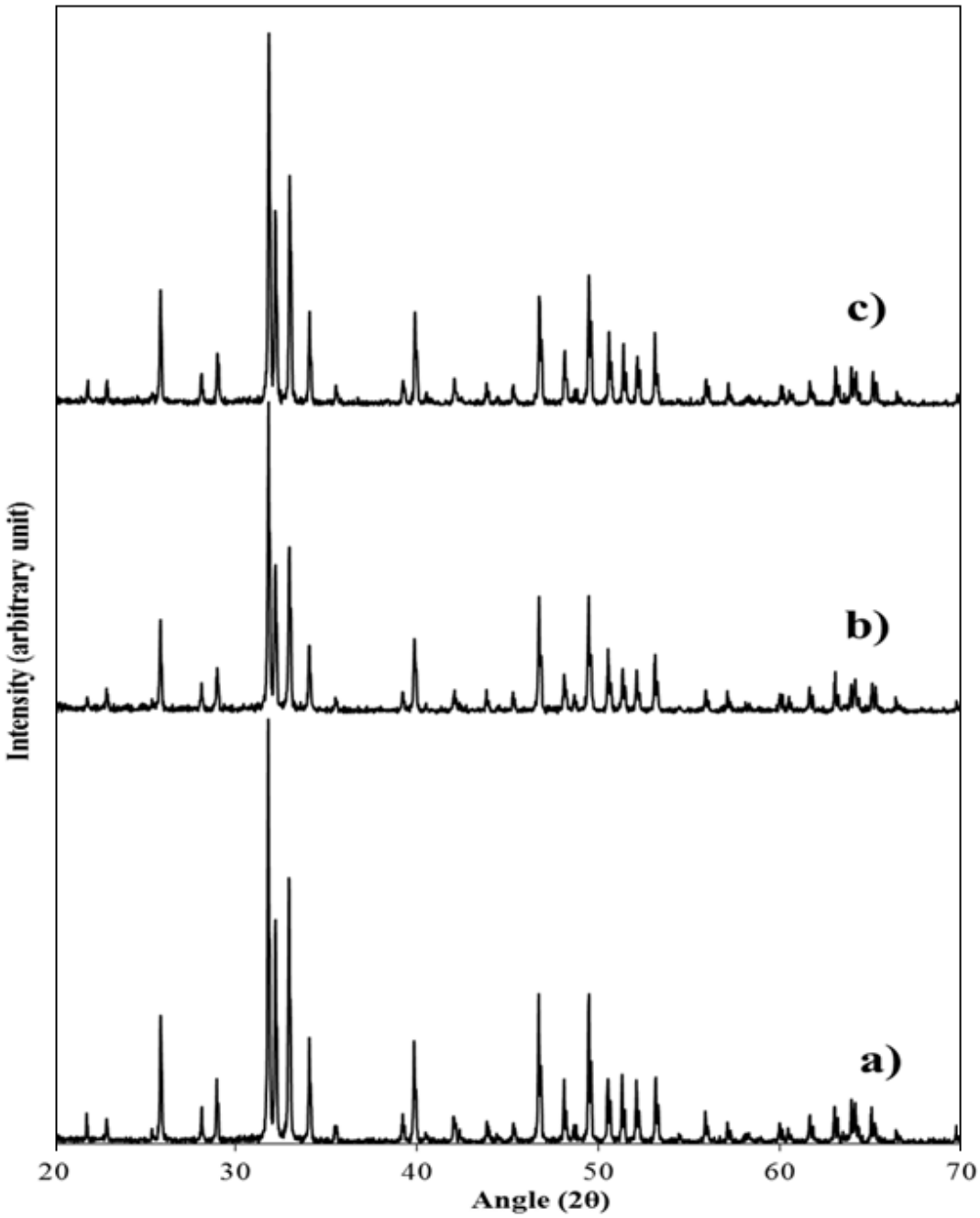


**Figure 3.6.** XRD patterns of the samples sintered at 1100°C for 1h: a) 2 Zn 1 F; b) 2 Zn 2.5 F; c) 2 Zn 5 F.

CaO phase is formed by the incorporation of $Zn^{2+}$ ions into HA hexagonal structure [195]. When $Zn^{2+}$ ion replaces $Ca^{2+}$ ion in HA, the $Ca^{2+}$ ions detached from HA structure to form CaO. Therefore, it may be the reason of CaO presence in

the samples with $Zn^{2+}$ ions. The phase fraction of HA in $Zn^{2+}$ doped HA was higher than that of pure HA.

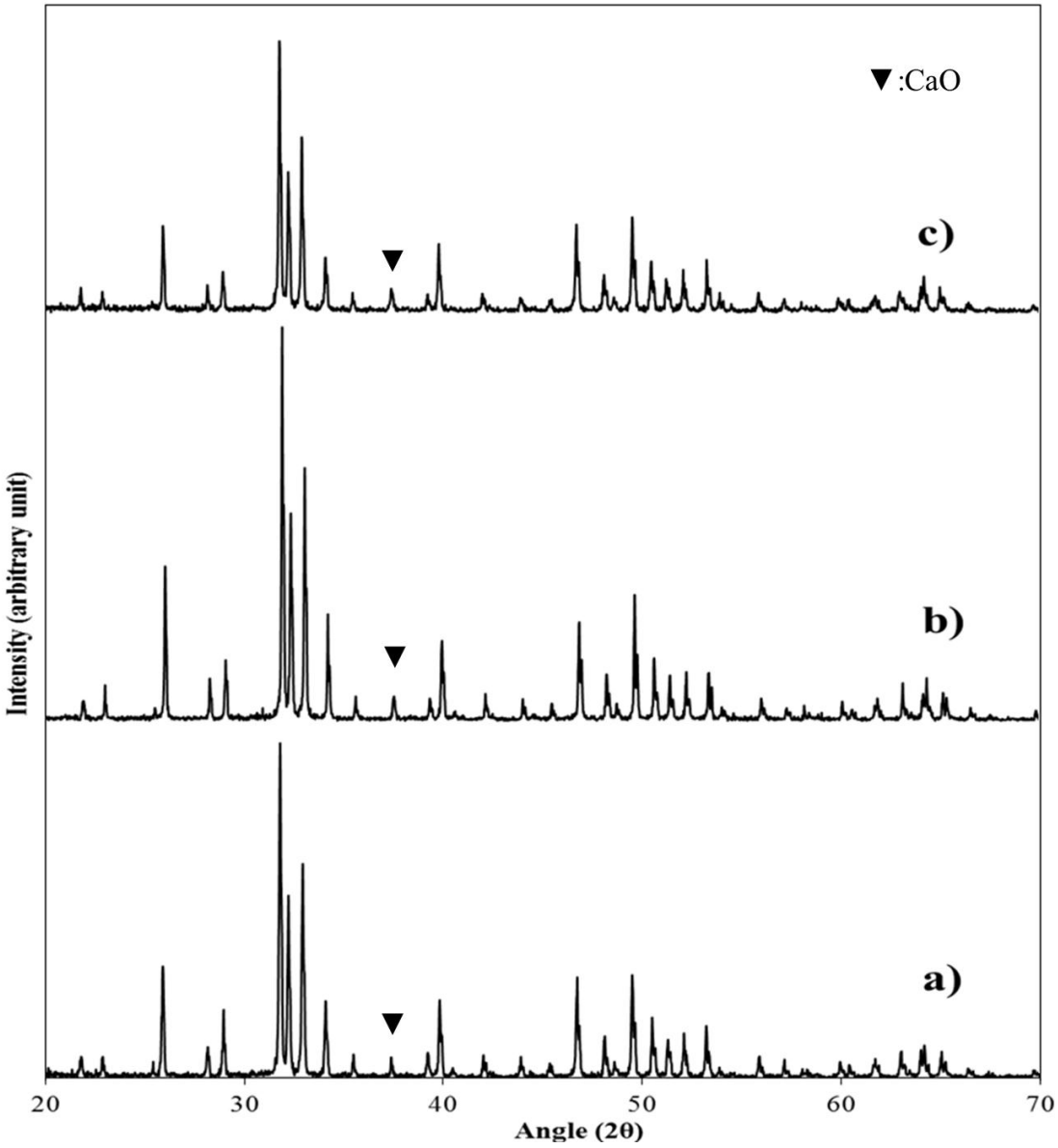


**Figure 3.7.** XRD patterns of the samples sintered at 1100°C for 1h: a) 1 Cl; b) 2.5 Cl ; c) 5 Cl.

When the phase fractions of fluoridated samples was investigated, it can be said that HA phase fraction increased. It is due to the fact that $F^-$ makes the HA structure

more stable. Therefore, presence of other phases were inhibited. Moreover, $Zn^{2+}$ and $F^-$ co-doping gave the highest fraction of HA phase which was the indicator of increased stability with co-doping of these two ions.

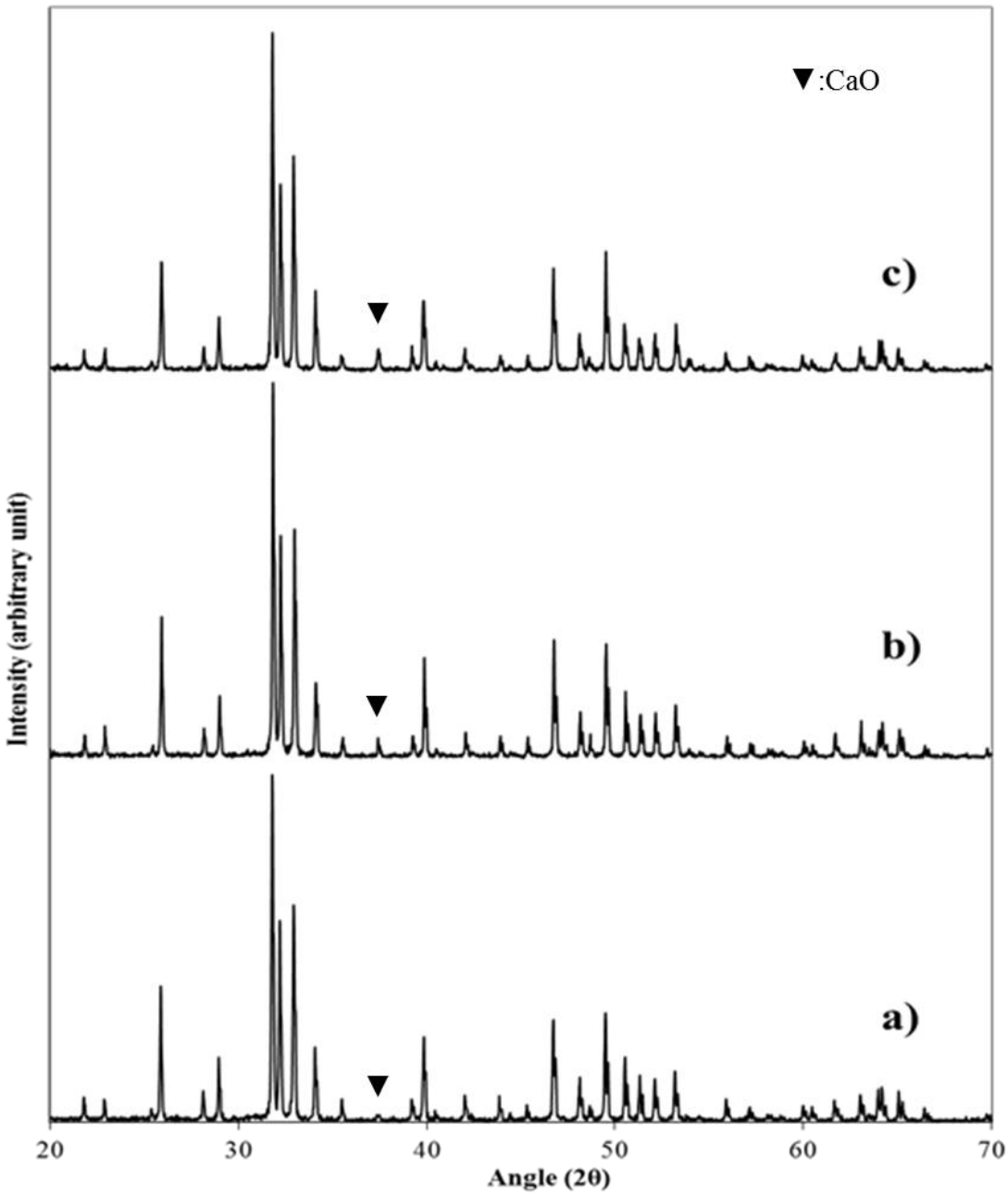


**Figure 3.8.** XRD patterns of the samples sintered at 1100°C for 1h: a) 2 Zn 1 Cl; b) 2 Zn 2.5 Cl; c) 2 Zn 5 Cl.

$Cl^-$ ion doping resulted in increase in CaO phase. This is due to the fact that the precursor used for $Cl^-$ contained samples is $CaCl_2 \cdot H_2O$. The $Ca^{2+}$ ions of the precursor may also cause the formation of CaO, although the amount of $Ca^{2+}$ ion is calculated before mixing the precursors. As the amount of $Cl^-$ in the samples increased, the phase fraction of CaO increased as expected. In $Zn^{2+}$ and $Cl^-$ co-doped samples a decrease in CaO phase was detected when compared to $Cl^-$ doped samples. This is due to the stability effect of $Zn^{2+}$ doping on HA structure.

**Table 3.2.** Weight fractions of HA and CaO phase and fraction of crystalline phase in samples.

| Group Name | Compound Name | Weight fraction of HA phase | Weight fraction of CaO phase | Fraction of crystalline phase ($X_c$) |
|---|---|---|---|---|
| Group 1 | Pure | 0.9934 | 0.0066 | 0.75 |
| | 2 Zn | 0.9970 | 0.0030 | 0.68 |
| Group 2 | 1 F | 0.9871 | 0.0129 | 0.83 |
| | 2.5 F | 0.9912 | 0.0088 | 0.82 |
| | 5 F | 0.9962 | 0.0038 | 0.75 |
| Group 3 | 2 Zn 1 F | 1.0000 | 0.0000 | 0.84 |
| | 2 Zn 2.5 F | 1.0000 | 0.0000 | 0.89 |
| | 2 Zn 5 F | 1.0000 | 0.0000 | 0.85 |
| Group 4 | 1 Cl | 0.9876 | 0.0125 | 0.85 |
| | 2.5 Cl | 0.9775 | 0.0225 | 0.82 |
| | 5 Cl | 0.9661 | 0.0339 | 0.80 |
| Group 5 | 2 Zn 1 Cl | 0.9950 | 0.0050 | 0.93 |
| | 2 Zn 2.5 Cl | 0.9869 | 0.0131 | 0.97 |
| | 2 Zn 5 Cl | 0.9731 | 0.0270 | 0.87 |

### 3.1.2.1. Lattice Parameters of Pure and Doped HA

Hexagonal lattice parameters and unit cell volumes of the materials were investigated using Rietvelt analysis by GSAS.

**Table 3.3.** Hexagonal lattice parameters, unit cell volumes of all samples.

| Group Name | Compound Name | a (Å) | c (Å) | Δa (Å) | Δc (Å) | V (Å$^3$) | ΔV (Å$^3$) |
|---|---|---|---|---|---|---|---|
| Group 1 | Pure | 9.4349 | 6.8926 | 0.0000 | 0.0000 | 1588.5 | 0.000 |
| | 2 Zn | 9.4314 | 6.9006 | -0.0035 | 0.0080 | 1589.2 | 0.669 |
| Group 2 | 1 F | 9.4341 | 6.8938 | -0.0008 | 0.0012 | 1588.5 | 0.016 |
| | 2.5 F | 9.4333 | 6.8958 | -0.0016 | 0.0032 | 1588.7 | 0.193 |
| | 5 F | 9.4311 | 6.8985 | -0.0038 | 0.0059 | 1588.6 | 0.083 |
| Group 3 | 2 Zn 1 F | 9.4161 | 6.8875 | -0.0188 | -0.0051 | 1581.0 | -7.489 |
| | 2 Zn 2.5 F | 9.4054 | 6.8882 | -0.0295 | -0.0044 | 1577.6 | -10.892 |
| | 2 Zn 5 F | 9.4029 | 6.8910 | -0.0320 | -0.0016 | 1577.4 | -11.119 |
| Group 4 | 1 Cl | 9.4215 | 6.8808 | -0.0133 | -0.0118 | 1581.3 | -7.193 |
| | 2.5 Cl | 9.4370 | 6.8895 | 0.0021 | -0.0031 | 1588.5 | 0.006 |
| | 5 Cl | 9.4242 | 6.8711 | -0.0107 | -0.0215 | 1579.9 | -8.552 |
| Group 5 | 2 Zn 1 Cl | 9.4187 | 6.8871 | -0.0162 | -0.0055 | 1581.8 | -6.729 |
| | 2 Zn 2.5 Cl | 9.4327 | 6.8974 | -0.0022 | 0.0048 | 1588.9 | 0.388 |
| | 2 Zn 5 Cl | 9.4188 | 6.8772 | -0.0161 | -0.0154 | 1579.6 | -8.950 |

According to the results, $Zn^{2+}$ addition increased the lattice parameter “c”, whereas decreased the lattice parameter “a” with a little amount. However, the volume increased due to increase in parameter “c”. In the crystal structure of HA, $Zn^{2+}$ can be placed into three positions. These are Ca(I), Ca(II) and P positions [196]. The ionic radius of these ions are 0.99 Å for $Ca^{2+}$, 0.31 Å for $P^{5-}$ and 0.74 Å for $Zn^{2+}$, respectively [197]. There are four Ca(I) atoms and six Ca(II) atoms in HA

structure. The Ca(I) atoms formed octahedral structure with their $O^{2-}$ atoms [187, 198]. On the other hand, Ca(II) atoms formed tetrahedral structure with $O^{2-}$ atoms [187, 198]. The tetrahedral structure requires less energy of formation. $P^{5-}$ ion also forms tetrahedral structure. However, the difference in ionic radius and charge $Zn^{2+}$ ion is more likely to replace $Ca^{2+}$ ions. Between Ca(I) and Ca(II), $Zn^{2+}$ ion prefers Ca(II) ion to replace due to less energy of formation because of its tetrahedral structure. $Zn^{2+}$ has smaller ionic radius than that of $Ca^{2+}$. Therefore, it was expected that $Zn^{2+}$ decreased the parameters "a", "c" and unit cell volume [137]. However, it was more likely to have a decrease in parameter "a" and unit cell volume and increase in the parameter "c" [196]. When the lattice parameters in this study were investigated, it can be said that there was no significant difference in parameter "a" after $Zn^{2+}$ addition. However, as expected, the parameter "c" increased. This difference was reflected as increase in unit cell volume which was an unexpected result. This stemmed from the fact that $Zn^{2+}$ ion can incorporate not only Ca(II) site but also Ca(I) site in the same structure. In this structure, most of $Zn^{2+}$ ions replaced Ca(II) site. Some of the ions may be replaced Ca(I) and P site also.

$F^-$ addition made very small changes in the crystal lattice of HA [199]. F-addition into HA decreased the parameter "a" and increased the parameter "c". Due to the fact that increase in parameter "c" was higher than increase in parameter "a", these changes resulted in very small increase in unit cell volumes when compared with pure HA. The changes in lattice parameters were also related with the amont of $F^-$ doping. As the amount of $F^-$ increased in the structure, the parameter "a" decreased and the parameter "c" increased. $F^-$ ions replaces $OH^-$ ion in the HA structure. The ionic radius of $F^-$ and $OH^-$ ion are 1.31 Å and 1.35 Å, respectively [200]. $F^-$ ion has higher electronegativity than that of $OH^-$. The decrease in parameter "a" stemmed from the low ionic radius and high electronegativity of $F^-$ ion [188]. The decrease in lattice parameter "a" was an expected result [139, 190, 198, 199]. Table 3.4 represents the positions of atoms along c-axis. According to the Table 3.4, $F^-$ ion positions are very close to the "O" atom position in $OH^-$ ion. Therefore, no change in c-axis was expected [130, 139, 190, 198]. However, in a

study a slight increase in direction c was detected [199]. This was due to the fact that 0.05 difference in z positions between "O" atom and "F" atom.

**Table 3.4.** z positions of the atoms of $OH^-$, $F^-$ and $Cl^-$ ions [130].

| Ion | Atoms | z |
|---|---|---|
| $OH^-$ | O | 0.2 or 0.3, 0.7 or 0.8 |
| | H | 0.06 or 0.44, 0.56 or 0.94 |
| $F^-$ | F | 0.25, 0.75 |
| $Cl^-$ | Cl | 0.0, 0.44 |

$F^-$ and $Zn^{2+}$ ions codoping decreased the parameter "a" significantly. This was due to the fact that $F^-$ and $Zn^{2+}$ ions had smaller ionic radius than $OH^-$ and $Ca^{2+}$ ions have [200]. The parameter "c" was smaller than pure HA in all $Zn^{2+}$ and $F^-$ co-doped samples. However, as the amount of $F^-$ increased the parameter "c" increased. This increase did not have an significant effect on hexagonal unit cell volumes. Hexagonal unit cell volumes of the samples decreased as the $F^-$ content in the $Zn^{2+}$ and $F^-$ co-doped samples increased.

$Cl^-$ addition decreased both the parameters "a" and "c". $Cl^-$ ion replaced $OH^-$ ion. The ionic radius of $Cl^-$ and $OH^-$ ions are 1.81 Å and 1.35 Å, respectively [200]. Due to the fact that $Cl^-$ ion is bigger than $OH^-$ ion, the unit cell volume expected to expand. However, the expansion only seen in the samples 2.5 mol.% $Cl^-$ added samples. Decrease in both parameters "a" and "c" were observed in 1 mol.% $Cl^-$ added samples. Further decrease were seen for 5 mol.% $Cl^-$ doped samples. According to Table 3.4, the z position of $Cl^-$ ion is highly different than O atom position. H and Cl atoms have the same positions (Table 3.4). Therefore, a deformation in the structure of HA was expected. This deformation resulted in increase in lattice parameters. Moreover, $Cl^-$ addition resulted in two different types of crystal structure; one is $P6_3/m$ hexagonal crystal structure and the other is $P2_1/b$ monoclinic structure [201]. The fluctuations in the lattice parameters stemmed

from occurrence of two different crystal structures in different amounts in $Cl^-$ doped samples.

When $Zn^{2+}$ and $Cl^-$ introduced to the system together, further decrease in "a", "c" and unit cell volume of the samples doped $Cl^-$ with 1 mol.% and 5 mol.% and increase in all parameters of 2.5 mol.% $Cl^-$ doped sample were observed. $Zn^{2+}$ ion addition decreased the hexagonal crystal lattice structure. Therefore, decrease in lattice parameters should be observed.

### 3.1.3. FTIR Analysis

FTIR studies were done for the observation of bands related to HA and also observation of bands related to $Zn^{2+}$, $F^-$ and $Cl^-$ ions to investigate whether HA structure was obtained or not and these three ions were incorporated to the HA structure or not.

**Table 3.5.** Assignments of FTIR absorption bands of pure HA after sintering at 1100°C for 1h in 4000-400 $cm^{-1}$ region [144, 193, 202-204].

| Peak No | Functional Groups | Vibration Mode | Wavenumber ($cm^{-1}$) |
|---|---|---|---|
| 1 | $(PO_4)^{3-}$ | $\nu_1$ | 960 |
| 2 | $(PO_4)^{3-}$ | $\nu_2$ | 473 |
| 3 | $(PO_4)^{3-}$ | $\nu_3$ | 1045, 1091 |
| 4 | $(PO_4)^{3-}$ | $\nu_4$ | 568, 601 |
| 5 | $OH^-$ | librational | 632 |
| 6 | $OH^-$ | stretching | 3571 |
| 7 | OH…Cl | | 3498 |
| 8 | OH…F | | 711, 3543 |
| 9 | Zn-O | stretching | 3403, 433 |

In Table 3.5, the locations of observed FTIR bands in pure HA and their assignments are summarized. All $(PO_4)^{3-}$ and $OH^-$ related bands specific for HA were observed in all samples nearly at the same wavenumbers.

**Table 3.6.** The band locations in FTIR spectra of the samples in the range of 3570-1045 $cm^{-1}$.

| Observed Wavenumbers ($cm^{-1}$) / Sample ID | 3571 | 3543 | 3495 | 3403 | 1091 | 1045 |
|---|---|---|---|---|---|---|
| Pure | 3571 | - | - | - | 1091 | 1045 |
| 2 Zn | 3570 | - | - | 3403 | 1091 | 1044 |
| 1 F | 3570 | 3543 | - | - | 1091 | 1046 |
| 2.5 F | 3569 | 3543 | - | - | 1092 | 1046 |
| 5 F | 3567 | 3542 | - | - | 1093 | 1047 |
| 2 Zn 1 F | 3570 | 3543 | - | 3404 | 1091 | 1045 |
| 2 Zn 2.5 F | 3569 | 3543 | - | 3402 | 1091 | 1045 |
| 2 Zn 5 F | 3567 | 3538 | - | 3400 | 1092 | 1046 |
| 1 Cl | 3571 | - | 3495 | - | 1091 | 1045 |
| 2.5 Cl | 3571 | - | 3496 | - | 1091 | 1045 |
| 5 Cl | 3571 | - | 3496 | - | 1090 | 1045 |
| 2 Zn 1 Cl | 3570 | - | 3498 | 3404 | 1091 | 1045 |
| 2 Zn 2.5 Cl | 3569 | - | 3496 | 3403 | 1090 | 1045 |
| 2 Zn 5 Cl | 3569 | - | 3496 | 3403 | 1091 | 1046 |

According to Table 3.6, The band observed at 3571 $cm^{-1}$ in pure HA spectra is assigned to the stretching vibration of the structural $OH^-$. By 2 mol.% $Zn^{2+}$ addition, the band shifted to 3570 $cm^{-1}$ [144, 190, 193, 203, 205]. Moreover, 1 mol.% addition of $F^-$ ion resulted in a shift to 3570 $cm^{-1}$. As the amount of $F^-$ increased in

the samples, the bands gradually shifted to the smaller wavenumbers (For 2.5 F, it became 3569 $cm^{-1}$ and for 5 F, it became 3567 $cm^{-1}$). $Zn^{2+}$ and $F^-$ doped samples followed the same trend with $F^-$ doped samples. The shifts in the absorptions are indicator of changes in structure, conformation and intermolecular interaction [206]. In the current study, the wavenumbers decreased with increasing $F^-$ amount in band at 3571 $cm^{-1}$. The shifts in the wavenumbers in band at 3571 $cm^{-1}$ stem from the increase in number of hydrogen bonds between $F^-$ and $H^+$ ions with $F^-$ addition. $Cl^-$ doping did not change the location of pure HA. However, $Zn^{2+}$ and $Cl^-$ co-doping resulted in a little shift to 3570 and 3569 $cm^{-1}$.

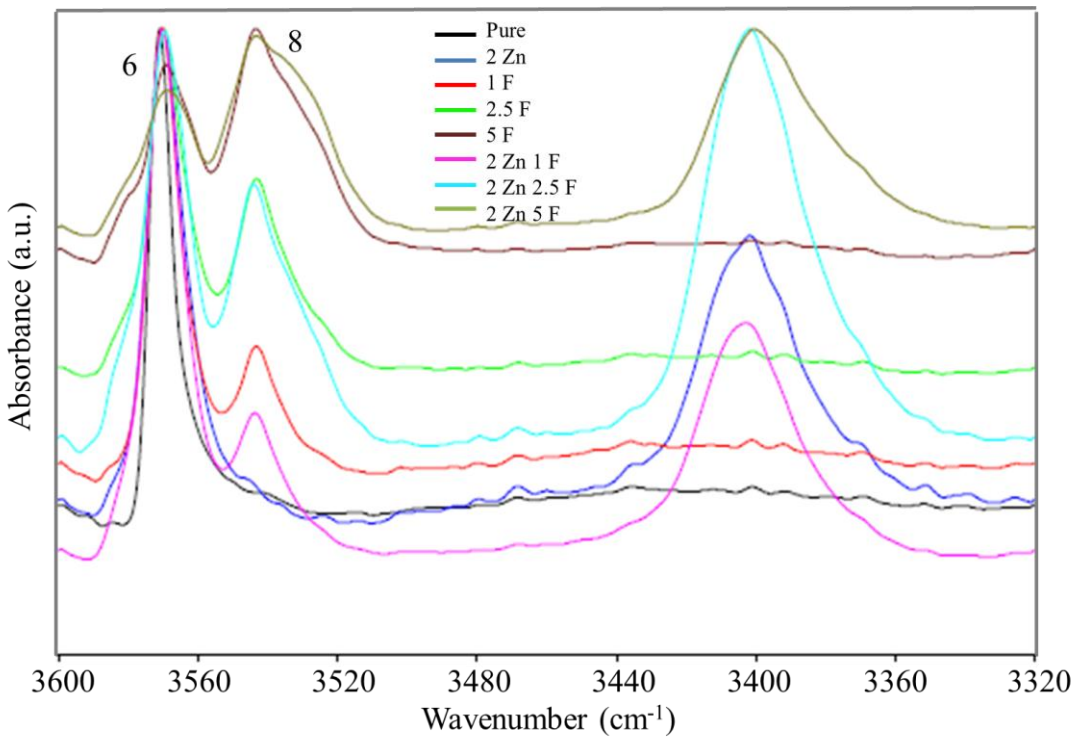


**Figure 3.9.** FTIR absorbance spectra of pure HA, $F^-$ and/or $Zn^{2+}$ doped samples in 3600-3320 $cm^{-1}$ region. (Normalization was done at peak 3575 $cm^{-1}$.)

Figure 3.9 shows the FTIR absorbance spectra for pure HA and $F^-$ and/or $Zn^{2+}$ doped samples in 3600-3320 $cm^{-1}$ region. In this range, the peaks at around 3571, 3543 and 3403 $cm^{-1}$ were observed. The intensity of the peaks at 3571 $cm^{-1}$

decreased with increasing $F^-$ amount in the samples [188]. This is due to the fact that $F^-$ ion replaces with $OH^-$ ion in the HA structure. As the $F^-$ amount in the samples increases, the concentration of $OH^-$ ion in the HA structure decreases due to the replacement with $F^-$ ion which results in decrease in intensity of the peaks at 3571 $cm^{-1}$ [207]. This is the indicator of successful incorporation of $F^-$ ion into the HA structure.

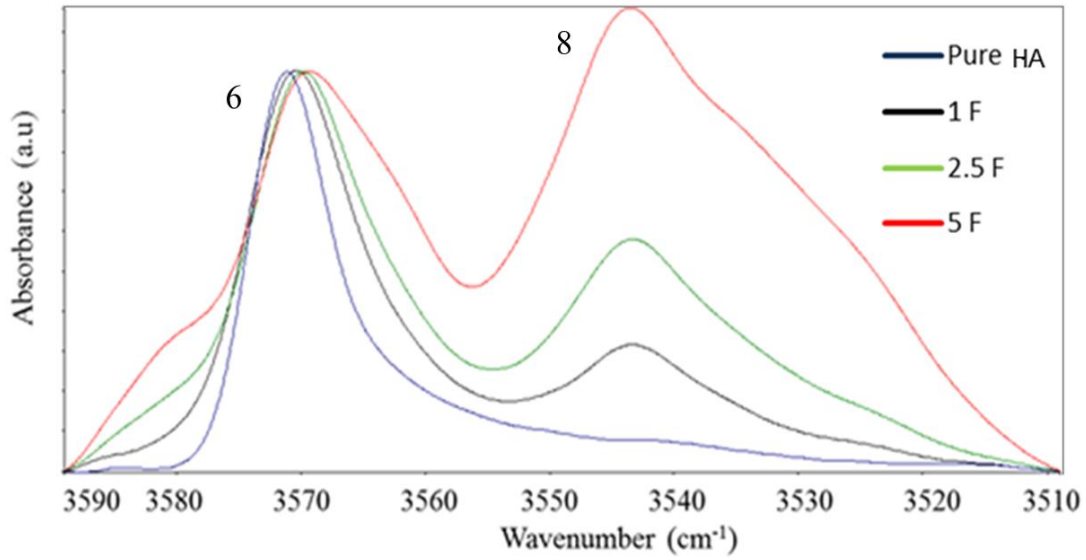


**Figure 3.10.** FTIR absorbance spectra of pure HA and $F^-$ doped samples in 3590-3510 $cm^{-1}$ region. (Normalization was done at peak 3575 $cm^{-1}$.)

The difference in the intensities can be seen more precisely in Figures 3.10 and 3.11. The differences in the intensities and the area under the bands are strongly related with the concentration of the functional groups [208, 209]. Therefore, the area under the the peak 3571 $cm^{-1}$ was also calculated for all samples and the results were represented in Figure 3.12. According to Figure 3.12, there is a statistical difference between pure HA and 2.5 F, pure HA and 5 F, 2.5 F and 5 F. Moreover, 2 Zn 5 F sample has significantly lower $OH^-$ band area at 3571 $cm^{-1}$ than that of the pure, 2 Zn 1 F and 2 Zn 2.5 F samples. This indicates that the concentration of $OH^-$ functional group decreased in the sample 2 Zn 5 F due to the replacement of $F^-$ group with $OH^-$ group [208, 209]. The changes in the area under the peak at 3571

$cm^{-1}$ suggest that $F^-$ ion addition with the amounts of 1 mol.%, 2.5 mol.% and 5 mol.% was succeeded.

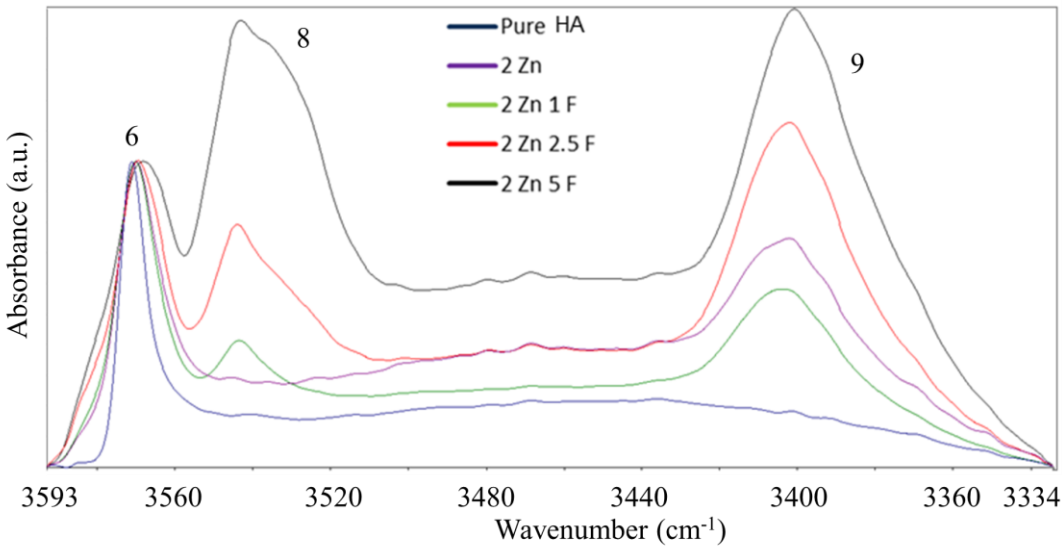


**Figure 3.11.** FTIR absorbance spectra of pure HA, $F^-$ and/or $Zn^{2+}$ doped samples in 3593-3334 $cm^{-1}$ region. (Normalization was done at peak 3573 $cm^{-1}$.)

Another important band in $F^-$ doped samples is at 3543 $cm^{-1}$. This band corresponds to the bond OH…F. Therefore, this band was seen only in $F^-$ doped samples. A small shift was seen in 5 mol.% $F^-$ doped HA ( at 3542 $cm^{-1}$). A relatively high amount of shift was observed for 2 Zn 5 F ( at 3538 $cm^{-1}$). The shifts to the lower wavenumbers with addition of $F^-$ ion is also related with increase in the number of hydrogen bonds between $F^-$ and $H^+$ ions [207, 208]. As the $F^-$ amount increased in the HA structure, the number of hydrogen bonds between $F^-$ and $H^+$ ion increased which resulted in a decrease in wavenumbers of the band at 3543 $cm^{-1}$ (Figure 3.10 and 3.11) [208, 209]. Moreover, in Figure 3.11, the samples without $F^-$ ion (pure HA and 2 Zn) do not have any bands at 3543 $cm^{-1}$ as expected. The band at 3543 $cm^{-1}$ is the evidence of the successful incorporation of $F^-$ ion into the HA structure.

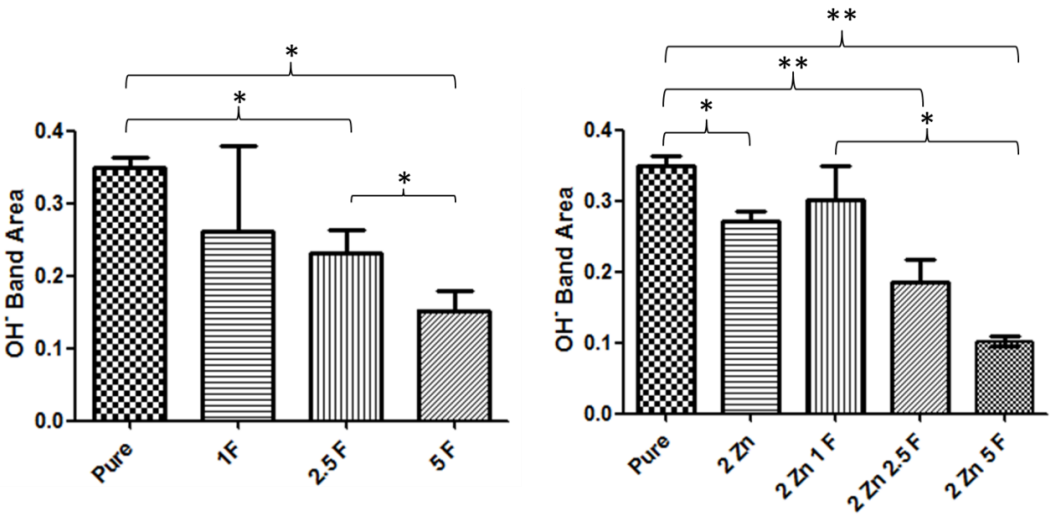


**Figure 3.12.** The $OH^-$ stretching band area at 3570 $cm^{-1}$ for pure HA and $Zn^{2+}$ and/or $F^-$ doped samples. (Paired student t- test was applied by using Minitab Statistical Software, USA: * denotes $p<0.05$ and ** denotes $p<0.01$.)

The area under the band at 3543 $cm^{-1}$ was also calculated for $F^-$ doped samples. Figure 3.13 represents the area under the band which corresponding to the OH…F bond. According to the Figure 3.13, the area under the band at 3543 $cm^{-1}$ increased with $F^-$ amount in the samples. The increase in the area becomes significant for 5 F sample when comparing with 1 F and 2.5 F. For the samples doped with $Zn^{2+}$ and $F^-$, a significant increase is seen between 2 Zn 1 F and 2 Zn 2.5 F, and between 2 Zn 2.5 F and 2 Zn 5 F. The difference in the area under the band at 3543 $cm^{-1}$ is the evidence of successful incorporation of $F^-$ ion into the HA structure with the ion amounts of 1 mol.%, 2.5 mol.% and 5 mol.%.

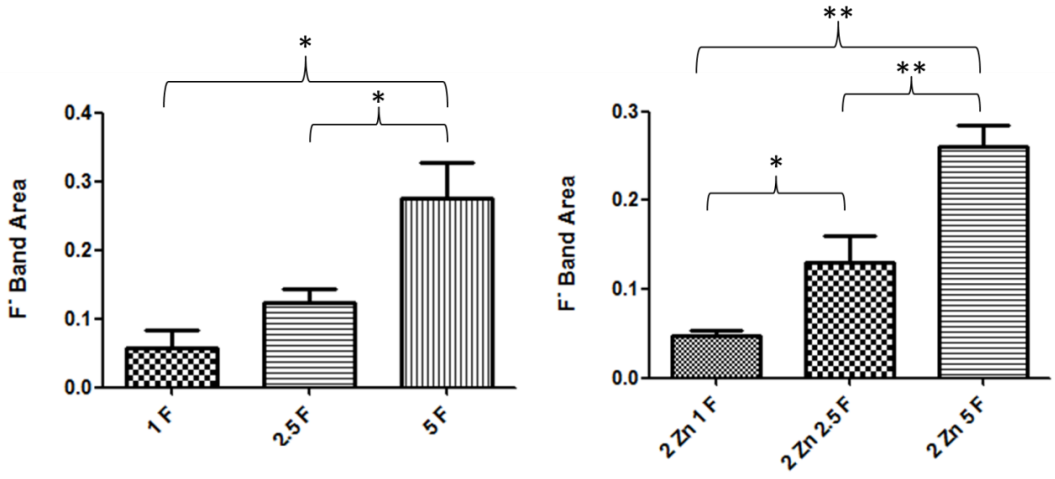


**Figure 3.13.** The OH…F band area at 3543 $cm^{-1}$ for pure HA and $Zn^{2+}$ and/or $F^-$ doped samples. (Paired student t-test was applied by using Minitab Statistical Software, USA: * denotes $p<0.05$ and ** denotes $p<0.01$.)

In Figures 3.9 and 3.11, the band at 3403 $cm^{-1}$ is seen only in $Zn^{2+}$ doped samples. Therefore, this band was assigned to the Zn-O symmetrical stretching. $F^-$ doping resulted in shift to the smaller wavenumbers whereas $Cl^-$ doping did not change the locations of the bands at 3403 $cm^{-1}$. The band at 3403 $cm^{-1}$ is the indicator of successful incorporation of $Zn^{2+}$ ion into the HA structure.

In Figure 3.14, the FTIR absorbance spectra of $Zn^{2+}$ and/or $Cl^-$ doped samples are seen between the wavenumbers 3600 and 3320 $cm^{-1}$. As can be seen from figure 3.14, there are three peaks at 3570, 3495 and 3403 $cm^{-1}$ in 3600-3320 $cm^{-1}$ region. The $OH^-$ stretching band at 3570 $cm^{-1}$ was also observed in $Cl^-$ doped samples. The difference in the intensities of the bands was observed by second derivative of the spectra (Figures 3.16 and 3.17) due to the fact that the absorbance of $OH^-$ stretching band at 3570 $cm^{-1}$ was low and could not be observed clearly. Moreover, there is no significant difference between the areas under the $OH^-$ stretching band at 3570 $cm^{-1}$ in $Cl^-$ doped samples. However, $Zn^{2+}$ and $Cl^-$ doped samples have significant decrease in the area under the band 3571 $cm^{-1}$ when compared with pure HA sample (Figure 3.15). Moreover, there is also a significant decrease in the area under the band 3571 $cm^{-1}$ of 2 Zn 2.5 Cl when compared with 2 Zn (Figure 3.15). The

decrease in intensity and the area under the band at 3571 $cm^{-1}$ indicated that the concentration of the functional group $OH^-$ decreased in HA structure with $Cl^-$ addition. $Cl^-$ ion replaces with $OH^-$ ion. Therefore, as the $Cl^-$ amount in the HA structure increased, $OH^-$ concentration decreased [208, 209]. It is the evidence of the successful incorporation of $Cl^-$ ion into the HA structure with the amounts of 1mol.%, 2.5 mol.% and 5 mol.%.

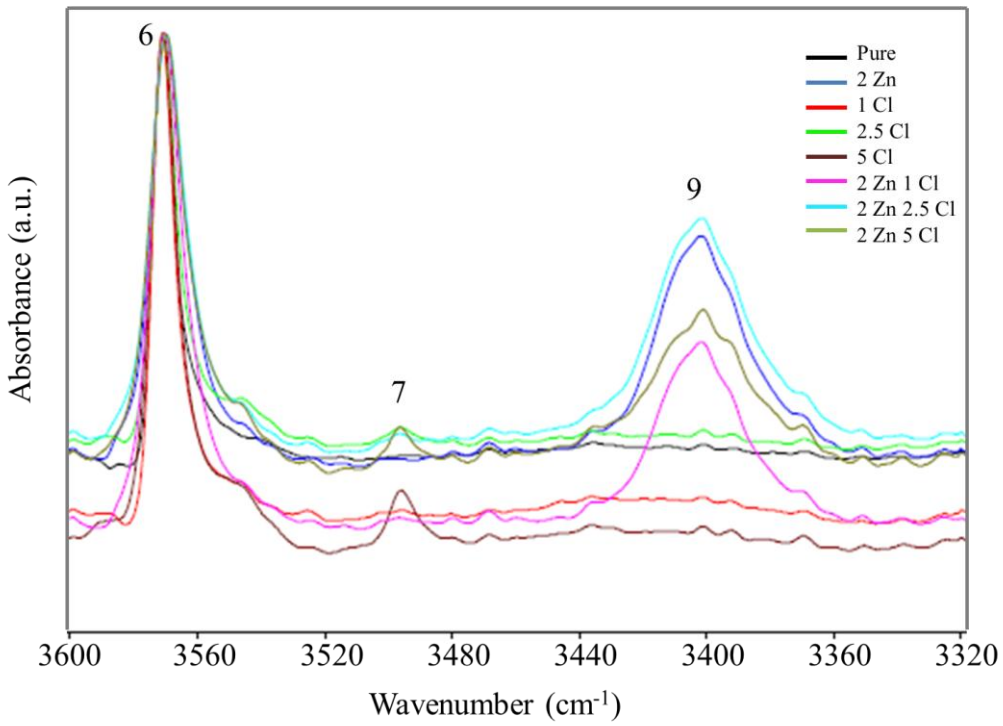


**Figure 3.14.** FTIR absorbance spectra of pure HA, $Cl^-$ and/or $Zn^{2+}$ doped samples in 3600-3320 $cm^{-1}$ region. (Normalization was done at peak 3575 $cm^{-1}$.)

The band at 3495 $cm^{-1}$ appeared with $Cl^-$ addition to the HA. Therefore, this band is related with OH…Cl bond. In Figure 3.14, this little band was not seen clearly. However, when the second derivative of the spectra was taken, the band at 3495 $cm^{-1}$ can be observed clearly. No significant shift was detected in wavenumbers between $Cl^-$ doped samples at 3495 $cm^{-1}$. The observation of the band at 3495 $cm^{-1}$ is the indicator of successful incorporation of the $Cl^-$ ion into the HA

structure.

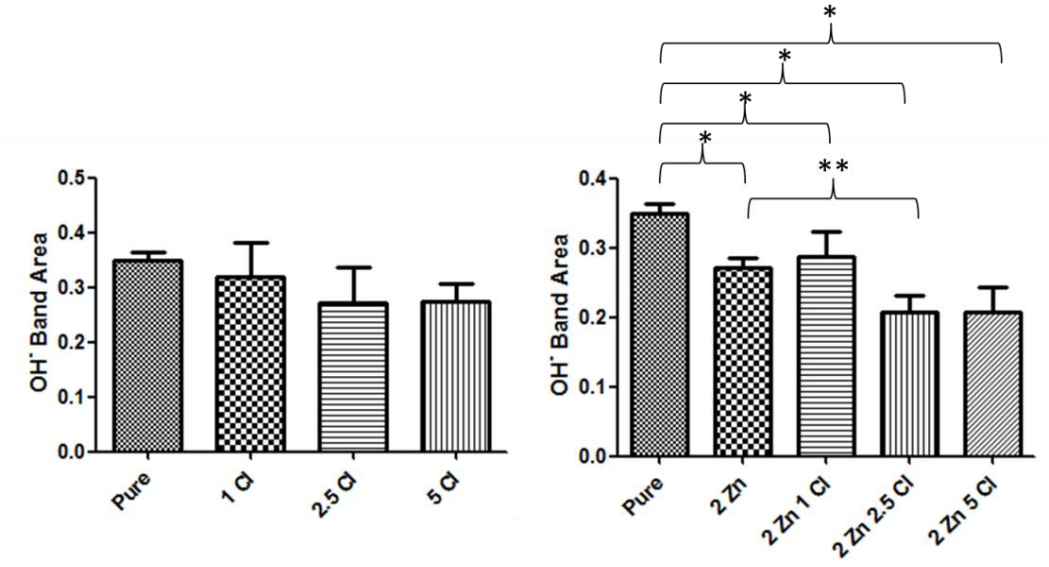


**Figure 3.15.** The $OH^-$ stretching band area at 3570 $cm^{-1}$ for pure HA and $Zn^{2+}$ and/or $Cl^-$ doped samples. (Paired student t-test was applied by using Minitab Statistical Software, USA: * denotes $p<0.05$ and ** denotes $p<0.01$.)

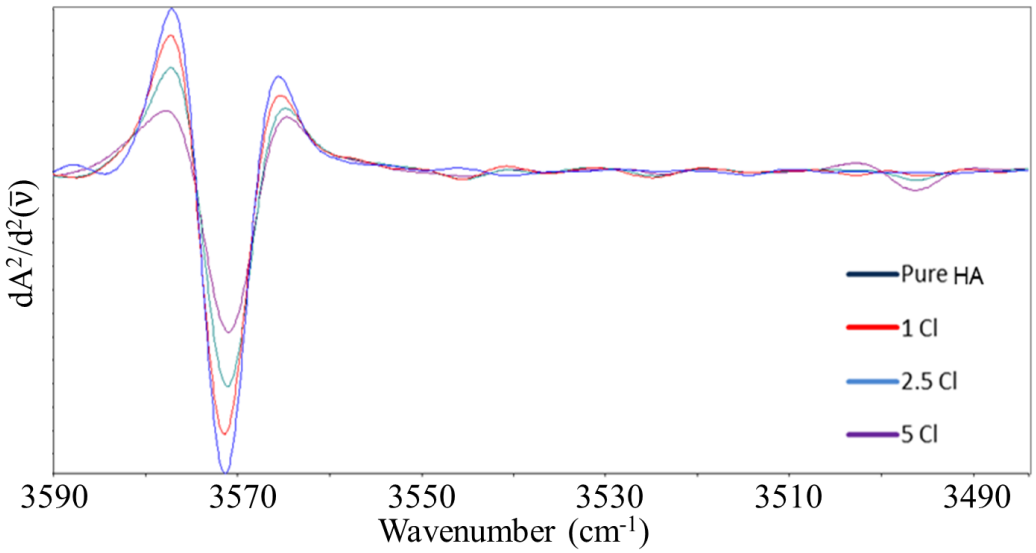


**Figure 3.16.** Second derivative FTIR spectra of pure HA, 1 Cl, 2.5 Cl and 5 Cl in 3590-3490 $cm^{-1}$ region.

Moreover, as the $Cl^-$ amount in the samples increased, the intensity of the band at 3495 $cm^{-1}$ increased (Figure 3.14). The increase in the intensity can be interpreted as the increase in the concentration of $Cl^-$ ion in the HA structure [208, 209]. In Figures 3.18 and 3.19, second derivative of the 3495 $cm^{-1}$ band are represented. Second derivative of the spectra are used in order to detect small bands more precisely. According to Figures 3.18 and 3.19, the area under the band at 3495 $cm^{-1}$ increased with $Cl^-$ amount. For more accurate information, the area under the band at 3495 $cm^{-1}$ was calculated for $Cl^-$ doped samples. The results are represented in Figure 3.20. There is a significant increase in the area under the band at 3495 $cm^{-1}$ between 1 Cl and 5 Cl. Moreover, when $Zn^{2+}$ was incorporated into the samples, the area under the band at 3495 $cm^{-1}$ decreased. The difference between 2 Zn 2.5 Cl and 2 Zn 5 Cl becomes significant in addition to the difference between 2 Zn 1 Cl and 2 Zn 5 Cl (Figure 3.20). The change in the area under the band at 3495 $cm^{-1}$ is the indicator of gradually incorporation of $Cl^-$ ions into HA structure with the amounts of 1 mol.%, 2.5 mol.% and 5 mol.%.

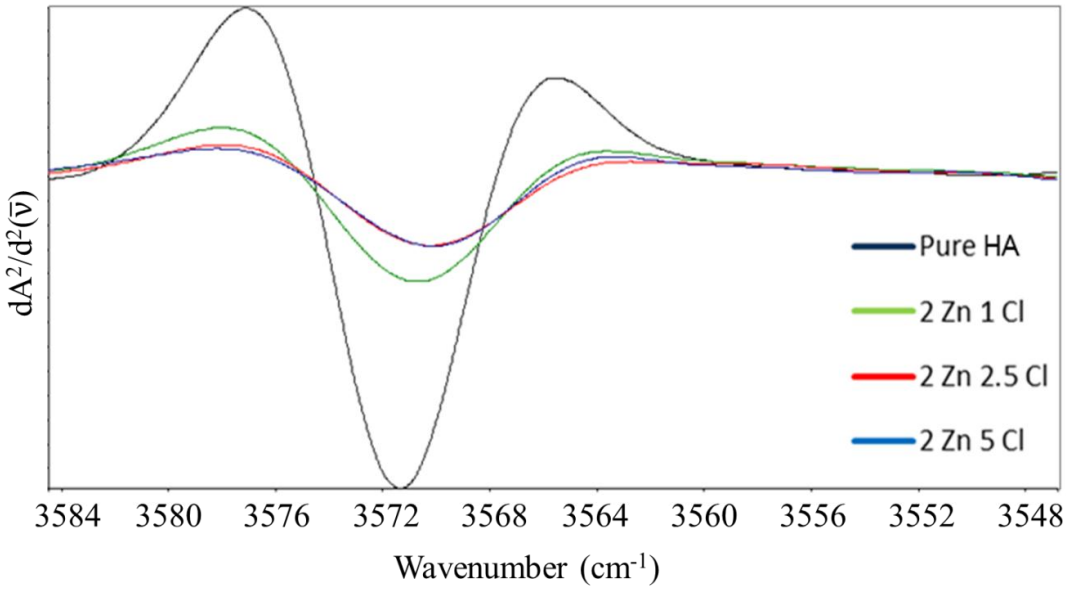


**Figure 3.17.** Second derivative FTIR spectra of pure HA, 2 Zn 1 Cl, 2 Zn 2.5 Cl and 2 Zn 5 Cl in 3584-3548 $cm^{-1}$ region.

$OH^-$ stretching band was highly affected by $F^-$ addition. However, $Cl^-$ addition did not affect the $OH^-$ stretching band. Moreover, OH…F band can be realized easily whereas OH…Cl band can be observed clearly by second derivative of the spectra. This is due to the fact that $F^-$ ion fits into space that is formed by $OH^-$ ion whereas $Cl^-$ ion does not. This situation stems from the fact that $F^-$ ion has smaller ionic radius that than of $OH^-$ ion. Moreover, the ionic radius of these two ions are closer (1.35 Å for $OH^-$ ion, 1.31 Å for $F^-$ ion [200]). However, $Cl^-$ ion has higher ionic radius than that of $OH^-$ ion (1.81 Å for $Cl^-$ ion [200]). Therefore, for $Cl^-$ ion, it is difficult to fit in the space of $OH^-$ ion.

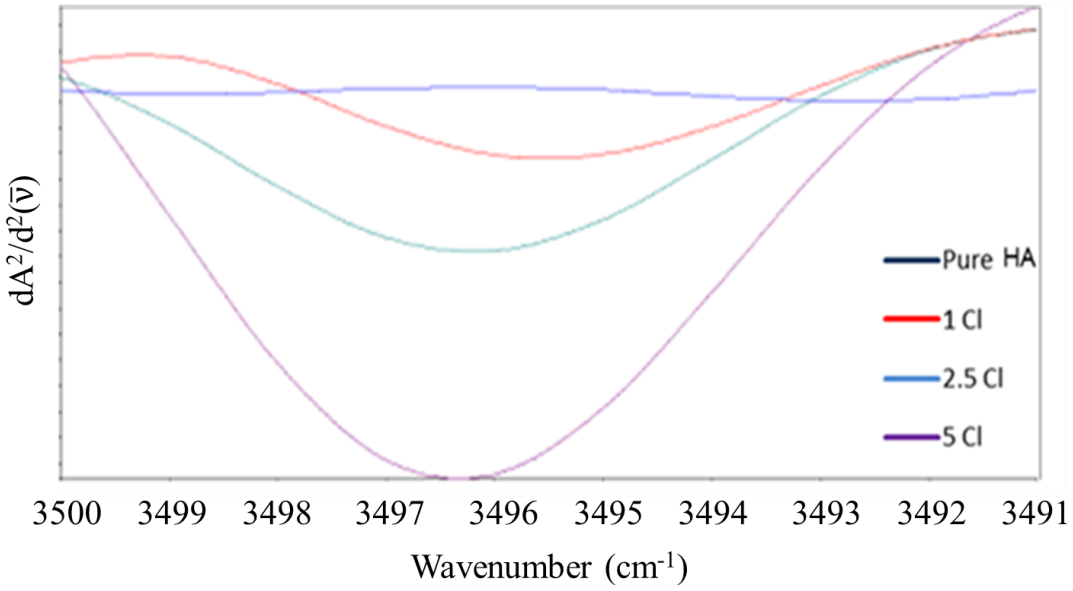


**Figure 3.18.** Second derivative FTIR spectra of pure HA, 1 Cl, 2.5 Cl and 5 Cl in 3500-3491 $cm^{-1}$ region.

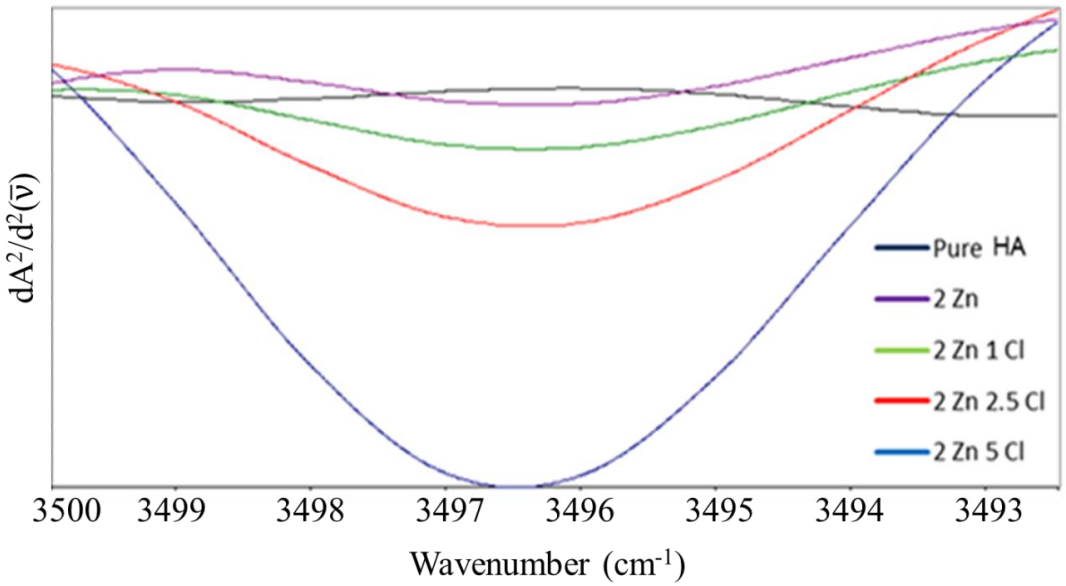


**Figure 3.19.** Second derivative FTIR spectra of pure HA, 2 Zn, 2 Zn 1 Cl, 2 Zn 2.5 Cl and 2 Zn 5 Cl in 3500-3493 $cm^{-1}$ region.

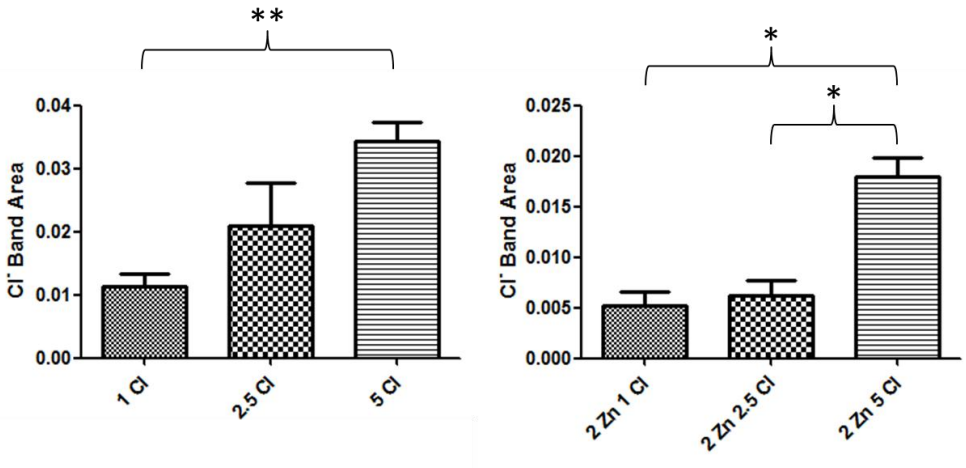


**Figure 3.20.** The OH…Cl band area at 3495 $cm^{-1}$ for pure HA and $Zn^{2+}$ and/or $Cl^{-}$ doped samples. (Paired student t-test was applied by using Minitab Statistical Software, USA: * denotes $p<0.05$ and ** denotes $p<0.01$.)

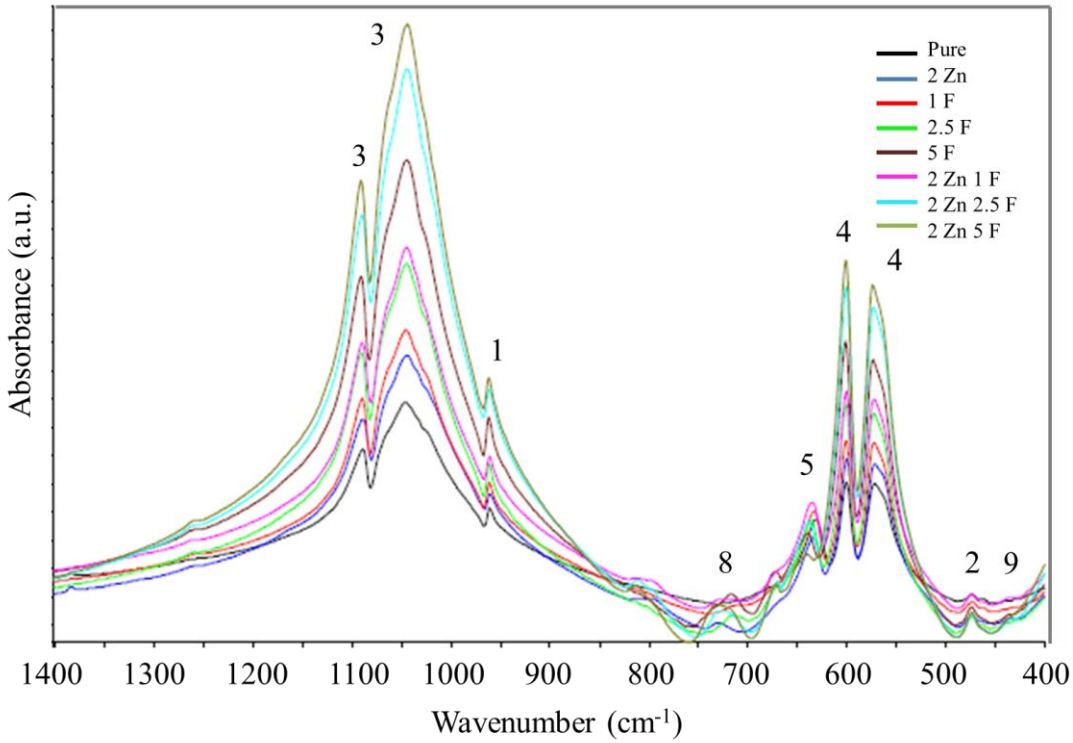


**Figure 3.21.** FTIR absorbance spectra of pure HA, $F^-$ and/or $Zn^{2+}$ doped samples in 1400-400 $cm^{-1}$ region. (Normalization was done at point 2820 $cm^{-1}$.)

The bands at 1091, 1045 and 960 $cm^{-1}$ correspond to the $\nu_3$, $\nu_3$ and $\nu_1$ vibrational modes of $(PO_4)^{3-}$ bond. $F^-$ addition resulted in small shifts to the higher wavenumbers at bands 1091 and 1045 $cm^{-1}$. However, no significant change was observed for the band at 960 $cm^{-1}$. $Cl^-$ doped samples had no significant change in locations of these three bands (Table 3.6 and 3.7). Moreover, the intensities and the areas under these three bands did not change with $Zn^{2+}$, $F^-$ or $Cl^-$ addition. However, between pure HA and 2 Zn, there are some differences in the area under the bands at 1091, 1045 and 960 $cm^{-1}$. There is a significant decrease in the area under these phosphate related bands in 2 Zn spectra when compared with pure HA spectra (paired t-test was applied by using Minitab Statistical Software, USA and $p<0.05$ was accepted as a significant difference). This is due to the fact that some $Zn^{2+}$ ions may replace with $P^{5+}$ ions in the $(PO_4)^{3-}$ or may distort $P^{5+}$ ions and break the bonds between $P^{5+}$ and $O^{2-}$.

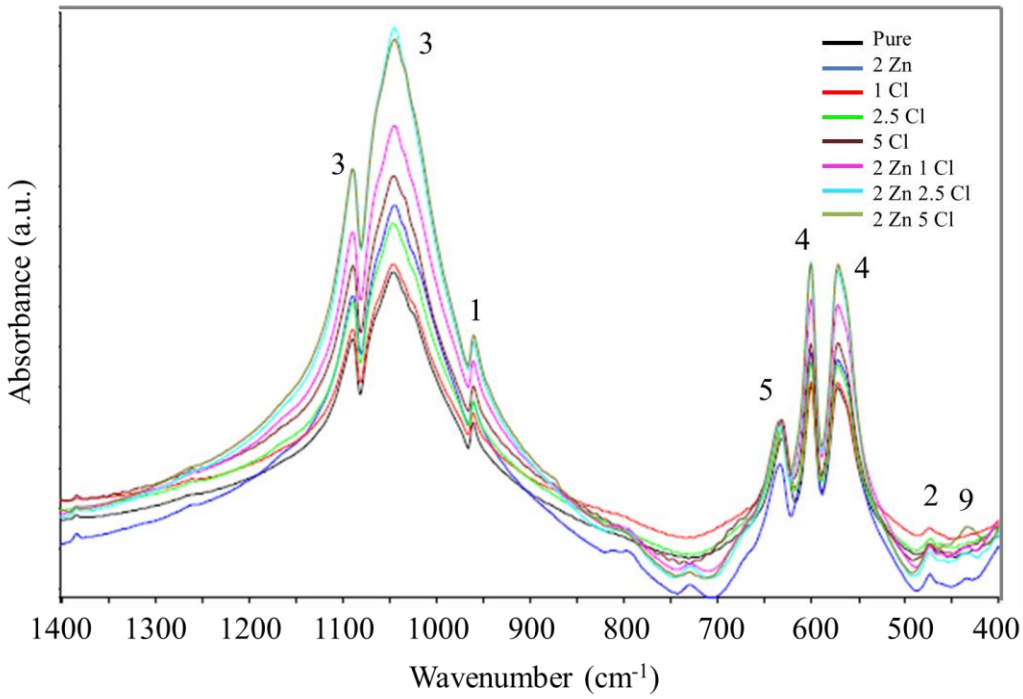


**Figure 3.22.** FTIR absorbance spectra of pure HA, $Cl^-$ and/or $Zn^{2+}$ doped samples in 1400-400 $cm^{-1}$ region. (Normalization was done at point 2820 $cm^{-1}$.)

The bands at 1091, 1045 and 960 $cm^{-1}$ are the evidence of formation of HA with the precipitation method successfully.

The bands between the wavenumbers 711 and 727 $cm^{-1}$ corresponded to the bond between OH…F. The band at 711 $cm^{-1}$ shifted to the higher wavenumbers with $F^-$ and $Zn^{2+}$ addition (Table 3.7). In Figure 3.23, the bands at between 711 and 727 $cm^{-1}$ can be seen clearly. However, in Figure 3.25, there is no such band which supports the fact that this band is related to $F^-$ ion. Shifts in wavenumbers to the low frequencies can be interpreted as the increase in the strength of hydrogen bonds in the structure and increase in bond formation in the structure [210, 211]. However, for the band at 711 $cm^{-1}$, there was an increase in wavenumbers with $Zn^{2+}$ and $F^-$ addition which is inconsistent with other $F^-$ and $OH^-$ related bands.

**Table 3.7.** The band locations in FTIR spectra of the samples in the range of 960-433 $cm^{-1}$.

| Observed Wavenumbers ($cm^{-1}$) / Sample ID | 960 | 711 | 632 | 601 | 566 | 473 | 433 |
|---|---|---|---|---|---|---|---|
| Pure | 960 | - | 632 | 601 | 568 | 473 | - |
| 2 Zn | 959 | - | 635 | 600 | 567 | 474 | 433 |
| 1 F | 961 | 711 | 634 | 601 | 569 | 473 | - |
| 2.5 F | 961 | 713 | 637 | 601 | 569 | 474 | - |
| 5 F | 961 | 717 | 640 | 602 | 569 | 474 | - |
| 2 Zn 1 F | 961 | 719 | 636 | 601 | 569 | 474 | 433 |
| 2 Zn 2.5 F | 960 | 725 | 639 | 601 | 569 | 474 | 435 |
| 2 Zn 5 F | 961 | 727 | 640 | 602 | 570 | 474 | 434 |
| 1 Cl | 960 | - | 632 | 601 | 569 | 474 | - |
| 2.5 Cl | 960 | - | 632 | 601 | 568 | 473 | - |
| 5 Cl | 960 | - | 632 | 601 | 568 | 474 | - |
| 2 Zn 1 Cl | 960 | - | 634 | 601 | 568 | 473 | 434 |
| 2 Zn 2.5 Cl | 960 | - | 636 | 600 | 568 | 473 | 434 |
| 2 Zn 5 Cl | 959 | - | 635 | 601 | 570 | 472 | 432 |

The area under the band at 711 $cm^{-1}$ was also calculated for $F^-$ doped samples. The results were represented in Figure 3.24. According to the Figure 3.24, there is an increase in the area under the band at 711 $cm^{-1}$ with $F^-$ addition. Significant increase is seen between the samples 1 F and 5 F, and also 2.5 F and 5 F. In $F^-$ and $Zn^{2+}$ doped samples, the changes in the area values are significant for all samples [212]. The increase in the area under the band at 711 $cm^{-1}$ is indicator of an increase in the concentration of $F^-$ functional group in HA structure [209, 213]. Like the

band at 3543 $cm^{-1}$, the band at 711 $cm^{-1}$ is the indicator of successful addition of $F^-$ ion into the HA structure.

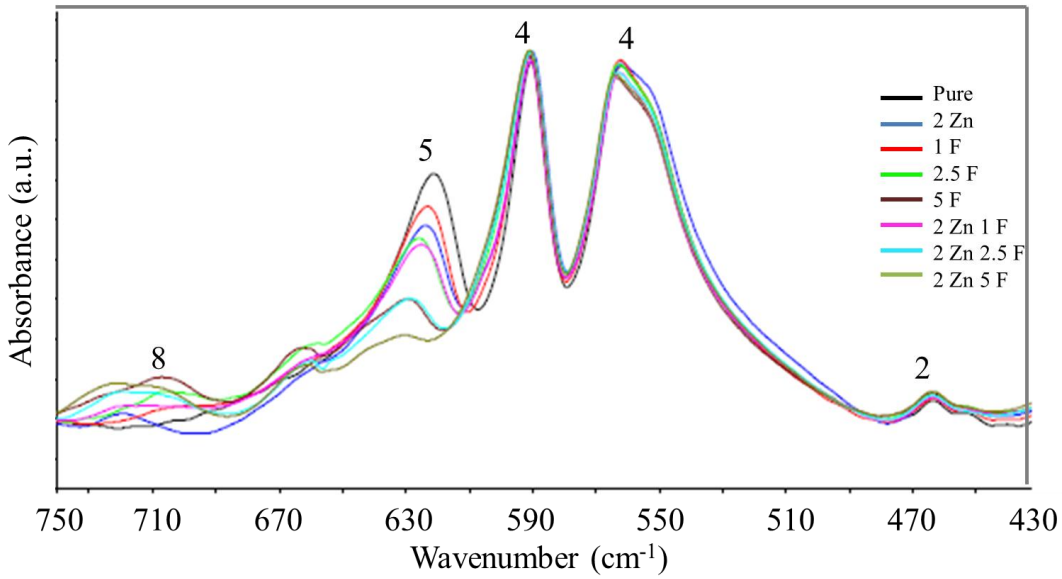


**Figure 3.23.** FTIR absorbancespectra of pure HA, $F^-$ and/or $Zn^{2+}$ doped samples in 750-430 $cm^{-1}$ region. (Normalization was done at peak 490 $cm^{-1}$.)

In Table 3.7, the band at 632 $cm^{-1}$ corresponded to $OH^-$ librational mode was shifted to 635 $cm^{-1}$ by 2 mol.% $Zn^{2+}$ addition [144]. $F^-$ ion doping also increased the wavenumber of the pure HA. Increase in wavenumber with $F^-$ ion amount was also seen in $F^-$ and $Zn^{2+}$ doped samples. No change in locations was observed for $Cl^-$ doped samples. The shifts to higher wavenumbers with $F^-$ and $Zn^{2+}$ ion addition at 632 $cm^{-1}$ band show inconsistent pattern with the OH…F and $OH^-$ stretching bands observed between 3600 $cm^{-1}$ and 3403 $cm^{-1}$ [210, 211]. Some fluctuations were seen in $Cl^-$ and $Zn^{2+}$ doped samples at 632 $cm^{-1}$. However, when compared with $F^-$ doped samples, these fluctuations became negligible.

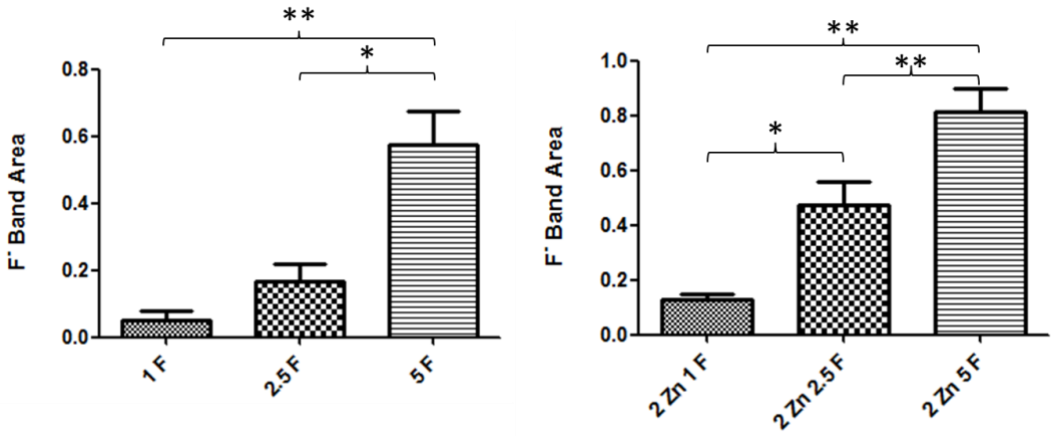


**Figure 3.24.** The OH…F band area at 711 $cm^{-1}$ for pure HA and $Zn^{2+}$ and/or $F^-$ doped samples. (Paired student t-test was applied by using Minitab Statistical Software, USA: * denotes $p<0.05$ and ** denotes $p<0.01$.)

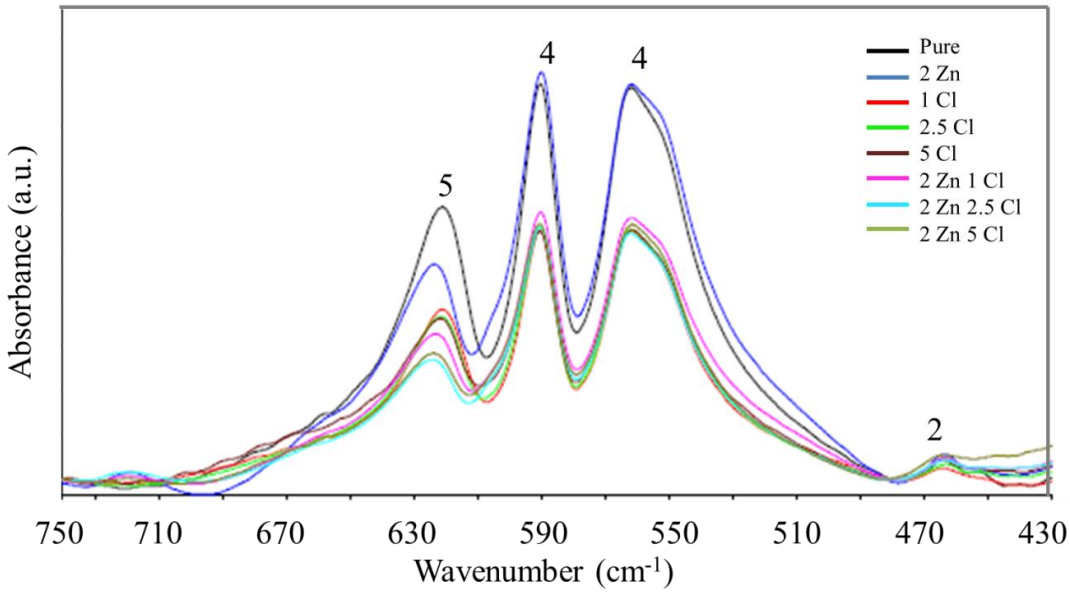


**Figure 3.25.** FTIR absorbance spectra of pure HA, $Cl^-$ and/or $Zn^{2+}$ doped samples in 750-430 $cm^{-1}$ region. (Normalization was done at peak 490 $cm^{-1}$.)

The intensity of $OH^-$ librational band decreased with addition of $Cl^-$ and $F^-$ ions because of the fact that these two ions replaces with $OH^-$ ion (Figures 3.23, 3.25). This is also the indicator of successful incorporation of $Cl^-$ and $F^-$ ions into the HA

structure. For more precise results, the area under this band was also calculated for $F^-$ and $Cl^-$ doped samples. The results are represented in Figures 3.26 and 3.27. The decrease in the intensity of $OH^-$ librational band is indicator of a decrease in the concentration of $OH^-$ functional group [209, 213]. As the $F^-$ and $Cl^-$ ion concentration in the structure increased, the replacement with $OH^-$ ion increased. The replacement with $OH^-$ ion decreased the concentration of $OH^-$ ion in the HA structure which resulted in decrease in intensity and the area under the band at 632 $cm^{-1}$.

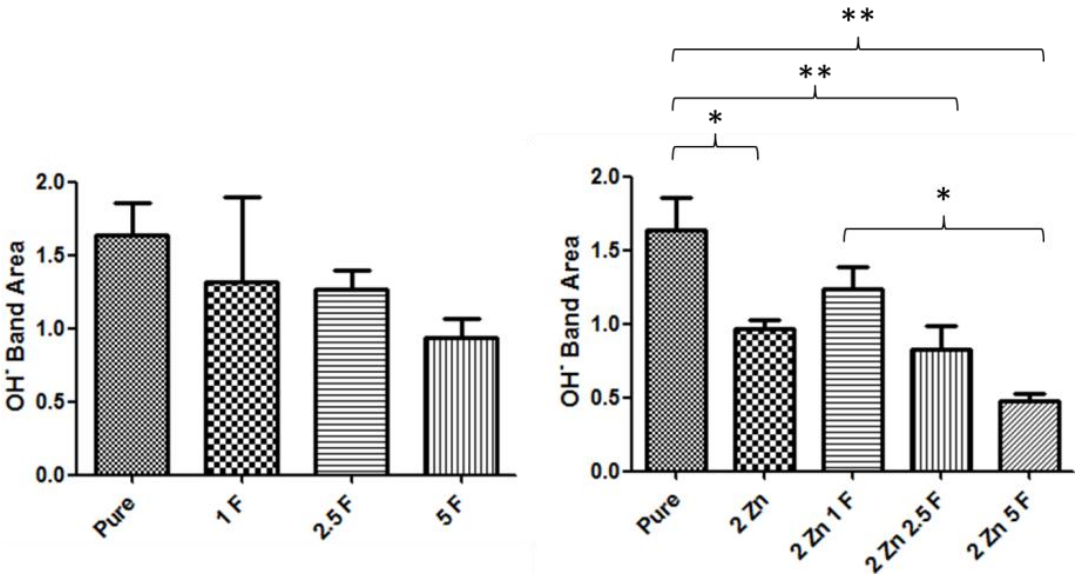


**Figure 3.26.** The $OH^-$ librational and area at 632 $cm^{-1}$ for pure HA and $Zn^{2+}$ and/or $F^-$ doped samples. (Paired student t-test was applied by using Minitab Statistical Software, USA: * denotes $p<0.05$ and ** denotes $p<0.01$.)

In Figure 3.26, a decrease in $OH^-$ librational band area with $F^-$ addition is observed. However, changes in the areas do not have significant meanings. However, when $Zn^{2+}$ ion is incorporated to the HA structure, it results in significant changes in the areas under the band at 632 $cm^{-1}$. The decrease in the band areas at 632 $cm^{-1}$ with $F^-$ addition is seen in $F^-$ and $Zn^{2+}$ co-doped samples in Figure 3.26. Comparing with $OH^-$ stretching band, $OH^-$ librational band was affected less by $F^-$ addition.

In Figure 3.27, the area under the band at 632 $cm^{-1}$ of $Cl^-$ and/or $Zn^{2+}$ doped samples is shown. When comparing with pure HA, there is a decrease in the area of the band at 632 $cm^{-1}$. However, no difference is observed among $Cl^-$ doped samples. Due to the differences between the ionic radius of $OH^-$ ion and $Cl^-$ ion, replacement of $Cl^-$ ion with $OH^-$ ion became problemeatic [200]. Therefore, the differences under the area of band at 632 $cm^{-1}$ changes insignificantly. $Zn^{2+}$ ion incorporation to the structure results in further decrease in the area under the band at 632 $cm^{-1}$. However, the difference between $Cl^-$ doped samples is negligible. Pure sample has the highest value and there is a significant difference between pure HA and $Zn^{2+}$ and $Cl^-$ co-doped samples.

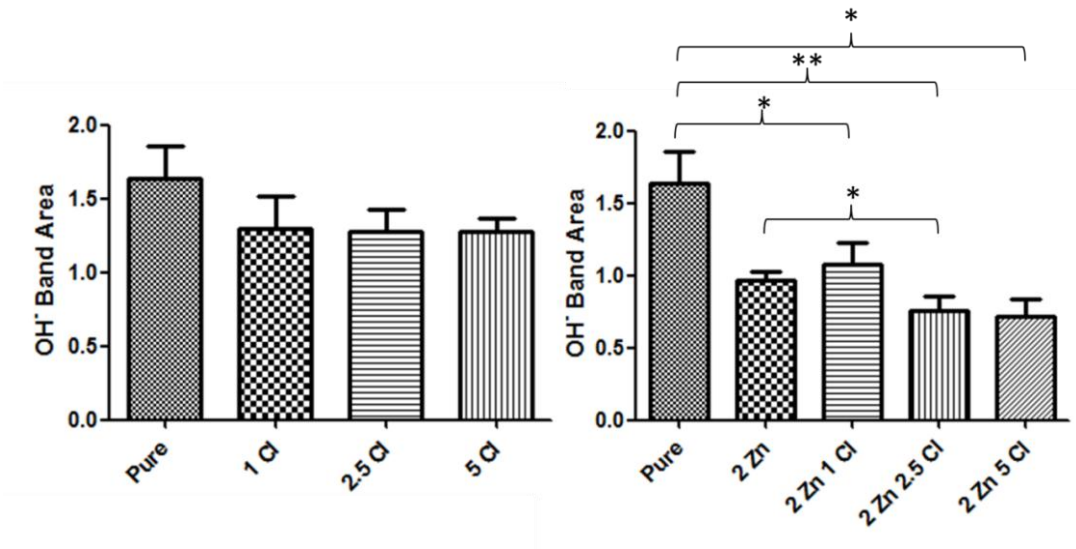


**Figure 3.27.** The $OH^-$ librational band area at 632 $cm^{-1}$ for pure HA and $Zn^{2+}$ and/or $Cl^-$ doped samples. (Paired student t-test was applied by using Minitab Statistical Software, USA: * denotes $p<0.05$ and ** denotes $p<0.01$.)

The bands at 601 and 568 $cm^{-1}$ corresponded to $(PO_4)^{3-}$ with vibrational mode of $\nu_4$. No significant difference in wavenumbers was detected for these bands. The wavenumbers changed between 600-602 $cm^{-1}$ and 567-570 $cm^{-1}$ for 601 $cm^{-1}$ and 568 $cm^{-1}$ bands, respectively [205, 206]. Another band related with $(PO_4)^{3-}$ group was detected at 473 $cm^{-1}$ which corresponded to the vibrational mode of $\nu_2$ [214]. There was not any significant shift for the band at 473 $cm^{-1}$ according to Table 3.7

(Figures 3.23, 3.25). The bands at 601, 568 and 473 $cm^{-1}$ have nearly the same intensities in all samples. This is an indicator of the fact that $Zn^{2+}$, $Cl^-$ and $F^-$ addition did not affect these $(PO_4)^{3-}$ related bands. These three bands at 601, 568 and 473 $cm^{-1}$ are also the evidence of formation of HA structure with the solution precipitation method.

There was a small band at 433 $cm^{-1}$ in $Zn^{2+}$ containing samples [204]. Therefore, this band was assigned to Zn-O symmetrical stretching band. Insignificant fluctuations between $Zn^{2+}$ doped samples were seen around this band. The wavenumbers were between 432 and 435 $cm^{-1}$ (Table 3.7).

To conclude that $(PO_4)^{3-}$ related bands detected at 1091, 1045, 960, 601, 568 and 473 $cm^{-1}$ and $OH^-$ related bands detected at 632 (librational) and 3571 (stretching) $cm^{-1}$ are the indicator of the fact that HA synthesis is successful. The bands detected at 3495 $cm^{-1}$ in $Cl^-$ doped samples showed that $Cl^-$ was successfully incorporated into the HA structure. Moreover, the bands at 3543 and 711 $cm^{-1}$ were detected in $F^-$ doped samples. The detection of these bands showed the fact that $F^-$ ion was accepted by the structure of HA. The decrease in the intensities of $OH^-$ related bands and the decrease in the areas under the $OH^-$ related bands with the $F^-$ and $Cl^-$ ion addition showed that $OH^-$ ion replaced with $F^-$ and $Cl^-$ ions. Furthermore, the bands at 3403 and 433 $cm^{-1}$ were detected only in $Zn^{2+}$ doped samples. This situation showed that $Zn^{2+}$ was incorporated into the HA structure successfully.

### 3.1.4. SEM Analysis

Figures 3.28-3.32 represent the SEM pictures of related groups. The morphology of the samples were investigated. No significant difference was seen between the SEM images. It can be easily observed from the SEM images that grain sizes of the samples increased by $Zn^{2+}$ addition and $F^-$ addition. $Cl^-$ addition decreased the grain sizes whereas $Zn^{2+}$ incorporation to $Cl^-$ doped samples increased the grain sizes. However, for more precise results, grain sizes were

calculated in Table 3.8 by using the Lorenzian crystallite size obtained from Rietwelt analysis.

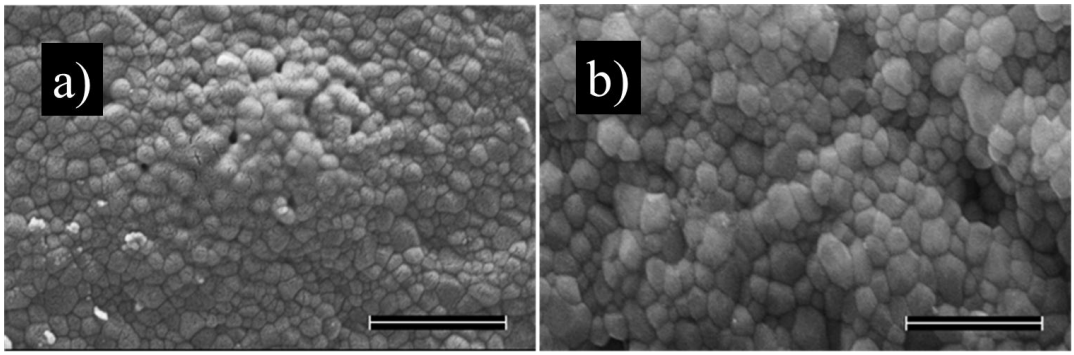


**Figure 3.28.** SEM results of Group 1; a) pure HA; b) 2 Zn (Scale bar is 2 µm, magnification is 30000X).

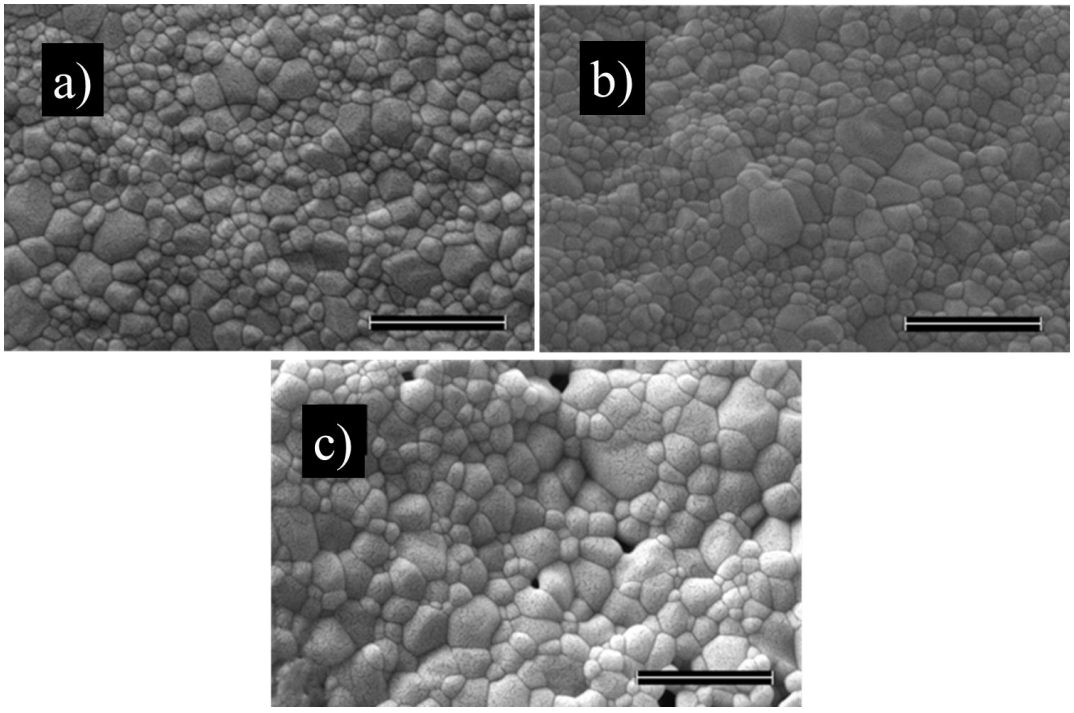


**Figure 3.29.** SEM results of Group 2; a) 1 F; b) 2.5 F; c) 5 F (Scale bar is 2 µm, magnification is 30000X).

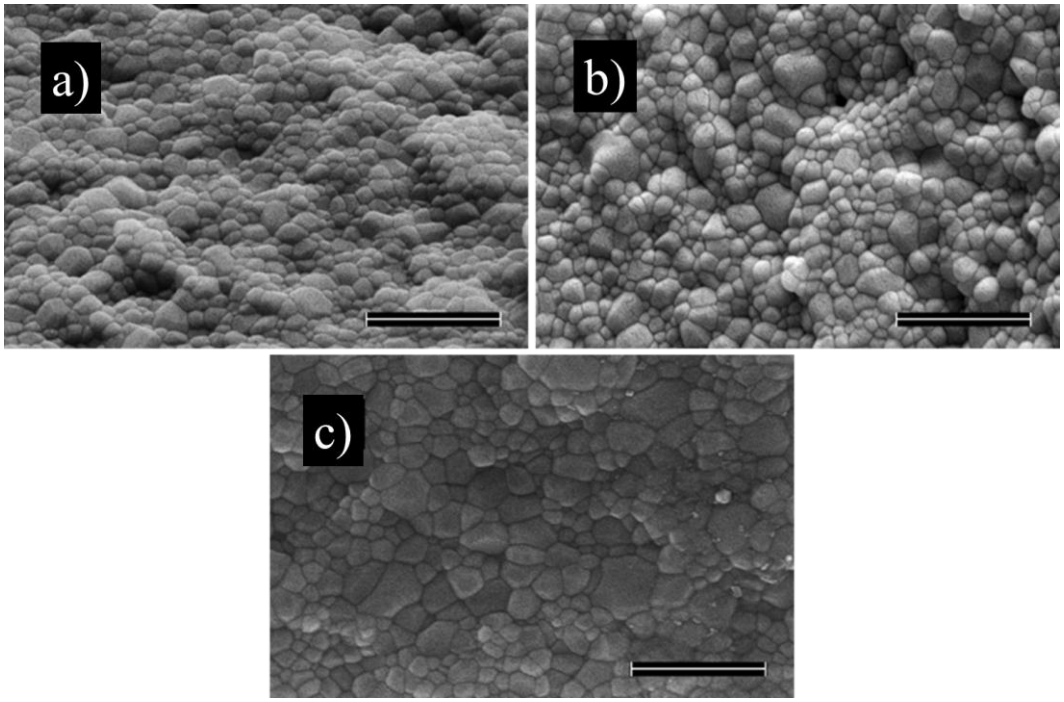


**Figure 3.30.** SEM results of Group 3; a) 2 Zn 1 F; b) 2 Zn 2.5 F; c) 2 Zn 5 F (Scale bar is 2 μm, magnification is 30000X).

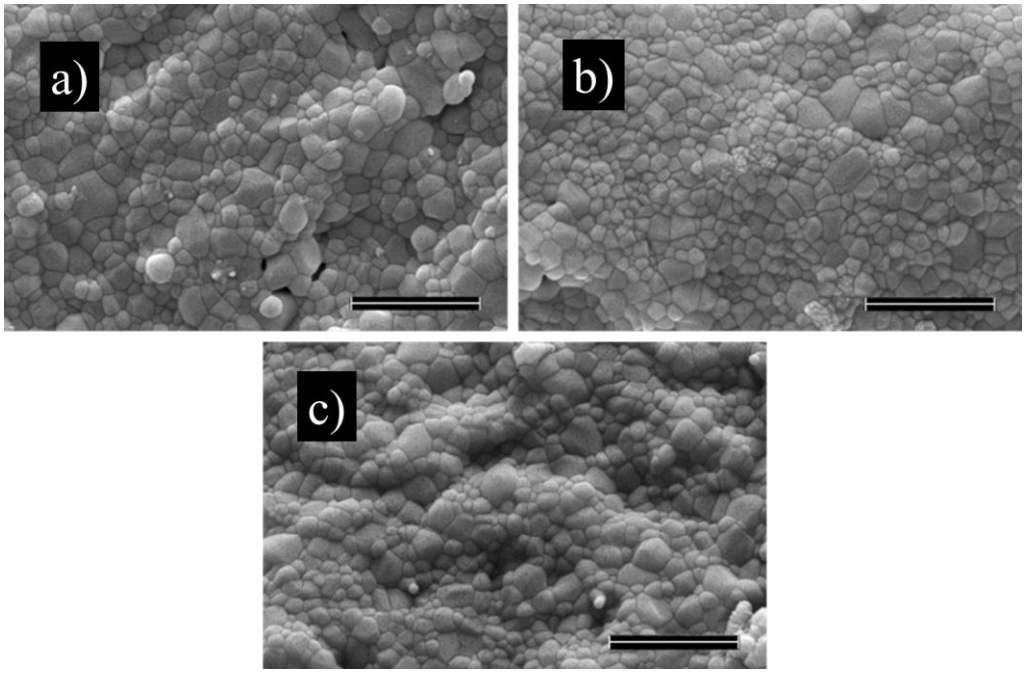


**Figure 3.31.** SEM results of Group 4; a) 1 Cl; b) 2.5 Cl; c) 5 Cl (Scale bar is 2 μm, magnification is 30000X).

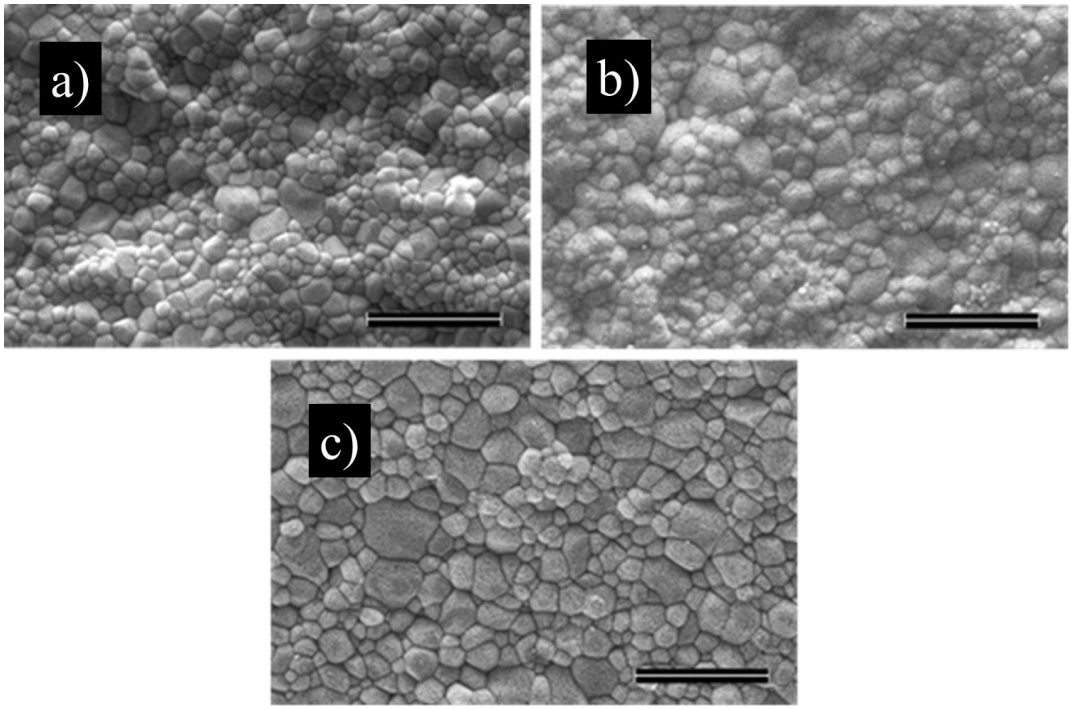


**Figure 3.32.** SEM results of Group 5; a) 2 Zn 1 Cl; b) 2 Zn 2.5 Cl; c) 2 Zn 5Cl (Scale bar is 2 μm, magnification is 30000X).

According to the results, $Zn^{2+}$ addition decreased the grain size of pure HA according to Rietvelt analysis results. In a study, the effect of doping of diavalent and trivalent ions into HA was investigated. The pure and doped samples were synthesized by precipitation method. The samples were sintered at 1100°C for 1h. It was found that HA doped with diavalent ions such as $Mg^{2+}$ and $Zn^{2+}$ had higher average grain size than pure HA have. However, trivalent ions such as $Y^{3+}$, $In^{3+}$, $La^{3+}$, $Bi^{3+}$ decreased the average grain size of pure HA [165]. In this study, undoped HA had the average grain size of 1.12 μm [165]. Moreover, 5% wt. $Zn^{2+}$ doped HA had the average grain size of 2.27 μm [165]. In another study, Ergun et al. synthesized pure HA and 2% by mole $Zn^{2+}$ doped HA by precipitation method. The samples were sintered at 1100°C for 1h [137]. According to the study, the average grain size of pure HA was found as 0.56 μm, whereas $Zn^{2+}$ doped samples had the average grain size of 0.32 μm [137]. Therefore, it was concluded that $Zn^{2+}$

addition decreased the grain size of HA. In the current study, smaller grain sized materials were obtained. For pure HA, it was 0.19 μm and for 2 Zn, it was 0.18 μm.

**Table 3.8.** Average grain size of the samples calculated by Rietvelt Analysis.

| Group ID | Sample ID | Grain size (nm) by Rietvelt Analysis |
|---|---|---|
| Group 1 | Pure | 191 |
| | 2 Zn | 183 |
| Group 2 | 1 F | 186 |
| | 2.5 F | 190 |
| | 5 F | 182 |
| Group 3 | 2 Zn 1 F | 176 |
| | 2 Zn 2.5 F | 166 |
| | 2 Zn 5 F | 188 |
| Group 4 | 1 Cl | 199 |
| | 2.5 Cl | 181 |
| | 5 Cl | 160 |
| Group 5 | 2 Zn 1 Cl | 209 |
| | 2 Zn 2.5 Cl | 187 |
| | 2 Zn 5 Cl | 203 |

There were also studies which investigated the effect of ZnO on TCP and HA [187]. In one of these studies ZnO was added into HA and TCP with different amounts with a range from 0% to 3.5% by mole. The samples were sintered at 1250°C for 3h. It was investigated that, ZnO did not have any significant effect on microstructures of HA. The average grain size was found between 5 and 6 μm. However, in case of TCP, ZnO addition decreased the grain sizes significantly.

Moreover sintering temperature was also an important parameter for grain growth. Increase in the sintering temperature (1300°C) increased the grain sizes due to high temperature grain growth [187]. Moreover, in a study it was also investigated that, addition of ZnO with a percentage of 0.25 by weight decreased the grain size of TCP by 12% when the samples were prepared by solid state reactions and sintered at 1250°C for 2h [215].

$F^-$ addition also decreased the grain size of pure HA according to results of Rietvelt analysis. As the amount of $F^-$ increased in the samples, the grain size decreased. However, in 2.5 F, an unexpected increase in grain size were observed. Co-doping of $F^-$ and $Zn^{2+}$ ions resulted in further decrease in grain sizes. As the amount of $F^-$ increased up to 2.5 mol.%, grain sizes decreased. However, 5 mol.% addition of $F^-$ increased the grain size of the samples. However, the values are still lower than grain size of HA.

Sun et al. investigated the grain sizes of $Mg^{2+}$ and $F^-$ doped HA that was synthesized by precipitation method and sintered at 1100°C for 1h [147]. According to the results, all doped samples resulted in smaller grain sizes than pure HA have. Moreover, $Mg^{2+}$ and $F^-$ co-doped samples showed further decreases in grain sizes [147]. The obtained grain sizes were ranged from 195 to 278nm [147]. In another study, HA and 50% $F^-$ substituted HA was synthesized by precipitation method and sintered at 1250°C for 1h and 1100°C for 3h, separately [190]. According to the SEM images, grain growth and coalescence with some small pores were seen in HA powder [190]. $F^-$ substituted sample had a limited porosity when compared with pure HA [190]. When sintering temperature was decreased to 1100°C and sintering time increased up to 3h, no grain growth and coalescence were seen and more porous structures were obtained [190]. In the current study, grain growth can be seen clearly. Toker et al. also investigated the effect of $F^-$ doping on HA and found that F- ion addition decreased the grain sizes of pure HA [188].

The grain sizes of $Cl^-$ doped samples were in the range of 0.199-0.160µm. 1 mol.% $Cl^-$ addition increased the grain size of pure HA. However, as the $Cl^-$ amount increased, the grain sizes of the samples decreased. Co-doping of $Zn^{2+}$ and $Cl^-$ ions

increased the grain size of pure HA. However, a sharp decrease was seen in 2 Zn 2.5 Cl when compared with $Zn^{2+}$ and $Cl^-$ co-doped samples. Decrease in grain sizes with $Cl^-$ addition was seen in $Zn^{2+}$ and $Cl^-$ co-doped sample like in $Cl^-$ doped samples.The presence of CaO phase also may have a role in high grain sizes of $Cl^-$ doped samples.

In a study, pure HA, chlorapatite and three different compositions of $Cl^-$ substituted HA were synthesized by precipitation method [193]. The samples sintered at 1200°C for 2h. According to the SEM images, pure HA had less porosity than $Cl^-$ substituted samples. As the $Cl^-$ amount in the samples increased, their porosity increased. The chlorapatite had the highest porosity among other $Cl^-$ added samples. The porosity of the ceramics had a significant effect on the mechanical properties. It was investigated that significanly porous materials had low mechanical performance [193].

### 3.2. Mechanical Analysis

In terms of mechanical analysis, Vickers micro-hardness test was applied to the samples. Fracture toughness and Vickers micro-hardness values were calculated.

#### 3.2.1. Vickers Micro-hardness

Vickers microhardness values are represented in Table 3.9. According to the results, $Zn^{2+}$ addition decreases the microhardness of the pure HA, slightly. $F^-$ addition into HA also decreases microhardness of pure HA. However, as $F^-$ amount increases the microharness of the samples are improved. 2.5 F gives the lowest microhardness result. However, its standard deviation is highest. Therefore, it can be said that by $F^-$ addition microhardness values increase. This is due to the fact that $F^-$ decreased the porosity of the samples which resulted in more compact and hard structure [139]. Moreover, the high affinity between F and H atoms played an important role in formation of this compact structure [188].

**Table 3.9.** Vickers microhardness of the samples sintered at 1100 °C for 1h.

| Group Name | Compound Name | Vickers Microhardness (GPa) |
|---|---|---|
| Group 1 | Pure | 5.826 ± 0.055 |
| | 2 Zn | 5.756 ± 0.174 |
| Group 2 | 1 F | 5.030 ± 0.338 |
| | 2.5 F | 4.777 ± 1.393 |
| | 5 F | 5.073 ± 0.951 |
| Group 3 | 2 Zn 1 F | 5.771 ± 0.204 |
| | 2 Zn 2.5 F | 6.057 ± 0.243 |
| | 2 Zn 5 F | 6.262 ± 0.170 |
| Group 4 | 1 Cl | 5.229 ± 0.486 |
| | 2.5 Cl | 5.490 ± 0.386 |
| | 5 Cl | 6.001 ± 0.361 |
| Group 5 | 2 Zn 1 Cl | 5.611 ± 0.392 |
| | 2 Zn 2.5 Cl | 4.934 ± 0.589 |
| | 2 Zn 5 Cl | 5.148 ± 0.619 |

In a study HA/yttria-doped alumina composite and HA/yttria-doped zirconia composites and the effect of fluorapatite that were added to HA with a percentage of 80 were investigated [139]. According to the results, after sintering the composites at 1400°C for 3h, the samples including $F^-$ had a significant decrease in porosity. It is found that $F^-$ addition increased the Vickers microhardness values significantly. The reason of this increase was explained as the decrease in porosity of fluoridated samples [139]. In another study, HA and 50% $F^-$ substituted HA was synthesized by precipitation method and sinetered at 1250°C for 1h [190]. According to the Vickers microhardness test applied to the samples, $F^-$ addition resulted in a slight increase in microhardness values at all applied loads [190]. Sun et al. investigated Vickers microhardness of $Mg^{2+}$ and $F^-$ doped HA that was synthesized by precipitation method and sintered at 1100°C for 1h [147]. According to the results, $Mg^{2+}$ doping decreased the microhardness values. As the amount of

$Mg^{2+}$ doping increased, the microhardness decreased. However, $F^-$ addition improved the microhardness values. It was observed that as the amount of $F^-$ increased, the microhardness values also increased [147]. Toker et al. found that $F^-$ addition increased the microhardness of pure HA up to a limit.

2 mol.% $Zn^{2+}$ incorporation to the $F^-$ doped samples is also investigated. It is observed that $Zn^{2+}$ addition improves the microhardness of $F^-$ doped samples. 2 Zn 2.5 F and 2 Zn 5 F samples give higher values than pure HA and 2 Zn (Figure 3.33). In another study ZnO was added into HA and TCP with different amounts with a range from 0% to 3.5% by mole. The samples were sintered at 1250°C for 3h. When Vickers microhardness values were investigated, it was found that, as ZnO amount increased in HA, the microhardness of the samples increased. However, 3.5% by mole addition of ZnO decreased the microhardness to a value higher than pure HA have. The highest microhardness value was 4.8 GPa and obtained for 2.5% by mole ZnO added HA. The reason of the increase in the microhardness was explained as the effect of combination of better densification and reduced grain size [187].

Gunduz et al. obtained a material by mixing of small amounts of ZnO with bovine HA powder. They sintered the samples at various temperatures from 1000°C to 1300°C [216]. Vickers microhardness test was applied to the samples. According to the results, as the sintering temperature increased, Vickers microhardness values increased. The samples sintered at 1300°C had 5 times higher microhardness values than the samples sintered at 1000°C. The effect of ZnO was investigated and found that ZnO increased the microhardness of the samples [216]. However, the amount of ZnO was also important. The addition of ZnO with the amounts of 2.5% and 10% by weight did not give satisfactory results as 5% by wt. ZnO added samples gave [216]. In another study, HA doped with MgO and ZnO was synthesized by sol-gel technique [155]. For mechanical analysis, the samples were sintered at 1300°C for 6h. Vickers hardness test results showed that ZnO addition with a percentage of 1 by weight increased the Vickers hardness of the samples when compared with pure HA [155]. However, MgO doped samples gave the highest

microhardness values [155]. The improvement was calculated as 6% for ZnO addition and 20% for MgO addition [155].

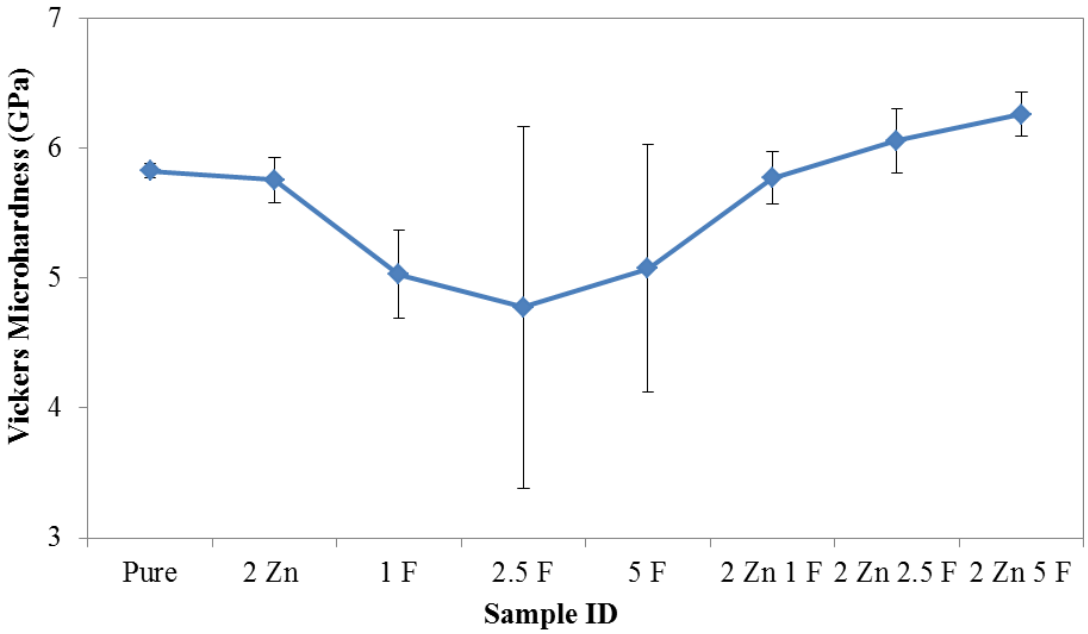


**Figure 3.33.** Vickers microhardness of pure HA, 2 Zn, 1 F, 2.5 F, 5 F, 2 Zn 1 F, 2 Zn 2.5 F, 2 Zn 5 F.

$Cl^-$ addition decreased the microhardness values. However, as the $Cl^-$ amount increased, microhardness values increased. The highest microhardness value was obtained for 5 Cl among $Cl^-$ doped samples. 2 mol.% $Zn^{2+}$ incorporation to the $Cl^-$ doped samples results in further decrease in microhardness values. 2 Zn 2.5 Cl has the lowest microhardness value. $Zn^{2+}$ incorporation supresses the increase in microhardness. All samples that include $Zn^{2+}$ and $Cl^-$ have lower microhardness values than pure HA and 2 Zn (Figure 3.34). This was due to the decrease of Ca/P ratio in Zn doped samples [193]. $Ca^{2+}$ ions increased the hardness of the samples. The increase in microhardness of 5 Cl stemmed from the additional CaO phase in the structure.

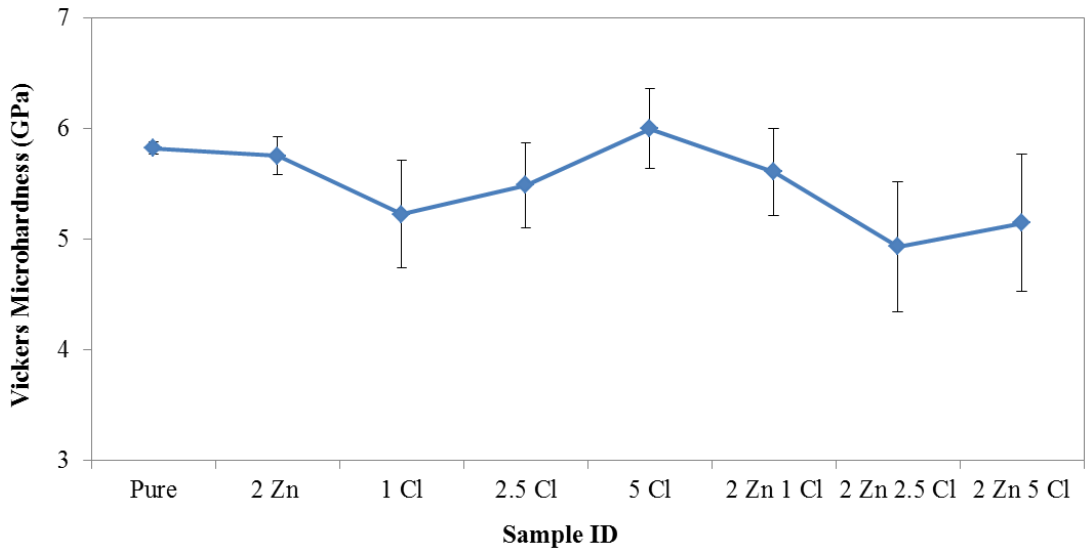


**Figure 3.34.** Vickers microhardness of pure HA, 2 Zn, 1 Cl, 2.5 Cl, 5 Cl, 2 Zn 1 Cl, 2 Zn 2.5 Cl, 2 Zn 5 Cl.

In a study, pure HA, chlorapatite and three different compositions of $Cl^-$ substituted HA were synthesized by precipitation method [193]. The samples were sintered at 1200°C for 2h. Vickers microhardness of the samples showed that, HA and 2.5 mol.% $Cl^-$ substituted HA gave the highest results. Other $Cl^-$ substituted samples had lower results due to the decrease in Ca/P ratio in these samples. Calcium deficiency resulted in decrease in mechanical properties. However, although chlorapatite had the Ca/P ratio of 1.67, it gave lower values than $Cl^-$ substituted sample which had the Ca/P ratio of 1.62 in terms of microhardness. Unlike very similar element $F^-$ which substitution increased the stability of HA, $Cl^-$ substitution decreased the stability. However, 2.5 mol.% $Cl^-$ addition did not have a significant effect on microhardness results [193].

### 3.2.2. Fracture Toughness

Fracture toughness of the samples is also calculated as seen in Table 3.10.

**Table 3.10.** Fracture toughness of the samples sintered at 1100 °C for 1h.

| Group Name | Compound Name | Fracture Toughness ($MPa \cdot m^{1/2}$) |
|---|---|---|
| Group 1 | Pure | 1.121 ± 0.165 |
| | 2 Zn | 1.054 ± 0.098 |
| Group 2 | 1 F | 1.247 ± 0.282 |
| | 2.5 F | 1.082 ± 0.129 |
| | 5 F | 1.110 ± 0.364 |
| Group 3 | 2 Zn 1 F | 1.147 ± 0.050 |
| | 2 Zn 2.5 F | 0.998 ± 0.007 |
| | 2 Zn 5 F | 1.233 ± 0.159 |
| Group 4 | 1 Cl | 1.114 ± 0.183 |
| | 2.5 Cl | 1.095 ± 0.023 |
| | 5 Cl | 1.090 ± 0.197 |
| Group 5 | 2 Zn 1 Cl | 1.099 ± 0.146 |
| | 2 Zn 2.5 Cl | 1.227 ± 0.265 |
| | 2 Zn 5 Cl | 1.077± 0.114 |

According to results $Zn^{2+}$ addition decreased the fracture toughness of pure HA. Doping of $F^-$ increased the fracture toughness. However, as $F^-$ amount increases the samples became more brittle and fracture toughness values decreased up to 2.5 mol.% $F^-$ doping. The samples with doped of 2.5 mol.% $F^-$ showed the lowest value which was an indicator of brittleness of the material. However, as the amount of $F^-$ increased further, the fracture toughness of the samples also increased.

In a study HA/yttria-doped alumina composite and HA/yttria-doped zirconia composites and the effect of fluorapatite that were added to HA with a percentage of 80 were investigated [139]. According to the results, after sintering the composites at 1400°C for 3h, the samples including $F^-$ had a significant decrease in porosity. Fracture toughness of the samples were also measured and calculated. It was found that, $F^-$ addition caused increase in the fracture toughness. The reason of this increase was explained as the decrease in porosity of fluoridated samples [139].

In another study HA and 50% $F^-$ substituted HA was synthesized by precipitation method and sinetered at 1250°C for 1h [190]. Fracture toughness data showed that, $F^-$ substitution increased the fracture toughness of the samples significantly, hence decreased the brittleness index [190].

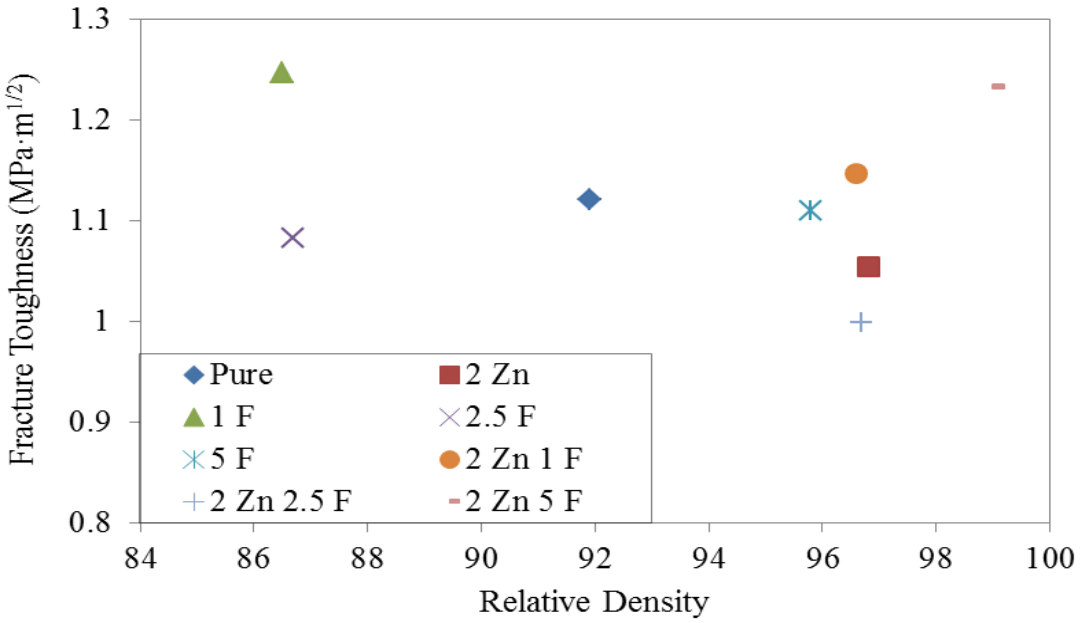


**Figure 3.35.** Fracture toughness and relative density relation of pure HA, 2 Zn, 1 F, 2.5 F, 5 F, 2 Zn 1 F, 2 Zn 2.5 F, 2 Zn 5 F

$Zn^{2+}$ addition to the $F^-$ doped samples increases the fracture toughness. Therefore, by $Zn^{2+}$ and $F^-$ addition the material becomes resistant to fractures when compared to pure HA and 2 Zn although $Zn^{2+}$ decreased the fracture toughness of pure HA alone. Like in $F^-$ doped samples, 2 Zn 1 F had the highest fracture toughness value among $Zn^{2+}$ and $F^-$ doped samples. Significant decrease was seen for 2 Zn 2.5 F. As the amount of $F^-$ increased, fracture toughness also increased.

$Cl^-$ effect is also investigated. It is observed that $Cl^-$ addition makes the material more brittle. When the $Cl^-$ amount increases, fracture toughness decreases which means increase in brittleness. $Zn^{2+}$ addition decreased the fracture toughness values

with a little amount. However, increasing the $Cl^-$ amount to 2.5 mol.% results in a significant increase in fracture toughness.

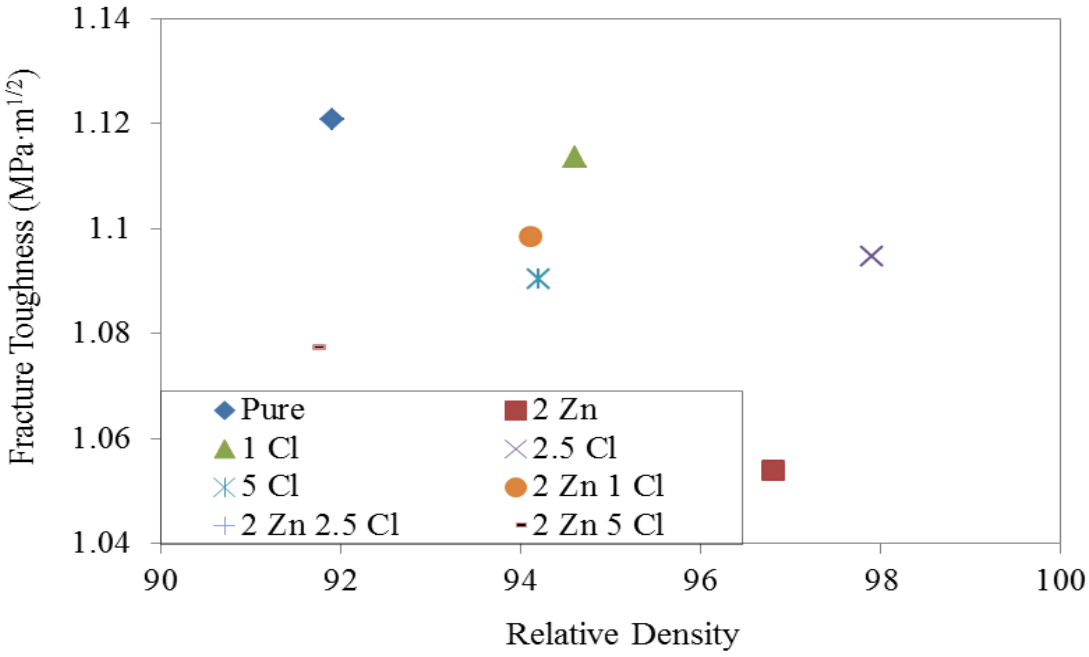


**Figure 3.36.** Fracture toughness and relative density relation of pure HA, 2 Zn, 1 Cl, 2.5 Cl, 5 Cl, 2 Zn 1 Cl, 2 Zn 2.5 Cl, 2 Zn 5 Cl.

The relative density and fracture toughness are also related properties. In Figures 3.35 and 3.36, the relation between fracture toughness and relative density can be investigated. In Figure 3.35, the fracture toughness shows an increasing trend as relative density increases. However, 1 F has the highest fracture toughness although it has the lowest relative density.

Figure 3.36 also shows the increasing trend between relative density and fracture toughness.

The calculated fracture toughness values were between 0.998 and 1.247. The highest value correspond to 1 F whereas the lowest one corresponds to 2 Zn 2.5 F.

### 3.3. Biological Characterizations

#### 3.3.1. Alamar Blue™ Assay

Alamar Blue™ is the indicator of cell proliferation. It has a dark blue non-fluorescent color and when reduced with cell metabolites it gains a fluorescent red color.

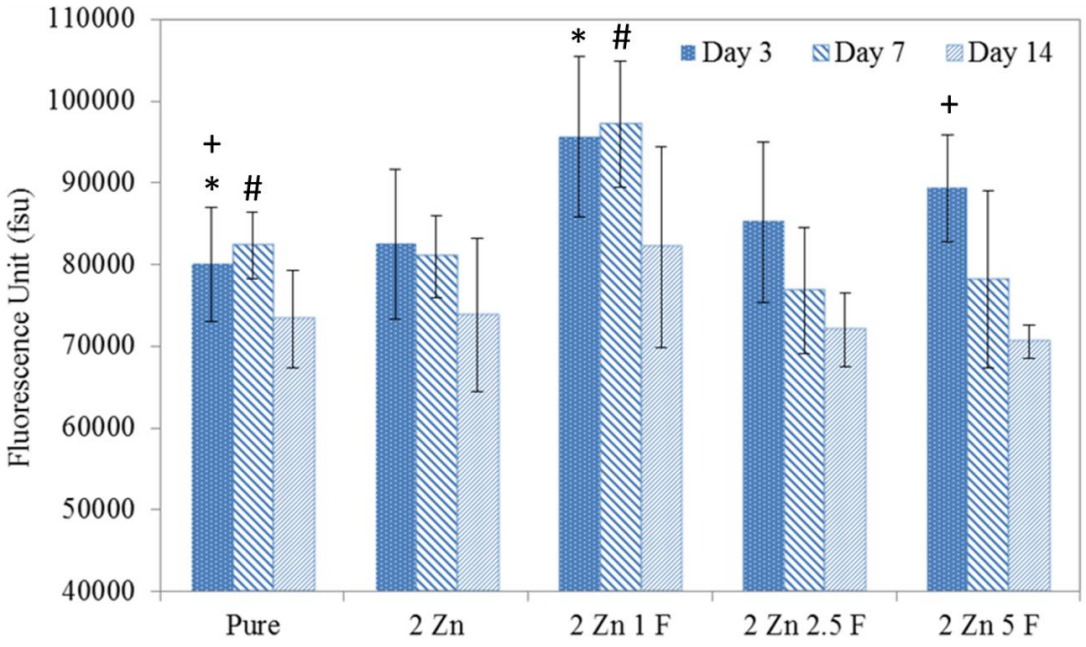


**Figure 3.37.** Cell proliferation on HA and doped HA discs determined by Alamar Blue™ Assay. (* and + denote $p<0.1$, # denotes $p<0.05$ for independent student t test by using SPSS-15.0 Software, USA).

Alamar Blue™ reagent does not interfere with any of metabolic reactions which makes this reagent non-cytotoxic. In Figure 3.37, results for cell proliferation on discs with different compositions are presented.

On all $Zn^{2+}$ doped samples, higher cell proliferation than that of pure HA was observed at day 3 which was in agreement with the work of Ramaswamy et al. [217]. The group reported that $Zn^{2+}$ addition increased the cell proliferation when compared with Ca-Si based ceramics without $Zn^{2+}$. At day 7, the viability of cells

on pure HA, 2 Zn and 2 Zn 1 F group discs remained the same as on day 3. At day 7, a decrease in the cell viability was observed. This could be due to reaching confluency on these discs and changing state from proliferation to differentiation state as reported by other studies [218, 219]. Further increase in $F^-$ content decreased the metabolic activity of the cells on these discs and an evident time dependent decrease in the viability of cells was observed for these groups. In literature, there are several reports stating that $Zn^{2+}$ ion addition increased the proliferation of the cells. However, in the study of Ito et al., it was stated that when zinc content of HA/TCP composites was between 0.6 and 1.2 wt.% an increase in the proliferation of MC3T3-E1 was observed. Otherwise, for zinc content higher that 1.2 wt.%, zinc release from the materials resulted in cytotoxic effects. The group observed the highest cell proliferation in the samples with 1.2 wt.% $Zn^{2+}$ [133]. The $Zn^{2+}$ amount used in the samples was also in this range in the current study. When the viability of the cells on doped discs was compared with that of pure HA at different time periods, no significant differences were observed showing that dopants did not cause any cytotoxic effect. It can be suggested that all groups were biocompatible. The time dependent decrease in the viability of the cells could be explained by the either probable cell death or decrease in cell viability due to reaching high cell density on discs or cells being captured in mineralized matrix that they produced.

In the current study, it was observed that $F^-$ addition to HA also resulted with an increase in the proliferation of cells (Figure 3.37). $F^-$ effect on cell proliferation and attachment were reported in several studies [220-223]. The investigations showed that doping of HA with $F^-$ can improve the biological properties (i.e. cell attachment, proliferation, functionality) of HA if the level of doping was done at optimum levels. This optimum amount for $F^-$ addition to HA was reported as 0.4 mol $F^-$/ 1 mol HA in literature [222, 223]. It was also shown that $OH^-$ ions had binding sites for cell attachment and $F^-$ ions in culture medium stimulated cell attachment [224]. The highest proliferation among $F^-$ doped discs was obtained for 2 Zn 1 F at day 3 in the current study. However, a time dependent increase in the

proliferation of cells on discs was not observed on all discs. In a study by Wang et al., the proliferation of MG63 cells was investigated on fluoridated HA. The group observed that the cells proliferated up to day 5. However, at day 7, the rate of proliferation started to decrease. Among fluoridated samples, 50 mol.% and 67 mol.% $F^-$ added samples highest cell proliferation was observed. However, the samples without $F^-$, 33 mol.% $F^-$ added HA and fluorapatite gave similar results in terms of cell proliferation [221]. Another study, however, reported that $F^-$ ion addition did not affect the cell proliferation and attachment significantly, but affected the gene expession specifically, ALP activity and osteocalcin related genes [220].

### 3.3.2. Alkaline Phosphatase Activity Assay

In Figure 3.38, alkaline phosphatase (ALP) activities of the cells seeded on pure HA and doped HA discs are presented. It was observed that at day 7 ALP activities of cells were higher than those on day 15 for all groups except 2 Zn 2.5 F group. This might indicate that the cells on these discs switched to the next differentiation state in agreement with the findings of Kim et al. and Wang et al. with the down regulation of the ALP gene [220, 221].

It was also observed that 2 mol% $Zn^{2+}$ addition alone increased the ALP activity significantly both at days 7 and which was also in agreement with literature [217, 225]. Ramaswamy et al. observed a time dependent increase in ALP activity of osteoblasts seeded on Ca-Si based materials [217]. In another study, $Zn^{2+}$ effect on β-TCP/HA composities in terms of ALP activity of bone marrow cells was investigated for two weeks [225]. According to their results, 0-1.26 wt.% of $Zn^{2+}$ addition increased the ALP activiy of the bone marrow cells. It was reported that 1.26 wt.% of $Zn^{2+}$ added samples showed 3 or 4 fold higher ALP activity results when compared with samples without $Zn^{2+}$ [225]. Roughly a 1.5 and 2-fold increases were observed for only 2 Zn and 2 Zn 1 F groups, respectively in the current study (Figure 3.38). Higher ALP activity observed for these groups were also in agreement with the viability results (Figure 3.37). Webster et. al. synthesized

$Zn^{2+}$ doped HA by precipitation method and sintered the samples at 1100°C for 1 h. They observed that human osteoblast cells had higher ALP activity on $Zn^{2+}$ doped samples than pure HA at days 7 and 21. They also concluded that the increase in ALP activity was dependent on the grain size of the samples. Smaller grain size resulted in better attachment of the cells hence higher ALP activity [137, 163, 165, 188].

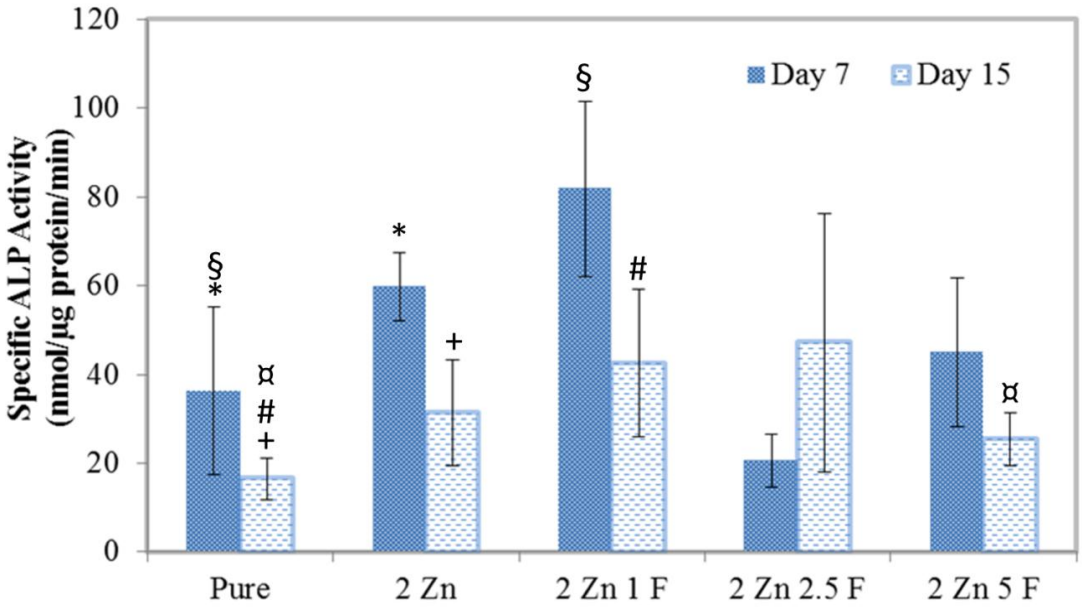


**Figure 3.38.** ALP Activity results at day 7 and 15. (*, + and ¤ denote $p<0.1$, # and § denote $p<0.05$ for independent student t test by using SPSS-15.0 Software, USA).

In the study of Webster et al., the grain sizes of the samples undoped HA, 2 mol% $Zn^{2+}$ doped HA and 7 mol% $Y^{3+}$ doped HA were found as 0.56 µm, 0.32 µm and 0.27 µm, respectively [137]. The cell density and the calcium adsorption on these samples increased as the grain sizes decreased [165]. In the current study, the highest grain size corresponded to the pure HA with the value 0.191 µm and all $Zn^{2+}$ doped samples had lower grain sizes (i.e., 0.183 µm for 2 Zn, 0.176 for 2 Zn 1 F, 0.166 for 2 Zn 2.5 F and 0.188 for 2 Zn 5 F) than that of pure HA. Moreover, ALP acitivity of the $Zn^{2+}$ doped samples had higher results than pure HA except 2

Zn 2.5 F. 2 Zn 2.5 F had the lowest grain size and ALP activity among the samples. It was also reported that grain sizes smaller than a certain given limit may affect the ALP activity negatively [218]. In the current study this limit was 0.176 μm.

The highest ALP activity was observed for 2 Zn 1 F group in this study. However, further increase in $F^-$ content in the samples decreased the ALP activity when compared with the groups at the same time period. Toker et al. found that $F^-$ addition to HA higher than 2.5 mol.% resulted in decrease in ALP activity at day 7 [188]. However, an increase was seen at day 14. The increase at day 14 was lower than the increase in 1 mol.% $F^-$ added sample [188]. The current study was in agreement with the study of Toker et al. The samples with 5 mol.% $F^-$ content showed a decrease in ALP activity of the cells both at day 7 and day 15.

### 3.3.3. SEM Examinations for Cell Morphologies

Figures 3.39 and 3.40 represent the morphologies of cells on discs after 1 and 15 days of incubations. SEM images showed that cells seeded on 2 Zn and 2 Zn 1 F samples spreaded on discs extensively at day 1, which is an indicator of good cell attachment. On pure HA and 2 Zn 2.5 F discs, cells were about 10 μm and cuboidal whereas on 2 Zn 5 F, cells were about 20 μm and had dendritic shapes. However, on 2 Zn and 2 Zn 1 F discs, it was observed that the cell diameters reached to about 50 μm and they also had dendritic shapes.

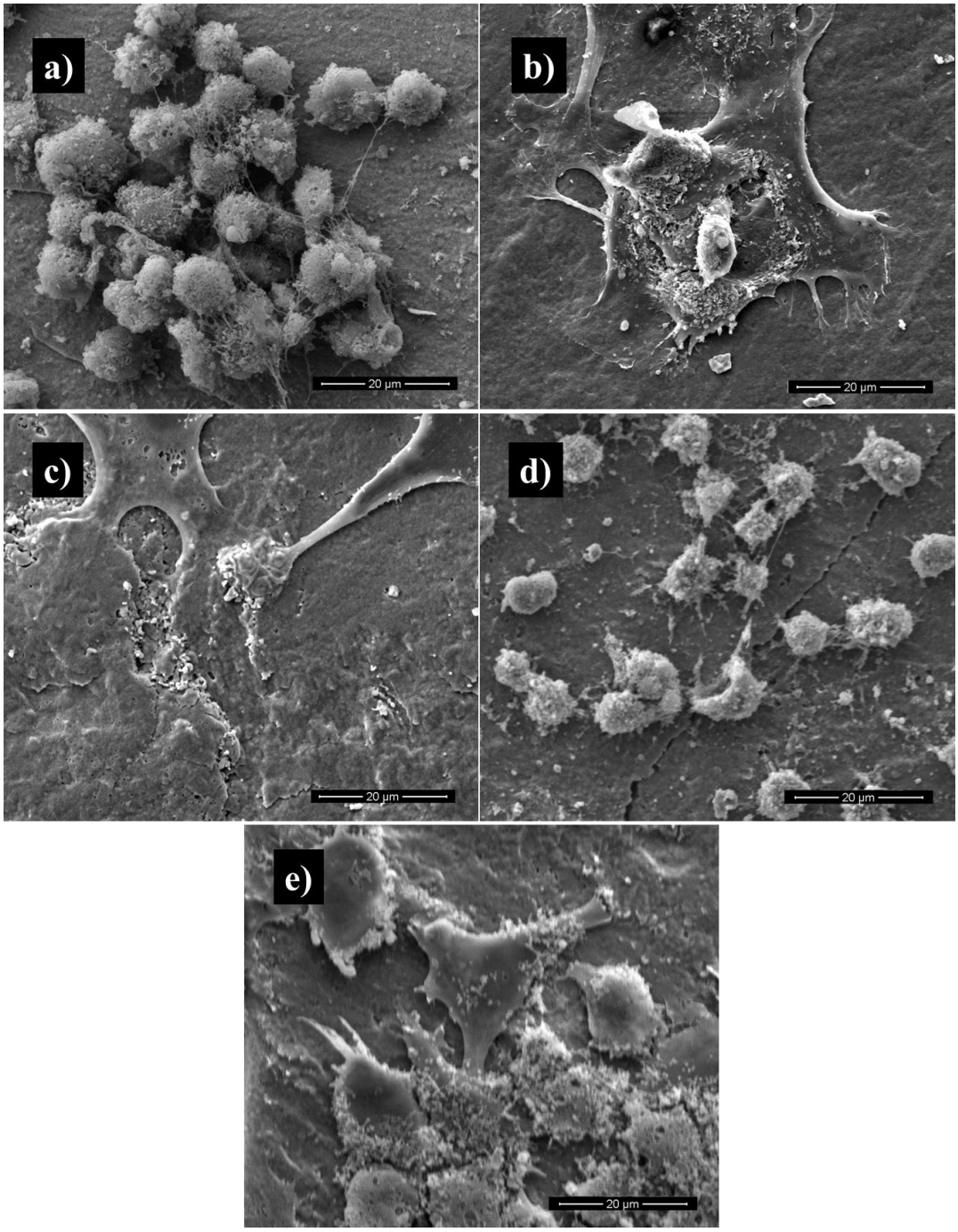


**Figure 3.39.** SEM images of a) pure HA; b) 2 Zn; c) 2 Zn 1 F; d) 2 Zn 2.5 F; e) 2 Zn 5 F after 24h.

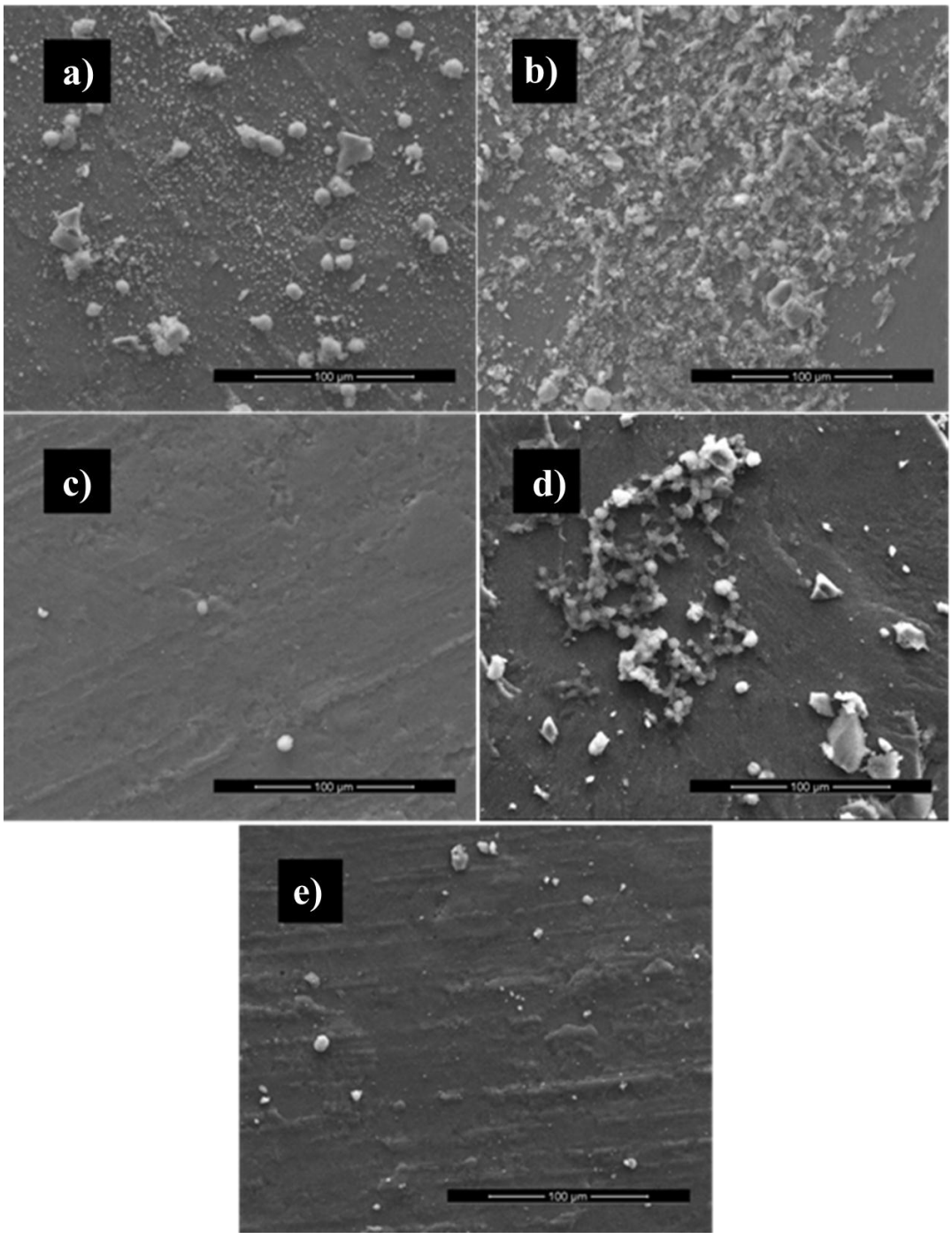


**Figure 3.40.** SEM images of a) pure HA; b) 2 Zn; c) 2 Zn 1 F; d) 2 Zn 2.5 F; e) 2 Zn 5 F after 15 days.

The effect of $Zn^{2+}$ addition on cell morphologies of different cell types were studied by different groups [185, 226]. In the study by Xue et al., it was observed that OPC1 cells on TCP samples without $Zn^{2+}$ had few filopodium. Few filapodium was the indicator of poor cell attachment. By $Zn^{2+}$ addition, OPC1 cells gained three dimensional and cuboidal morphology. Moreover, filopodium started to increase by $Zn^{2+}$ addition [185]. In Figure 3.39, Saos-2 cells seeded on pure HA discs had few filapodium. Moreover, cells seeded on the sample 2 Zn 2.5 F had few filapodium which means poor cell attachment but at the same time gained cuboidal shape. The cell morphologies observed for other $Zn^{2+}$ included samples supported the study of Xue et al. [185]. Similarly, in a study by Miao et al., SEM observations showed that human osteoblast-like MG63 cells had dendritic shapes and a diameter of 50 μm on $Zn^{2+}$ doped samples. The group observed spherical cell bodies on the samples without $Zn^{2+}$ with SEM [226].

In the current study, cell morphology was strongly affected by $Zn^{2+}$ addition. However, $F^-$ addition had no significant effect on cell morphologies as mentioned in the study of Wang et al. [221]. In this study, the effect of $F^-$ addition on the morphology of osteoblast-like MG63 cells was investigated. No change in cell morphology was detected between fluoridated samples. It was reported that cells spreaded onto surface of fluoridated samples with their filopodium and lamellipodium which was the indicator of good cell viability.

In Figure 3.40, some apatite-like clusters are seen on the samples. However, no cells were found at the end of 15 days. It is thought that cells died or detached from the discs during sample preparation for SEM analysis. In accordance with the ALP results, few apatite-like depositions were observed on 2 Zn 5 F discs. On the other hand, although ALP activity of the cells on 2 Zn 1 F and 2 Zn 2.5 F discs had higher values than that of pure HA and 2 Zn, very few depositions were seen on 2 Zn 1 F. Moreover, 2 Zn had more apatite-like formations than 2 Zn 2.5 F.

### 3.3.4. Dissolution Test

#### 3.3.4.1. pH Measurement Results

Stimulated body fluid (SBF) is a solution that has the same ionic concentrations with human extracellular fluid [227] and it is a metastable solution which has $Ca^{2+}$ and $PO_4^{3-}$ ions are supersaturated with respect to apatite [228].

Table 3.11 represents the ion concentrations of blood plasma and SBF. The pH of SBF should be adjusted to 7.25 at 36.5 °C. However, if the material tested had low apatite forming ability, the pH should be 7.40 [227]. In the current study, the pH of the SBF was chosen 7.25 due to the high apatite forming ability of HA. The samples were kept at 36.5°C both in the water bath and incubator.

Dissolution and reprecipitation are two reactions in equilibrium. Figures 3.41 and 3.42 show ΔpH values of $Zn^{2+}$ and $F^-$ doped samples incubated in SBF in a shaking waterbath and in incubator, respectively. It was observed that the pH of the solutions increased with time. In Figure 3.41, a significant increase was seen between days 3 and 7. However, the pH changed slightly between days 7 and 15. This was due to the fact that the solution reached the equilibrium of dissolution and reprecipitation of the ions. The increase in pH is an indicator of high dissolution [229-232]. Increase in pH observed between days 3 and 7 could be the result of high dissolution. However, between days 7 and 15, the pH change was decreased significantly which may be interpreted as the saturation of dissolved ions. In literature, it was reported that reprecipitation stage began after the saturation of dissolved ions which was followed by decrease in of $Ca^{2+}$ and $PO_4^{3-}$ ions concentration and a final stage of apatite formation. For TCP, the ion concentrations of $Ca^{2+}$ and $(PO4)^{3-}$ in SBF started to decrease at day 5. Then, the significant pH increase was observed later at day 15 [233]. However, HA was more stable than TCP. In Figure 3.42, no significant increase in pH was observed between days 3 and 7. However, there was a significant increase at day 15. This was due to lack of mechanical stimulator. In water bath, SBF and material interaction increased by mechanical disturbance. However, in samples kept in incubator did not have any stimulator for maximizing the interaction of SBF and the material.

**Table 3.11.** Ion concentrations of blood plasma and SBF [234].

| Ion | Concentration (mol/m$^3$) | |
|---|---|---|
| | **Blood plasma** | **SBF** |
| $Na^+$ | 142.0 | 142.0 |
| $K^+$ | 5.0 | 5.0 |
| $Mg^{2+}$ | 1.5 | 1.5 |
| $Ca^{2+}$ | 2.5 | 2.5 |
| $Cl^-$ | 103.0 | 147.8 |
| $HCO_3^-$ | 7.0 | 4.2 |
| $HPO_4^{2-}$ | 1.0 | 1.0 |
| $SO_4^{2-}$ | 0.5 | 0.5 |

The effect of $Zn^{2+}$ and $F^-$ ions on the rate of dissolution were also investigated.. In Figure 3.41, a decrease in pH of all samples doped with $Zn^{2+}$ and $F^-$ was seen when compared to pure HA at day 3. The pH change observed for 2 Zn 1 F was the most significant in comparison to pure HA at days 3 and 7. In literature, $Zn^{2+}$ addition into carbonated HA, Ca-Si based ceramics, TCP and sol-gel prepared bioactive glasses were investigated in terms of dissolution studies in different solutions such as cell culture medium, acid, tris-HCl buffer and SBF [185, 217, 235, 236].

In most of the studies, $Zn^{2+}$ addition decreased the dissolution rate of the samples and made the material more chemically stable. The decrease in ΔpH in the current study was interpreted as decrease in the dissolution rate. It was reported that the rate of dissolution increased with increasing crystal disorder and decreasing crystal size. $Zn^{2+}$ ion was known to reduce the crystalline disorder [237]. Moreover, it increased the crystal size [238]. In this study, $Zn^{2+}$ addition decreased the fraction of crystalline phases (Table 3.2) (i.e. 0.75 for pure HA and 0.68 for 2 Zn) and

increased the crystal size (Table 3.3) (i.e., 1588.5 $Å^3$ for pure HA and 1589.2 $Å^3$ for 2 Zn).

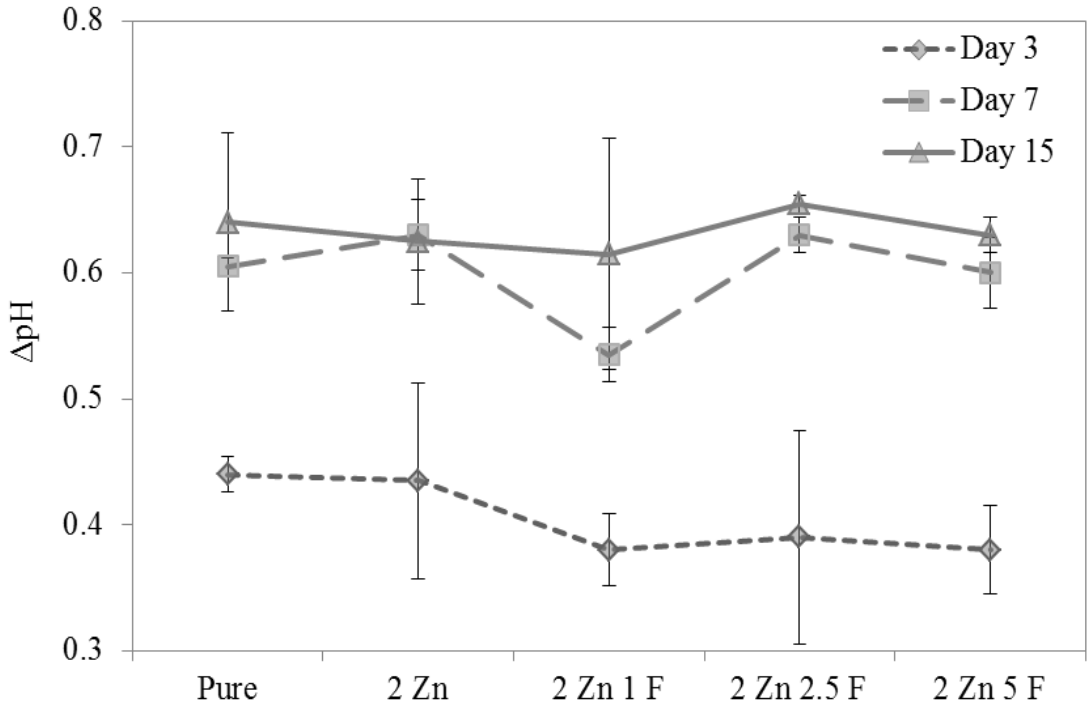


**Figure 3.41.** The ΔpH of the samples in waterbath.

The decreases in ΔpH resulted in decrease in the dissolution rate meaning that $Zn^{2+}$ addition made HA more chemically stable although it had lower fraction of crystalline phases which may be interpreted as low crystallinity. At days 7 and 15, except 2 Zn 1 F samples, pH changes observed for all doped samples were indifferent than that of pure HA. According to a study of Webster et al., $Zn^{2+}$ increased the dissolution of HA. The mass of $Zn^{2+}$ doped HA decreased whereas the mass of HA increased during 21 days. The increase stemmed from the precipitation of apatite on the surface of HA [165]. However, the results in the current study did not support the study of Webster et al. For both pure and doped HA samples, there was a time dependent increase in ΔpH (Figures 3.41 and 3.42) indicating a time dependent dissolution of the samples to differing degrees. After day 7, the dissolution rates started to decrease as a property of the material.

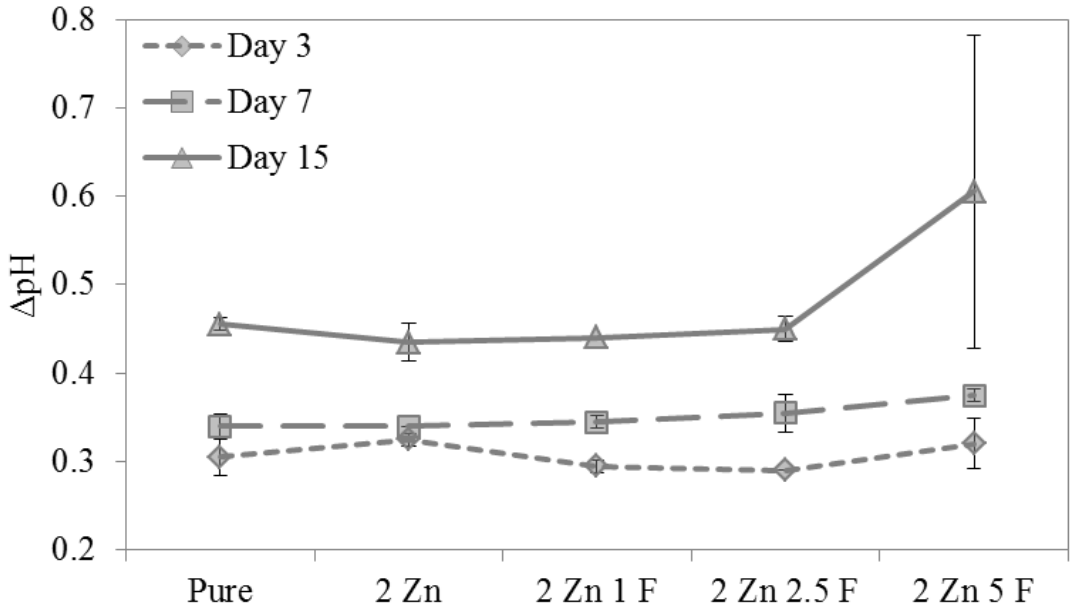


**Figure 3.42.** The ΔpH of the samples in incubator.

The further decrease in pH change in 2 Zn 1 F sample may stem from the $F^-$ effect in the structure. $F^-$ addition increased the fraction of crystallites and made the material more stable [220, 239, 240]. As it was mentioned before, the disorder in the crystal structure increases the solubility significantly. Therefore, $F^-$ ion increased the crystallinity and the stability of the structure. It can be explained by the fact that $F^-$ ion has more stronger hydrogen bond with H atom in $OH^-$ ion than $O^{2-}$ and $H^+$ ions have. H atoms make bond with $O^{2-}$ in different directions along c-axis. It was reported that the stability increased the most when 50 mol.% $F^-$ was doped into HA. The doping percentage higher than 50 mol% resulted in increase in the solubility. Up to that ratio, as $F^-$ amount increased the solubility decreased [221].

In Figure 3.42, no significant change in pH was observed among the samples at days 3, 7 and 15. This was due to lack of the mechanical stimulator. The SBF could not interact these materials efficiently. Therefore, the slight change in pH that was seen in the samples in the water bath (Figure 3.41) was not seen in the samples when they were incubated.

### 3.3.4.2. SEM Observations for $Ca^{2+}$ Deposition

Figures 3.43-3.52 represent the SEM observations of pure and doped HA discs after 7 and 15 days and in SBF.

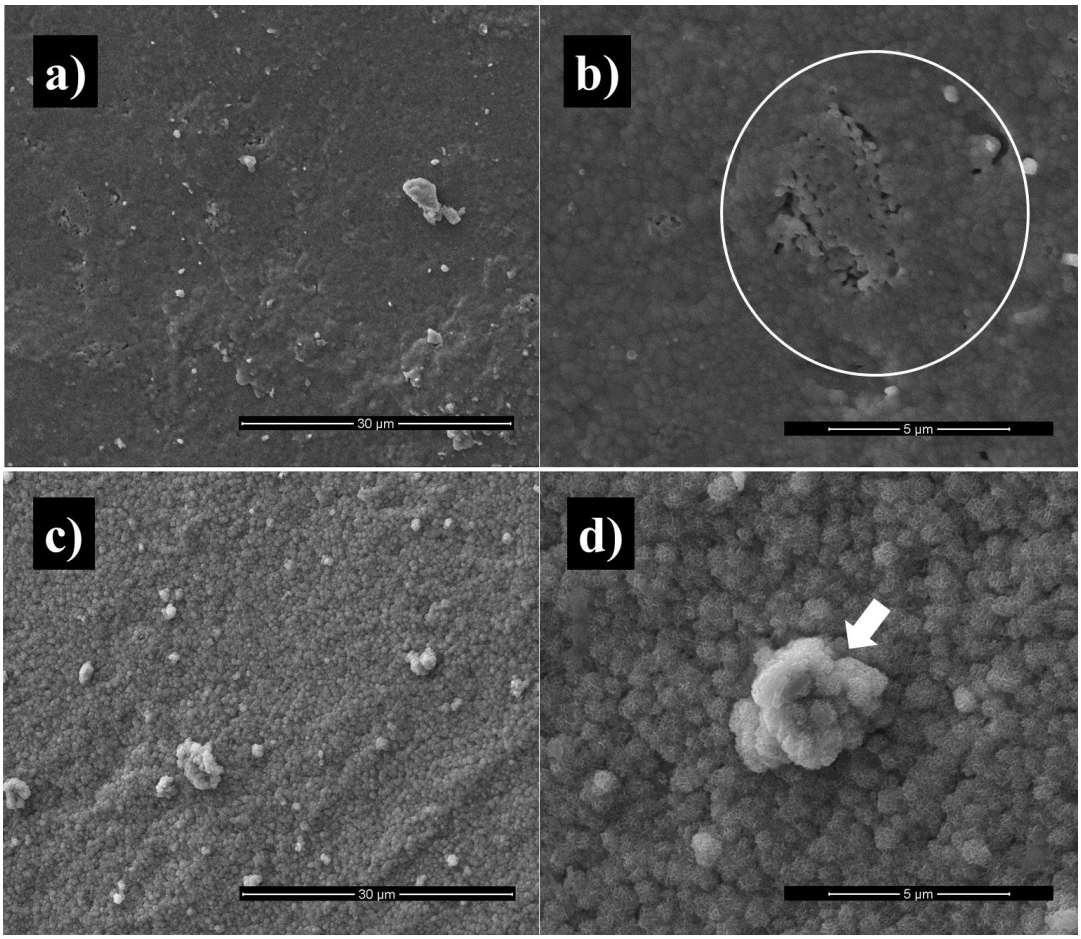


**Figure 3.43.** SEM images of a) pure HA in incubator, 5000X; b) pure HA in incubator, 20000X; c) pure HA in water bath, 5000X; d) pure HA in water bath, 20000X after 7 days in SBF. Circle shows dissolved area on the apatite surface. Arrow head shows the apatite cluster formed on the surface.

In Figures 3.43 and 3.44, the samples in the incubator have similar surface morphologies at days 7 and 15. However, at day 15, the surface was more rough and some apatite particles were seen. The samples in the water bath have more

apatite crsytals when compared with the samples in incubator. Among the samples in water bath, the samples at day 15 have more dissolution pits on the surface which might be due to the dissolution of the samples. The increase in roughness of the surface observed in SEM images are in agreement with the findings in Figures 3.46 and 3.47 in which the pH change increased with a probable higher dissolution rate.

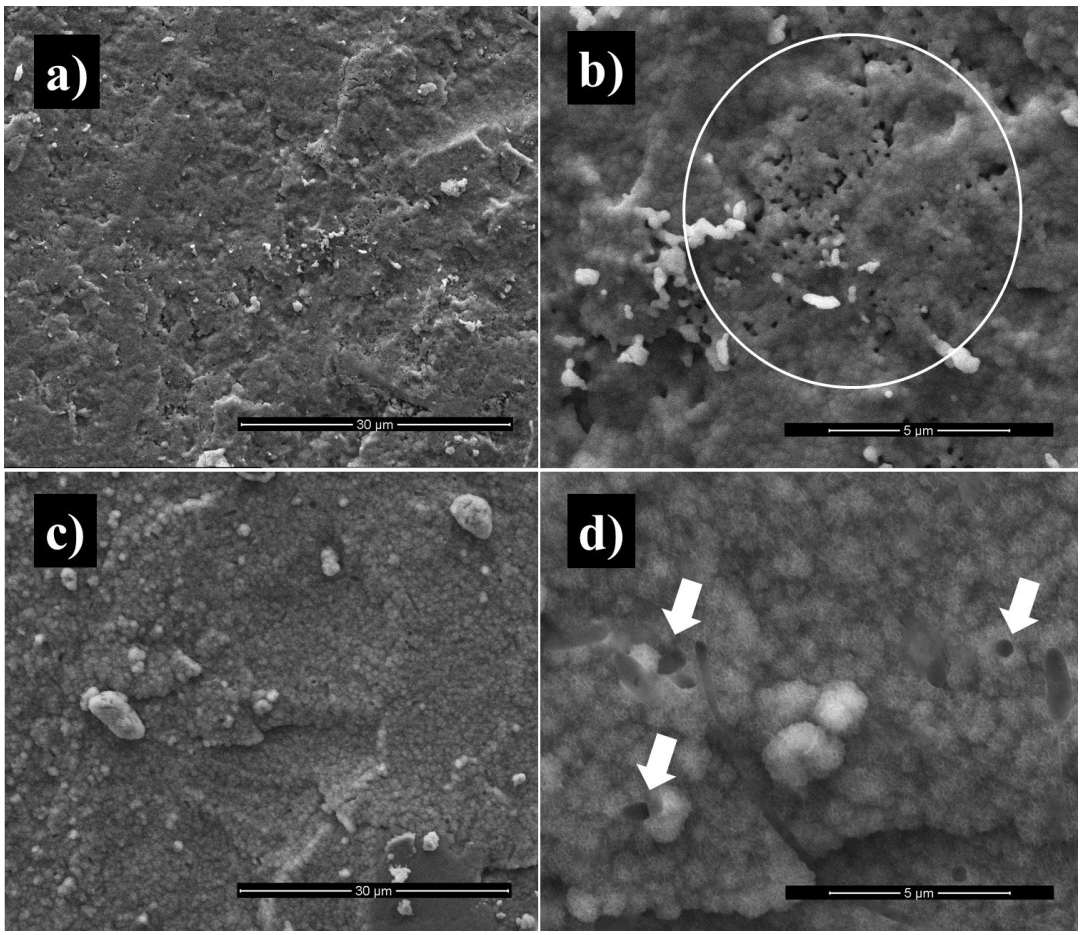


**Figure 3.44** SEM images of a) pure HA placed in incubator, 5000X; b) pure HA in incubator, 20000X; c) pure HA in water bath, 5000X; d) pure HA in water bath, 20000X after 15 days in SBF. Circle shows dissolved area on the apatite surface. Arrow heads show the holes that are formed by dissolution.

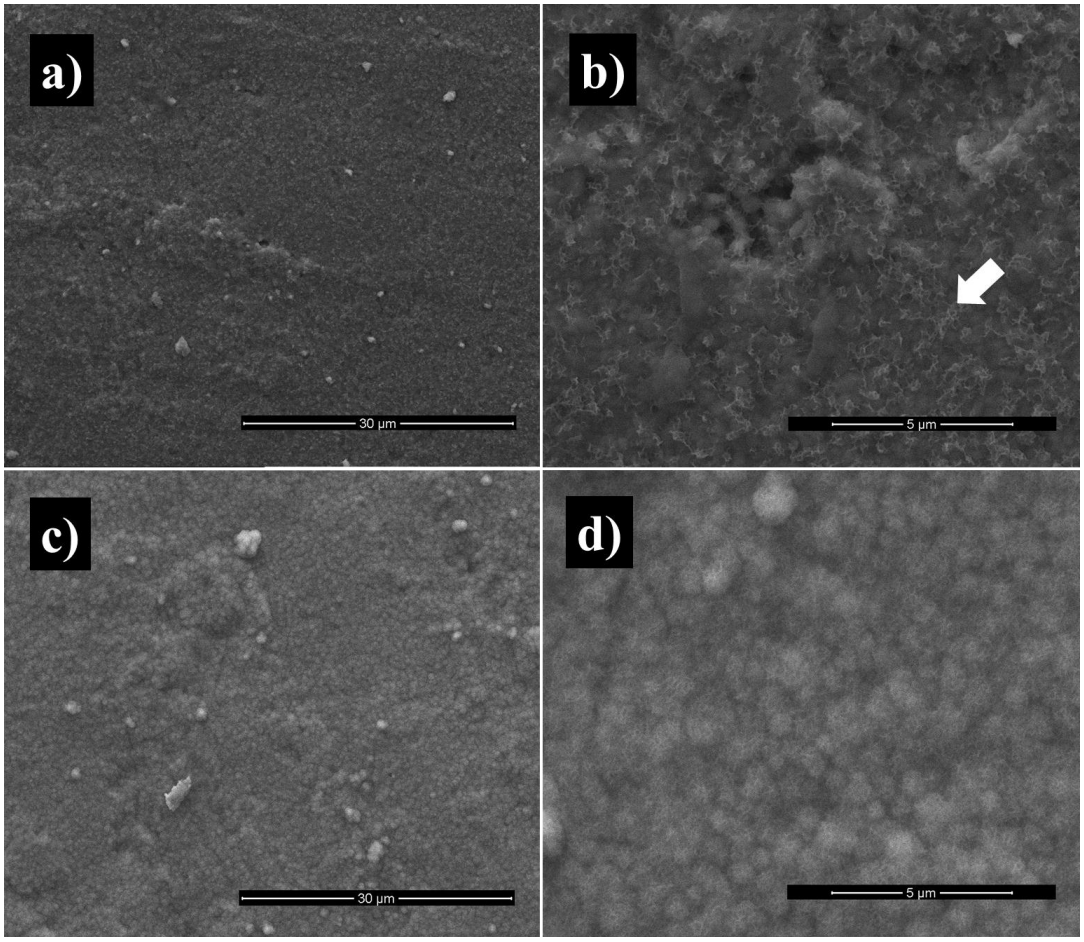


**Figure 3.45.** SEM images of a) 2 Zn in incubator, 5000X; b) 2 Zn in incubator, 20000X; c) 2 Zn in water bath, 5000X; d) 2 Zn in water bath, 20000X after 7 days in SBF. Arrow head shows the apatite crystals formed on the surface.

No significant difference between the samples with the same composition in the incubator and in the water bath was detected (Figures 3.45 and 3.46). The dissolution effect was noticed at the day 15. The samples in the incubator had more dissolution pits than those incubated in the water bath at day 15. However, more apatitic formations were observed on the surface of the samples in the water bath.

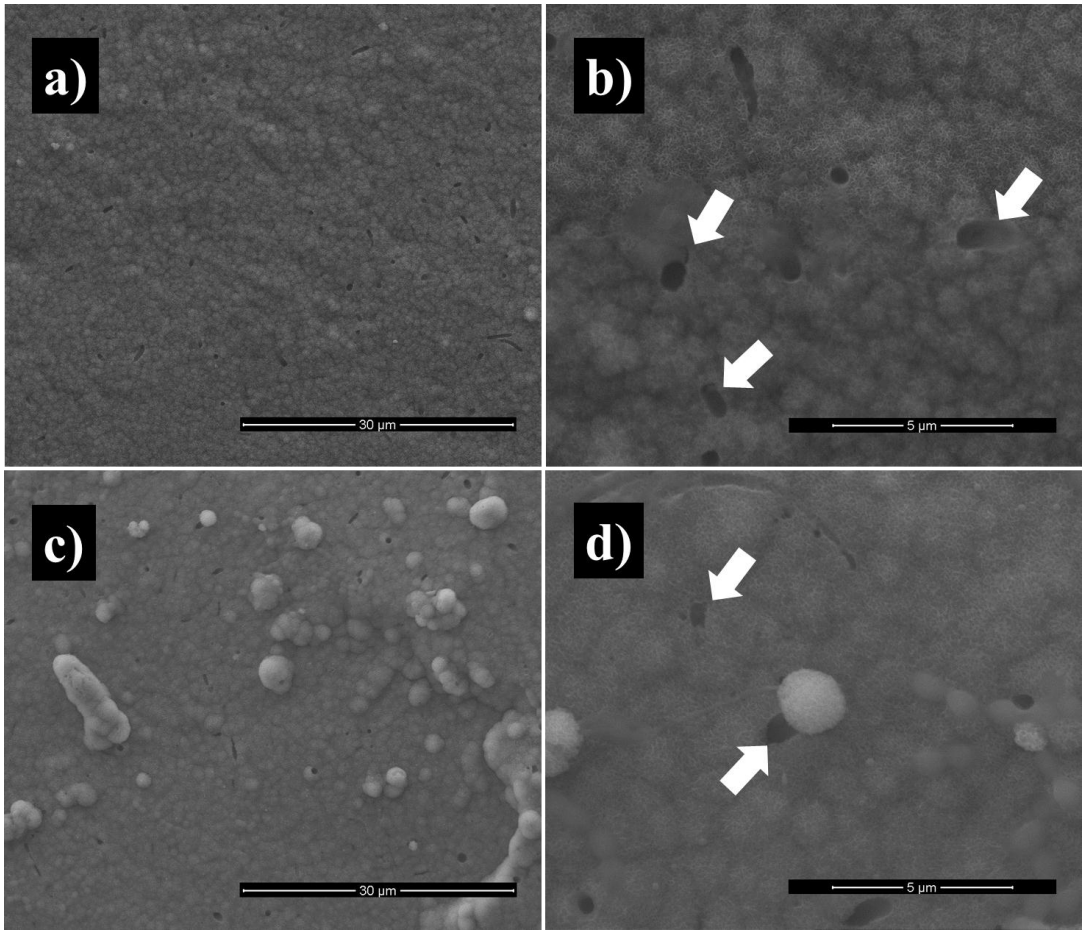


**Figure 3.46.** SEM images of a) 2 Zn in incubator, 5000X; b) 2 Zn in incubator, 20000X; c) 2 Zn in water bath, 5000X; d) 2 Zn in water bath, 20000X after 15 days in SBF. Arrow heads show the holes that were formed by dissolution of the material.

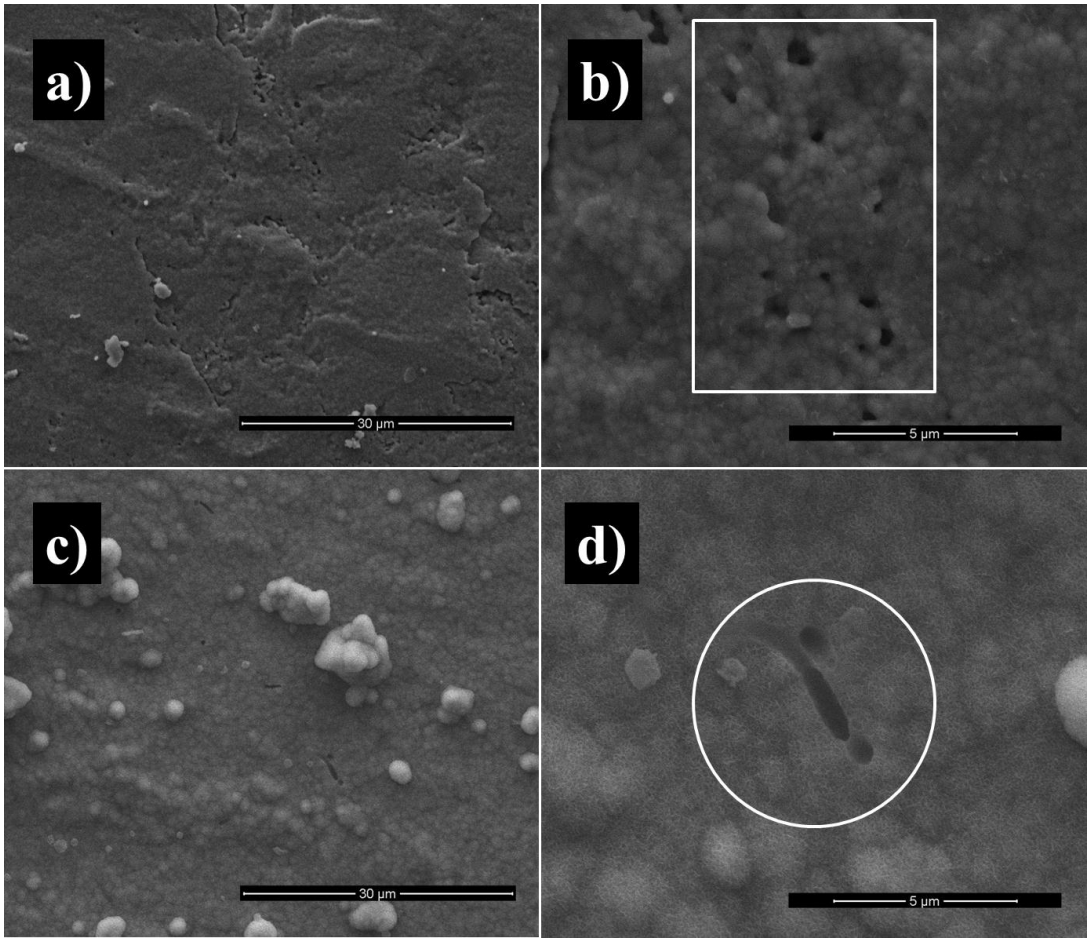


**Figure 3.47.** SEM images of a) 2 Zn 1 F in incubator, 5000X; b) 2 Zn 1 F in incubator, 20000X; c) 2 Zn 1 F in water bath, 5000X; d) 2 Zn 1 F in water bath, 20000X after 7 days in SBF. The rectangle represents the dissolved area on the surface. The circle shows the holes formed by dissolution.

2 Zn 1 F sample gave the lowest decreases in terms of pH changes among the other samples. This means that 2 Zn 1 F sample was the most stable one. Therefore, least dissolution in 2 Zn 1 F samples was expected. The images in the Figures 3.47 and 3.48 are consistent with these results. When the images of pure and 2 Zn were compared with the images of 2 Zn 1 F, it was observed that 2 Zn 1 F had fewer holes on its surface. The water bath effect on the samples appeared with more

apatitic formations on the surface. Moreover, no change was seen between the images of the day 7 and day 15 for the discs with the same composition.

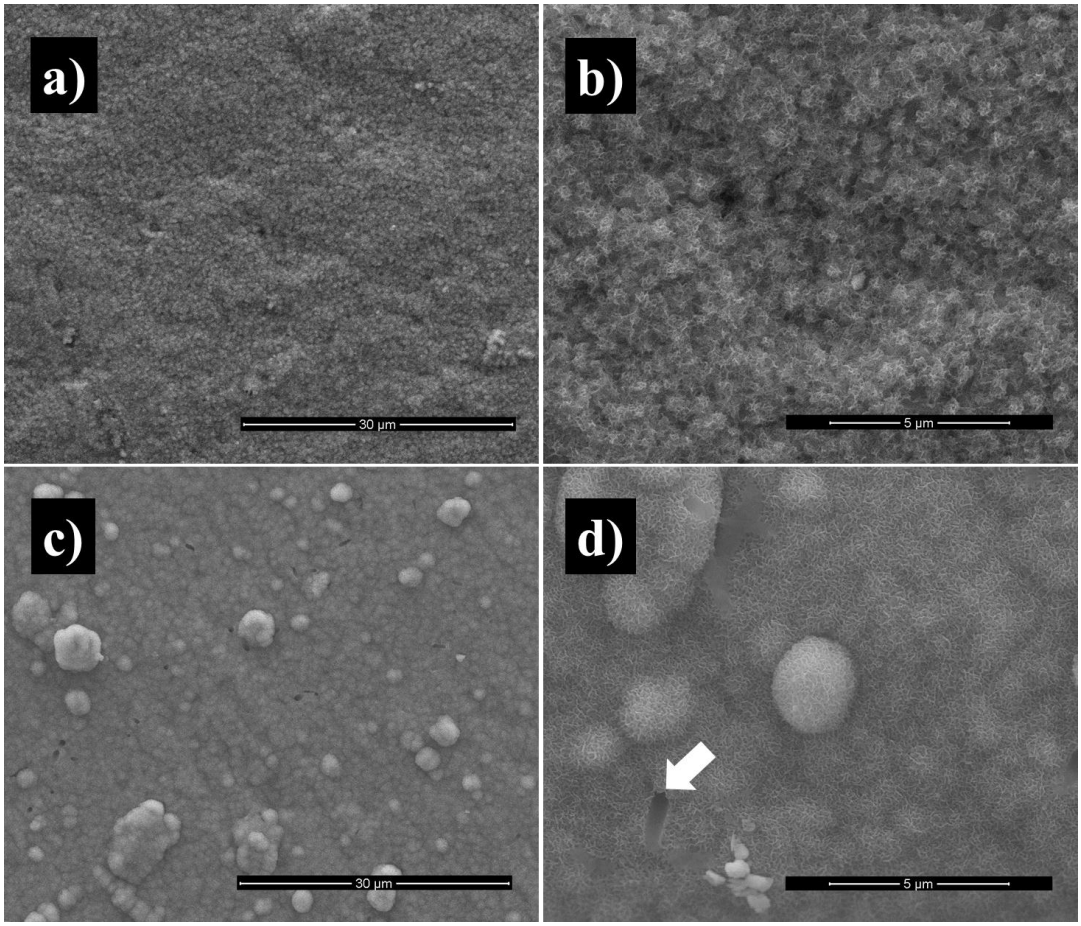


**Figure 3.48.** SEM images of a) 2 Zn 1 F in incubator, 5000X; b) 2 Zn 1 F at in incubator, 20000X; c) 2 Zn 1 F in water bath, 5000X; d) 2 Zn 1 F in water bath, 20000X after 15 days in SBF. Arrow head shows the hole formed by dissloution.

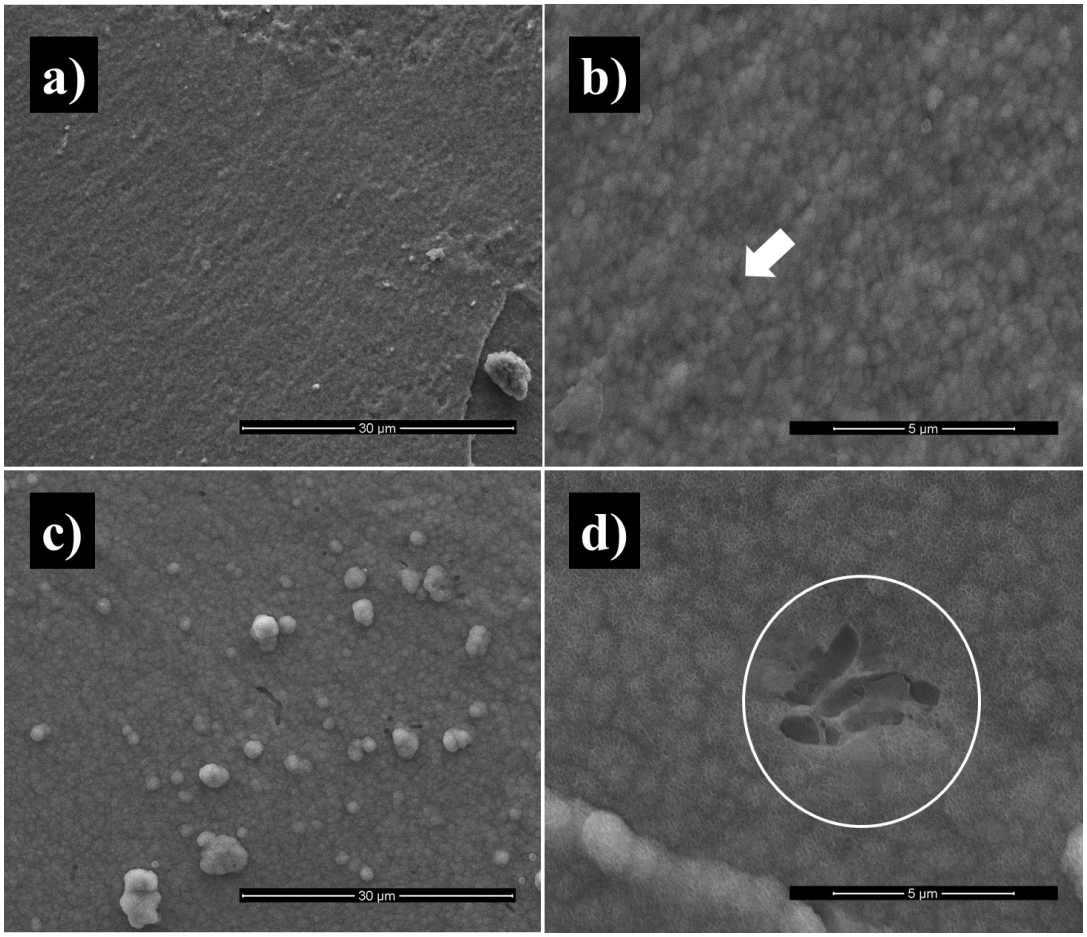


**Figure 3.49.** SEM images of a) 2 Zn 2.5 F in incubator, 5000X; b) 2 Zn 2.5 F in incubator, 20000X; c) 2 Zn 2.5 F in water bath, 5000X; d) 2 Zn 2.5 F in water bath , 20000X after 7 days in SBF. Arrow head shows the hole formed by dissolution. Circle shows dissolved area on the surface.

In Figures 3.46 and 3.47, the change in pH for 2 Zn 2.5 F was higher than that observed for 2 Zn 1 F. Therefore, a high dissolution rate was expected for 2 Zn 2.5 F. In Figures 3.49 and 3.50, the dissolution was clearly seen with dissolution pits. The surface of the sample 2 Zn 2.5 F was very rough and with more holes when compared with pure, 2 Zn and 2 Zn 1 F at day 15. The water bath had no significant effect on 2 Zn 2.5 F sample. However, at day 7, more apatitic formations were observed for the samples incubated in the water bath. For 2 Zn 2.5 F, there was a

significant difference between the surface morphologies of the samples at days 7 and 15. Consistent with the pH change results, more rough surface was seen at day 15 when compared to day 7.

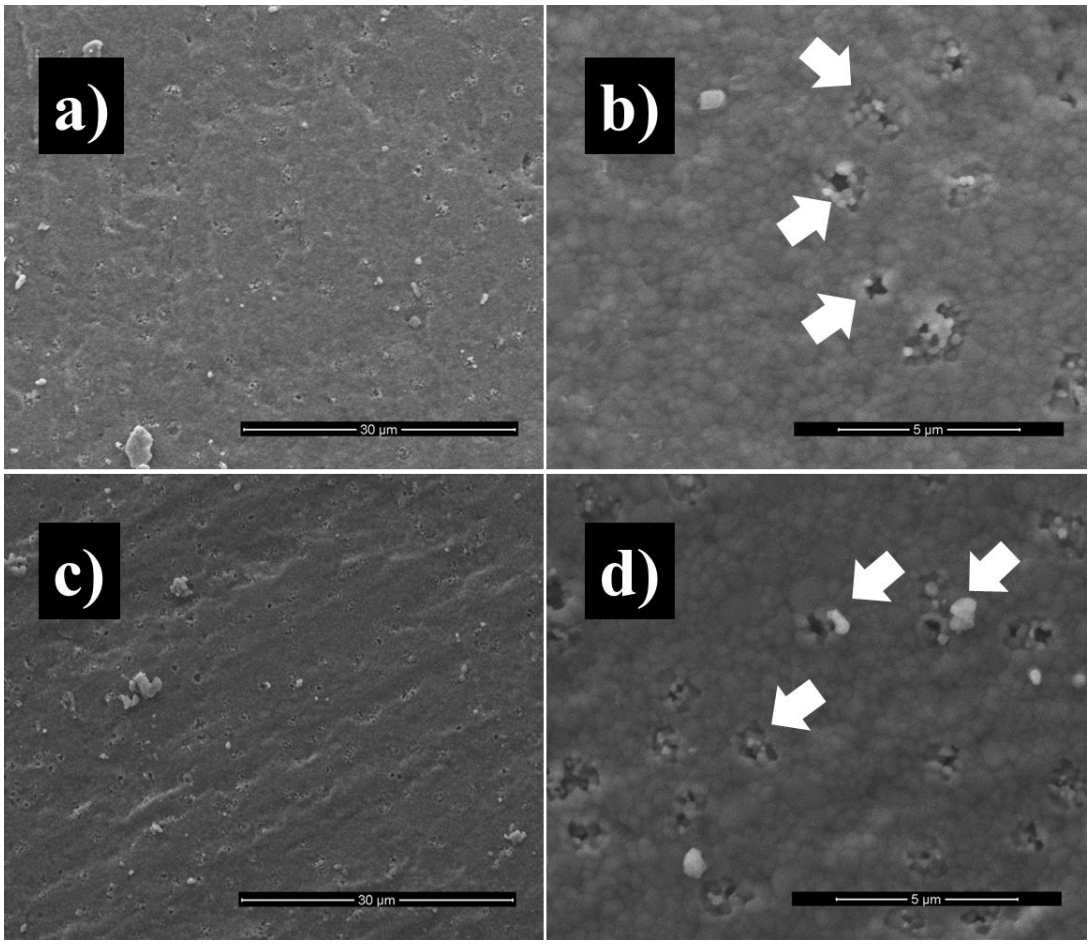


**Figure 3.50.** SEM images of a) 2 Zn 2.5 F in incubator, 5000X; b) 2 Zn 2.5 F in incubator, 20000X; c) 2 Zn 2.5 F in water bath, 5000X; d) 2 Zn 2.5 F in water bath, 20000X after 15 days in SBF. Arrow heads show the dissolution pits on the surface of the material.

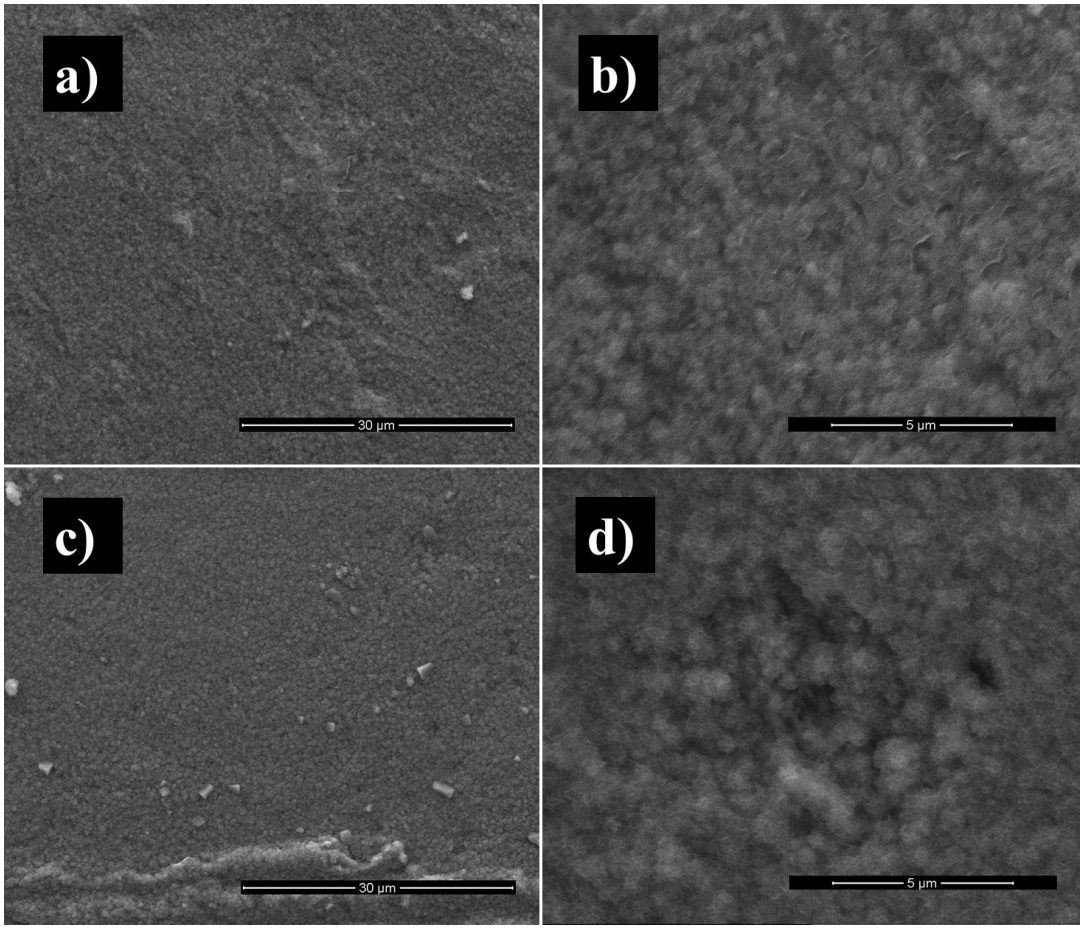


**Figure 3.51.** SEM images of a) 2 Zn 5 F in incubator, 5000X; b) 2 Zn 5 F in incubator, 20000X; c) 2 Zn 5 F in water bath, 5000X; d) 2 Zn 5 F in water bath, at 20000X after 7 days in SBF.

No significant change was observed between the samples in the water bath and in the incubator at day 7 (Figure 3.51). 2 Zn 5 F had less rough surface than that of 2 Zn 2.5 F at day 15 supporting the pH change results. According to Figure 3.46, ΔpH change decreased when $F^-$ mole% in doped samples was increased to 5 mol.% (2 Zn 5 F). However, in the Figure 3.47, a slight increase in the pH change of 2 Zn 5 F was seen for those incubated in the incubator. When the samples in the incubator and in the water bath were compared, more dissolution pits were seen on the surface of the samples in the water bath. Moreover, some apatitic formations

were observed on the samples in the incubator at day 15 when compared with the samples in the incubator at day 7.

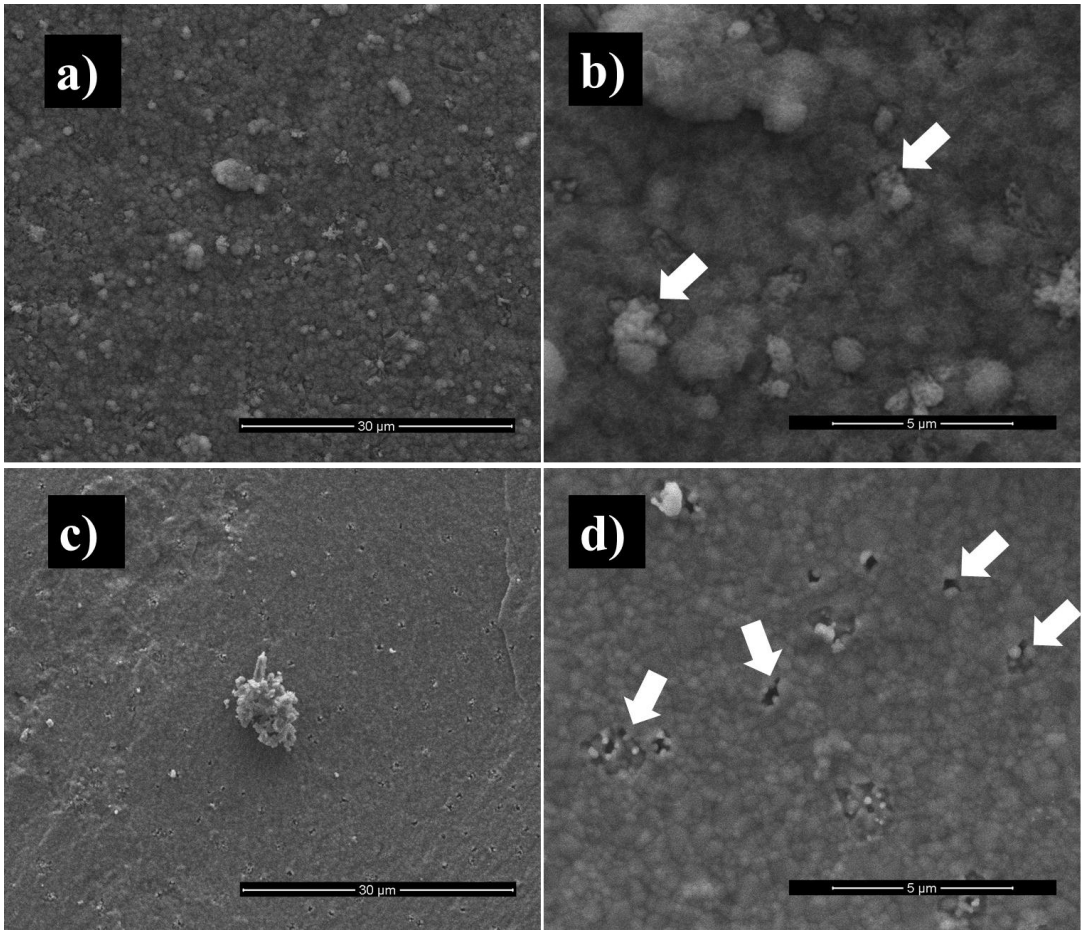


**Figure 3.52.** SEM images of a) 2 Zn 5 F in incubator, 5000X; b) 2 Zn 5 F in incubator, 20000X (Arrow heads show the apatite clusters); c) 2 Zn 5 F in water bath, 5000X; d) 2 Zn 5 F in water bath, 20000X (Arrow heads show the dissolution pits) after 15 days in SBF.

# CHAPTER 4

# CONCLUSION

In this study HA and HA doped with $Zn^{2+}$, $Cl^-$ and $F^-$ ions synthesized by precipitation method. The doping of $Zn^{2+}$ was kept at 2 mol.%, whereas doping of $Cl^-$ and $F^-$ ions changed with the percentages of 1 mol.%, 2.5 mol.% and 5 mol.%. The synthesized samples sintered at 1100°C for 1h. Microstructural, mechanical and biological properties of the sintered samples were investigated.

According to the density measurements, addition of $Zn^{2+}$ ion increased the density of pure HA, whereas $F^-$ addition decreased the density of pure HA. However, as the $F^-$ amount increased, the density of the samples increased. Co-doping of $Zn^{2+}$ and $F^-$ ions highly improves the density of pure HA. For $Zn^{2+}$ and $F^-$ co-doped samples, as the $F^-$ amount increased, the density of the samples increased and the highest density was obtained for 2 Zn 5 F. $Cl^-$ doped samples had higher density values than that of pure HA due to the additional $Ca^{2+}$ ions from precursor $CaCl_2 \cdot 2H_2O$. However, fluctuations were seen with changes in the amount of doping. Co-doping of $Zn^{2+}$ and $F^-$ ions resulted in further increase in density.

XRD results shows that HA and trace amount of CaO phase detected in all samples except $Zn^{2+}$ and $F^-$ co-doped samples and 5 F sample. The intensity of CaO phase increased when $Ca^{2+}$ ion that was introduced to the system increased. The fraction of crystalline phase in the samples were calculated. $Zn^{2+}$ ion addition decreased the fraction of crystalline phase due to the decrease in Ca/P ratio whereas $F^-$ and $Cl^-$ addition increased it. As the amount of $F^-$ or $Cl^-$ increased in the samples, the fraction of crystalline phase decreased. However, fluctuations were seen in $Zn^{2+}$ and $F^-$ co-doped and $Zn^{2+}$ and $Cl^-$ co-doped samples. Lattice parameters and hexagonal unit cell volumes of the samples were calculated. In all samples except

2.5 Cl, lattice parameter “a” decreased. Lattice parameter “c” decreased in samples co-doped with $Zn^{2+}$ and $F^-$ and all $Cl^-$ doped samples except 2 Zn 2.5 Cl. These changes in lattice parameters reflected as increase in hexagonal unit cell volume of $Zn^{2+}$ doped HA and $F^-$ doped HA and decrease in hexagonal unit cell volume of $Zn^{2+}$ and $F^-$ co-doped samples. Among $Cl^-$ doped samples, only 2.5 Cl and 2 Zn 2.5 Cl increased the hexagonal unit cell volume of pure HA.

In FTIR studies, $PO_4^{3-}$ ($\nu_1$, $\nu_2$, $\nu_3$, $\nu_4$ vibrational modes) and $OH^-$ (librational and stretching) bands related to HA were observed. It was the indicator of the fact that HA was snthesized by precipitation method successfully. The bands corresponding to the residual compounds were not observed. The bands observed in $F^-$ doped samples at 711 and 3543 $cm^{-1}$ showed that $F^-$ ion was incorporated into the HA structure, successfully. In $Cl^-$ doped samples, the band detected at 3495 $cm^{-1}$ was the indicator of successful $Cl^-$ incorporation to the HA structure. Changes in the intensity of the bands and the area under the bands with the amount of doping were observed. The decrease in intiensities and the area under both $OH^-$ librational and stretching bands with the amount of $Cl^-$ and $F^-$ ions showed that $Cl^-$ and $F^-$ ions replaced with $OH^-$ ion successfully. $Zn^{2+}$ specific bands were observed at 3403 $cm^{-1}$ and 433 $cm^{-1}$ which was the indicator of successful incorporation of $Zn^{2+}$ ion to the HA structure.

SEM images showed no significant differences in surface morphologies of the samples. According to grain size calculations, $Zn^{2+}$ or $F^-$ ions addition decreased the average grain size of the samples. Moreover, further decrease in grain sizes were seen in $Zn^{2+}$ and $F^-$ co-doped samples. $Cl^-$ addition increased the grain sizes of pure HA. However, as the $Cl^-$ amount increased, grain sizes decreased. The group consisting of $Zn^{2+}$ and $Cl^-$ co-doped samples had the highest grain size values and fluctuations in grain sizes were observed.

Mechanical characterization was done by Vickers microhardness test and fracture toughness of the samples also calculated. $Zn^{2+}$ ion addition decreased the microhardness of the samples like $F^-$ ion addition. However, when these two ions co-doped into HA structure, hardness increased significantly. Moreover, hardness

increased with $F^-$ amount in the samples. $Cl^-$ addition decreased the microhardness of pure HA. However, as the $Cl^-$ amount increased, the microhardness of the samples increased. 5 Cl samples had higher Vickers microharness than pure HA. $Zn^{2+}$ and $Cl^-$ co-doping resulted in fluctuations and the microhardness values obtained were smaller than pure HA.

$Zn^{2+}$ addition decreased the fracture toughness of the sample. $F^-$ and $Cl^-$ addition seperately resulted in more brittle materials except 1 F. The fracture toughness decreased with the amount of $Cl^-$ in the samples. Co-doping of $Zn^{2+}$ and $F^-$ resulted in higher fracture toughness values whereas co-doping of $Zn^{2+}$ and $Cl^-$ did not.

$Zn^{2+}$ and $F^-$ co-doped samples gave the highest density values. According to XRD patterns, the most stable compositions corresponded to the $Zn^{2+}$ and $F^-$ co-doped samples due to the fact that no CaO phase was detected. The unit cell volumes of $Zn^{2+}$ and $F^-$ co-doped samples decreased gradually as expected whereas other samples showed fluctuated trends. Gradual decrease in unit cell volumes was also the indicator of the stability of these compositions. $Zn^{2+}$ and $F^-$ co-doped samples gave smaller grain sizes than pure HA. Co-doping of $Zn^{2+}$ and $F^-$ ions increased the Vickers microhardness values significantly and also they gave relatively higher fracture toughness values. Therefore, $Zn^{2+}$ and $F^-$ co-doped samples could be a good candidate for some biomedical applications such as metal implant coating. Cell culture studies were applied to $Zn^{2+}$ and $F^-$ doped samples due to its better structural and mechanical properties.

Alamar™ Blue assay was done to determine the behaviour of cells when they were in contact with the materials. Cell proliferation results showed that $Zn^{2+}$ incorporation to the structure increased the cell proliferation. 1 mol.% $F^-$ addition resulted in further increase in cell proliferation. However, as the amount of increase in $F^-$ content, cell proliferation rates decreased. Cells were differentiated to osteoblasts and their functionality were observed by ALP activity assay. The results were in the same trend with Alamar™ Blue assay. $Zn^{2+}$ addition increased the ALP activity and further increase was seen in 2 Zn 1 F. However, there was a sharp

decrease in 2 Zn 2.5 F and cell functionality started to increase again in 2 Zn 5 F. SEM images also supported these results. In samples 2 Zn and 2 Zn 1 F, cells spreaded extensively and had a dendritic shape which means that cells had good attachment on these samples. However, cells seeded on pure HA, 2 Zn 2.5 F and 2 Zn 5 F showed cuboidal shape. The small grain size of 2 Zn 1 F with the value 176nm was strongly related to increase in cell viability and alkaline phosphatase activity. Dissolution test in SBF was also done by measuring the change in pH of the SBF that the samples dipped in. The change in pH was higher in the samples that were put into the waterbath when compared with the samples that were put into the incubator. Moreover, the pH change increased with time in all samples which means that dissolution increased with time. Among the samples $F^-$ doped samples gave lower results than pure HA and 2 Zn which is an indicator of $F^-$ effect on low dissolution rate.

To conclude that the sample 2 Zn 1 F showed the highest results in terms of biological properties. Moreover, this sample also had superior machanical properties when compared to other samples. Therefore, it is a good candidate for biomedical applications especially in osteoporosis treatment because of the noteworthy effect of $Zn^{2+}$ ion on osteoclast cells.

## REFERENCES


[1] D. McConnell, "Apatite: Its crystal chemistry, mineralogy, utilization, and geologic and biologic occurrences", Springer-Verlag (1973) 1-63.

[2] J.M. Hughes, M. Cameron, K.D. Crowley, "Structural variations in natural F, OH, and Cl apatites", American Mineralogist 74 (1989) 870-876.

[3] T. Ikoma, A. Yamazaki, S. Nakamura, M. Akao, "Preparation and structure refinement of monoclinic hydroxylapatite", Journal of Solid State Chemistry 144 (1999) 272-276.

[4] P.E. Mackie, J.C. Elliott, R.A. Young, "Monoclinic structure of synthetic $Ca_5(PO_4)_3Cl$ chlorapatite", Acta Crystallographica Part A 28 (1972) 1840-1848.

[5] N.G. Newberry, E.J. Essene, D.R. Peacor, "Alforsite, a new member of the apatite group: The barium analogue of chlorapatite", American Mineralogist 66 (1981) 1050-1053.

[6] Y. Dai, J.M. Hughes, "Crystal structure refinements of vanadinite and pyromorphite", Canadian Mineralogist 27 (1989) 189-192.

[7] D.Y. Pushcharovskii, T.N. Nadezhina, A.P. Khomyakov, "Crystal structure of strontium apatite from Khibiny", Soviet Physics, Crystallography 32 (1987) 524-526.

[8] J. Rakovan, J.M. Hughes, "Strontium in the apatite structure: Strontian fluorapatite and belovite-(Ce)", Canadian Mineralogist 38 (2000) 839-845.

[9] P.J. Dunn, D.R. Peacor, N. Newberry, "Johnbaumite, a new member of the apatite group from Franklin, New Jersey", American Mineralogist 65 (1980) 1143-1145.

[10] Y. Dai, J.M. Hughes, P.B. Moore, " The crystal structure of mimetite and clinomimetite, $Pb_5(AsO_4)_3Cl$", Canadian Mineralogist 29 (1991) 369-376.

[11] R.C. Rouse, P.J. Dunn, D.R. Peacor, "Hedyphane from Franklin, New Jersey and Laangban, Sweden; cation ordering in an arsenate apatite", American Mineralogist 69 (1984) 920-927.

[12] P.J. Dunn, R.C. Rouse, “Morelandite, a new barium arsenate chloride member of the apatite group”, Canadian Mineralogist 16 (1978) 601-604.

[13] P.J. Dunn, E.U. Petersen, D.R. Peacor, “Turneaureite, a new member of the apatite group from Franklin, New Jersey, Balmant, New York and Laangban, Sweden”, Canadian Mineralogist 23 (1985) 251-254.

[14] R. Oberti, L. Ottolini, G. Della Ventura, G.C. Pardon, “On the symmetry and crystal chemistry of britholite: New structural and microanalytical data”, American Mineralogist 86 (2001) 1066-1075.

[15] J.H. Zhang, Z. Fang, L.B. Liao, “A study of crystal structure of britholite-Y”, Acta Mineralogica Sinica 12 (1992) 132-142.

[16] R.C. Rouse, P.J. Dunn, “A contribution to the crystal chemistry of ellestadite and the silicate sulfate apatites”, American Mineralogist 67 (1982) 90-96.

[17] I.M. Steele, J.J. Pluth , A. Livingstone, “Crystal structure of mattheddleite, a Pb, S, Si phase with the apatite structure”, Mineralogial Magazine 64 (2000) 915-921.

[18] L.M. Anovitz, B.S. Hemingway, “Thermodynamics of boron minerals: Summary of structural, volumetric and thermochemical data”, Reviews in Mineralogy and Geochemistry 33 (1996) 181-261.

[19] J.C. Elliott, Structure and chemistry of the apatites and other calcium orthophosphates, Elsevier, (1994) 4-62.

[20] U. Kockan, “Prediction of hexagonal lattie parameters of stoichiometric and non-stoichiometric apatites by artificial neural networks”, Masters thesis, Department of Micro and Nanotechnology, METU, (2009).

[21] Tulane University, http://www.tulane.edu/~sanelson/eens211/forms_zones_habit.htm, last visited on 31 December 2009.

[22] The Mineralogy Database, webmineral.com/help/CrystalSystem.shtml, last visited on 31 December 2009.

[23] B. Wopenka, J.D. Pasteris, “A mineralogical perspective on the apatite in bone”, Materials Science and Engineering C 25 (2005) 131-143.

[24] M.J. Kohn, J. Rakovan, J.M. Hughes, “Phosphates: Geochemical, geobiological and material importance”, Reviews in Mineralogy and Geochemistry 48 (2002) 631–672.

[25] M.J. Kohn, J. Rakovan, J.M. Hughes, “Phosphates: Geochemical, geobiological and material importance”, Reviews in Mineralogy and Geochemistry 48 (2002) 427– 454.

[26] M. Ma, Y. Zhu, J. Chang, “Monetite formed in mixed solvents of water and ethylene glycol and its transformation to hydroxylapatite”, Journal of Physical Chemistry Part B 110 (2006) 14226-14230.

[27] G. Vereecke, J. Lemaıˆtre, “Calculation of the solubility diagrams in the system $Ca(OH)_2$-$H_3PO_4$-KOH-$HNO_3$-$CO_2$-$H_2O$”, Journal of Crystal Growth 104 (1990) 820–832.

[28] T. Moutin, J.Y. Gal, H.E. Halouani, B. Picot, J. Bontoux, “Decrease of phosphate concentration in a high rate pond by precipitation of calcium phosphate: theoretical and experimental results”,Water Research 26 (1992) 1445–1450.

[29] W. Kossler, J. Fuchs, "Calcium orthophosphates as biomaterials and bioceramics" In S.V. Dorozhkin “Bioceramics, properties, preparation and applications” Nova Science Publishers, (2009) 65-159.

[30] B. Dickens, J.S. Bowen, “Refinement of the crystal structure of $Ca(H_2PO_4)_2 \cdot H_2O$”, Acta Crystallographica Part B 27 (1971) 2247-2255.

[31] S. Jinawath, D. Pongkao, W. Suchanek, M. Yoshimura, “Hydrothermal synthesis of monetite and hydroxylapatite from monocalcium phosphate monohydrate”, International Journal of Inorganic Materials 3 (2001) 997-1001.

[32] B. Dickens, E. Prince, L.W. Schroeder, W.E. Brown, “$Ca(H_2PO_4)_2$, a crystal structure containing unusual hydrogen bonding”, Acta Crystallographica Part B 29 (1973) 2057-2070.

[33] Mineral Information Institute, http://www.mii.org/Minerals/photophos.html #sources, last visited on 30 March 2010.

[34] L. Tortet, J.R. Gavarri, G. Nihoul, A.J. Dianoux, “Proton mobilities in bruhite and brushite/polymer composites”, Solid State Ionics 97 (1997) 253-256.

[35] L. Tortet, J.R. Gavarri, G. Nihoul, A.J. Dianoux, “Study of protonic mobility in $CaHPO_4 \cdot 2H_2O$ (brushite) and $CaHPO_4$ (monetite) by infrared spectroscopy and neutron scattering”, Journal of Solid State Chemistry 132 (1997) 6-16.

[36] D.W. Jones, J.A.S. Smith, “The structure of brushite, $CaHPO_4 \cdot 2H_2O$”, Journal of the Chemical Society (1962) 1414-1420.

[37] C.A. Beevers, “The crystal structure of dicalcium phosphate dihydrate, $CaHPO_4 \cdot 2H_2O$”, Acta Crystallographica 11 (1958) 273-277.

[38] A.O. McIntosh, W.L. Jablonski, “X-ray powder patterns of the calcium phosphates”, Analytical Chemistry 28 (1956) 1424-1427.

[39] U. Gbureck, T. Hölzel, U. Klammert, K. Würzler, F.A. Müller, J.E. Barralet, “Resorbable dicalcium phosphate bone substitutes prepared by 3D powder printing”, Advanced Functional Materials 17 (2007) 3940-3945.

[40] F. Theiss, D. Apelt, B.A. Brand, A. Kutter, K. Zlinszky, M. Bohner, “Biocompatibility and resorption of a brushite calcium phosphate cement”, Biomaterials 26 (2005) 4383–4394.

[41] P. Fraysinnet, L. Gineste, P. Conte, J. Fages, N. Rouquet, “Short-term implantation effects of a DCPD based calcium phosphate cement”, Biomaterials 19 (1998) 971–977.

[42] M. Bohner, J. Lemaitre, T.A. Ring, “Effects of sulfate, pyrophosphate, and citrate ions on the physicochemical properties of cements made of beta-tricalcium phosphate-phosphoric acid-water mixtures”, Journal of the American Ceramic Society 79 (1996) 1427-1434.

[43] J.E. Barralet, L.M. Grover, U. Gbureck, “Solid state reactions in calcium phosphate cement mixtures during ageing”, Biomaterials 25 (2004) 2197–2203.

[44] C. Pittet, J. Lemaıˆtre, **“**Mechanical characterization of brushite cements: A Mohr circles' approach”, Journal of Biomedical Materials Research Part A 53 (2000) 769–780.

[45] M. Bohner, H. P. Merkle, P. van Landuyt, G. Trophardy, J. Lemaitre, “Effect of several additives and their admixtures on the physico-chemical properties of a calcium phosphate cement”, Journal of Materials Science 11 (2000) 111–116.

[46] E. Fernandez, M.P. Ginebra, M.G. Boltong, F.C.M. Driessens, J. Ginebra, J.A. Planell, E.A.P. De Maeyer , R.M.H. Verbeeck, “Kinetic study of the setting reaction of a calcium phosphate bone cement”, Journal of Biomedical Materials Research 32 (1996) 367–374.

[47] E. Fernandez, F.J. Gil, S. Best, M.P. Ginebra, F.C.M. Driessens, J.A. Planell, "The cement setting reaction in the $CaHPO_4$-α -$Ca_3(PO_4)_2$ system: An X ray diffraction study", Journal of Biomedical Materials Research 42 (1998) 403–406.

[48] E. Fernandez, F.J. Gil, S. Best, M.P. Ginebra, F.C.M. Driessens, J.A. Planell, "Improvement of the mechanical properties of new calcium phosphate bone cements in the $CaHPO_4$–$Ca_3(PO_4)_2$ system: Compressive strength and microstructural development", Journal of Biomedical Materials Research 41 (1998) 560–567.

[49] B.Dickens, J.S. Bowen, W.E. Brown, "A refinement of the crystal structure of $CaHPO_4$ (synthetic monetite)", Acta Crystallographica Part B 28 (1972) 797-806.

[50] J.P. Smith, J.R. Lehr, W.E. Brown, "Crystallography of monocalcium and dicalcium phosphates", American Mineralogist 40 (1955) 893-899.

[51] S. Jinawatah, D. Pongkao, W. Sunchanek, M. Youshimura, "Hydrothermal synthesis of monetite and hydroxylapatite from monocalcium phosphate monohydrate", International Journal of Inorganic Materials 3 (2001) 997–1001.

[52] S. Hsu, E. Chang, H.S. Liub, "Hydrothermally-grown monetite ($CaHPO_4$) on hydroxylapatite", Ceramics International 24 (1998) 249–253.

[53] X.D. Kong, X.D. Sun, J.B. Lu, F.Z. Cui, "Mineralization of calcium phosphate in reverse microemulsion", Current Applied Physics 5 (2005) 519–521.

[54] G.R. Sivakumar, E.K. Girija, S.N. Kalkura, C. Subramanian, "Crystallization and characterization of calcium phosphates: brushite and monetite", Crystal Research and Technology 33 (1998) 197–205.

[55] R. Rohanizadeh, R.Z. LeGeros, M. Harsono, A. Bendavid, "Adherent apatite coating on titanium substrate using chemical deposition", Journal of Biomedical Materials Research Part A 72 (2005) 428–438.

[56] R. Rohanizadeh, R.Z. LeGeros, "Novel method of hydroxyapatite coating on titanium using chemical deposition", Key Engineering Materials 361–363 (2008) 617–620.

[57] W. Bonfield, S.M. Best, A. Nobuyuki, "Method for coating a calcium phosphate compound onto a metallic material", World Intellectual Property Organization (WIPO), 1998, WO9813539.

[58] The European Food Information Council (EUFIC), http://www.eufic.org /upl/1/default/doc/enumbers_ eufic.pdf, last visited on 12 April 2010.

[59] O. Suzuki, M. Nakamura, Y. Miyasaka, M. Kagayama, M. Sakurai, "Bone-formation on synthetic precursors of hydroxyapatite", Tohoku Journal of Experimental Medicine 164 (1991) 37–50.

[60] P. Habibovic, U. Gbureck, C.J. Doillon, D.C. Bassett, C.A. van Blitterswijk, J.E. Barralet, "Osteoconduction and osteoinduction of low-temperature 3D printed bioceramic implants", Biomaterials 29 (2008) 944–953.

[61] P.G. Werness, J.H. Bergert, L.H. Smith, "Crystalluria", Journal of Crystal Growth 53 (1981) 166-181.

[62] M. Daudon, R. Donsimoni, C. Hennequin, S. Fellahi, G. Lemoel, M. Paris, S. Troupel, B. Lacour, "Sex- and age-related composition of 10 617 calculi analyzed by infrared spectroscopy", Urological Research 23 ( 1995) 319-326.

[63] H.D. Jiang, X.Y. Liu, C.T. Lim, C.Y. Hsu, "Ordering of self-assembled nanobiominerals in correlation to mechanical properties of hard tissues", Applied Physics Letters 86 (2005) 1-3.

[64] X. Xin-bo, Z. Xie-rong, Z. Chun-li, L. Ping, F. Yun-bo, "Influence of hydrothermal temperature on hydroxyapatite coating transformed from monetite on HT-C/C composites by induction heating method", Surface and Coatings Technology 204 (2009) 115-119.

[65] Q. Ruan,Y. Zhu, Y. Zeng, H. Qian, J. Xiao, F. Xu, L. Zhang, D. Zhao, "Ultrasonic irradiation-assisted oriented assembly of ordered monetite nanosheets stacking", Journal of Physical Chemistry Part B 113 (2009) 1100-1106.

[66] H. McDowell, W.E. Brown, and J.R. Sutter, ''Solubility study of calcium hydrogen phosphate: Ion pair formation'', Inorganic Chemistry 10 (1971) 1638-1643.

[67] F.C.M. Driessens, R.M.H. Verbeeck, Biominerals, CRC Press, Boca Raton, FL, USA (1990) 37–59.

[68] T. Kawasaki, W. Kobayashi, ''Apatite Chromatography Column System''; U.S. Patent No. 4,874,511, (1989).

[69] J.G. Rabatin, R.H. Gale, A.E. Newkirk, ‘‘The mechanism and kinetics of the dehydration of calcium hydrogen phosphate dihydrate”, Journal of Physical Chemistry 64 (1960) 491–493.

[70] M.C. Ball, M.J. Casson, ‘‘Dehydration of calcium hydrogen phosphate dihydrate’’, Journal of the Chemical Society 1 (1973) 34-37.

[71] M. Landin, R.C. Rowe, P. York, ‘‘Structural changes during the dehydration of dicalcium phosphate dihydrate’’, European Journal of Pharmaceutical Sciences 2 (1994) 245–252.

[72] A.C. Tas, S.B. Bhaduri, ‘‘Chemical processing of $CaHPO_4 \cdot 2H_2O$: Its conversion to hydroxyapatite’’, Journal of the American Ceramic Society 87 (2004) 2195–2200.

[73] C.F. Chenot, ‘‘Method of converting brushite to monetite crystals with controlled variation in crystal habit’’; U.S. Patent No. 3,927,180, (1975).

[74] K. Wei, C. Lai, Y. Wang, ‘‘Formation of monetite nanoparticles and nanofibers in reverse micelles’’, Journal of Material Science 42 (2007) 5340–5346.

[75] O. Takagi, K. Azumo, T. Iwamura, ‘‘Process for producing hydroxylapatites’’, U. S. Patent No. 5,073,357, 17 December 1991.

[76] H.H.K. Xu, L. Sun, M.D. Weir, J.M. Antonucci, S. Takagi, L.C. Chow, M. Peltz, “Nano DCPA-whisker composites with high strength and Ca and $PO_4$ release”, Journal of Dental Research 85 (2006) 722–727.

[77] S. Jinawath, D. Pungkao, W. Suchanek, M. Yoshimura, “Hydrothermal synthesis of monetite and hydroxyapatite from monocalcium phosphate monohydrate”, International Journal of Inorganic Materials 3 (2001) 997–1001.

[78] G. Thomas, H. Dehbi, “Effect of water on monetite synthesis in the solid state”, Materials Chemistry and Physics 15 (1986) 1–13.

[79] Y.S. Hsu, E. Chang, H.S. Liub, “Hydrothermally grown monetite ($CaHPO_4$) on hydroxyapatite”, Ceramics International 24 (1998) 249-254.

[80] A.C. Tas, “Monetite ($CaHPO_4$) synthesis in ethanol at room temperature”, Journal of the American Ceramic Society 92 (2009) 2907-2912.

[81] Biomedical Engineering Online, http://www.biomedical-engineering-online.com/content/3/1/8, last visited on 10 April 2010.

[82] Y. Zhang, J. Lu, J. Wang, S.Yang, Y. Chen, "Synthesis of nanorod and needle-like hydroxyapatite crystal and role of pH adjustment", Journal of Crystal Growth 311 (2009) 4740-4746.

[83] B. Dickens, W.E. Brown, G.J. Kruger, J.M. Stewart, "$Ca_4(PO_4)_2O$, tetracalcium diphosphate monoxide: Crystal structure and relationships to $Ca_5(PO_4)_3OH$ and $K_3Na(SO_4)_2$", Acta Crystallographica Part B 29 (1973) 2046-2056.

[84] S.J. Kalita, A. Bhardwaj, H.A. Bhatt, "Nanocrystalline calcium phosphate ceramics in biomedical engineering", Materials Science and Engineering C 27 (2007) 441-449.

[85] H. Oonishi, S. Kushitani, M. Aono, F. Sugihara, Y. Mandai, E. Tsuji, T. Mizukoshi, "Fully bioactive bone cement using tetra-calciumphosphate and collagen", Transactions of the Annual Meeting of the Society for Biomaterials in conjunction with the International Biomaterials Symposium 14 (1991) 306.

[86] M. Mathew, W.E. Brown, L.W. Schroeder, B. Dickens, "Crystal structure of octacalcium bis(hydrogenphosphate) tetrakis(phosphate)pentahydrate, $Ca_8(HPO_4)_2(PO_4)_4 \cdot 5H_2O$", Journal of Crystal Spectroscopy Research 18 (1988) 523-527.

[87] W.E. Brown, J.P. Smith, J.R. Lehr, A.W. Frazier, "Octacalcium phosphate and hydroxyapatite: Crystallographic and chemical relations between octacalcium phosphate and hydroxyapatite", Nature 196 (1962) 1050-1055.

[88] M. Iliescu, V. Nelea, J. Werckmann, I.N. Mihailescu, G. Socol, Adriana Bigi, Barbara Bracci, "Electron microscopy studies of octa-calcium phosphate thin films obtained by pulsed laser deposition", Thin Solid Films 453 –454 (2004) 157–161.

[89] M. Mathew, S. Takagi, "Structures of biological minerals in dental research", Journal of the Research National Institute of Standards and Technology 106 (2001) 1035-1044.

[90] L.C. Chow, E.D. Eanes, "Octacalcium Phosphate", Monographs in Oral Science, Basel, Karger, 18 (2001).

[91] B. Dickens, L.W. Schroeder, W.E. Brown."Crystallographic studies of the role of Mg as a stabilizing impurity in β-$Ca_3(PO_4)_2$. 1. The crystal structure of pure β-$Ca_3(PO_4)_2$", Journal of Solid State Chemistry 10 (1974) 232-248.

[92] M.U. Nylen, E.D. Eanes, K.A. Omnell, "Crystal growth in rat enamel", The Journal of Cell Biology 18 (1963) 109-123.

[93] A. Rodrigues, A. Lebugle, "Behavior in wet atmosphere of an amorphous calcium phosphate with an atomic Ca/P ratio of 1.33", Journal of Solid State Chemistry 148 (1999) 308-315.

[94] N.C. Blumenthal, A.S. Posner, J.M. Holmes, "Effect of preparation conditions on the properties and transformation of amorphous calcium phosphate", Materials Research Bulletin 7 (1972) 1181-1190.

[95] M. Bohner, J. Lemaitre, "Effects of sulfate, pyrophosphate, and citrate ions on the physicochemical properties of cements made of b-tricalcium phosphate–phosphoric acid water mixtures", Journal of the American Ceramic Society 79 (1996) 1427–1437.

[96] J. Zhou, X. Zhang, J. Chen, S. Zeng, K. De groot, "High temperature characteristics of synthetic hydroxyapatite", Journal of Materials Science: Materials in Medicine 4 (1993) 83–85.

[97] R. Famery, N. Richard, P. Boch, "Preparation of α- and β- tricalcium phosphate ceramics, with andwithout magnesium addition", Ceramics International 20 (1994) 327–336.

[98] M.Yashima, A.Sakai, T. Kamiyama, A. Hoshikawa, "Crystal structure analysis of β-tricalcium phosphate $Ca_3(PO_4)_2$ by neutron powder diffraction", Journal of Solid State Chemistry 175 (2003) 272–277.

[99] K.P. Sanosh, M.C. Chu, A. Balakrishnan, T.N. Kim, S.J. Cho, "Sol–gel synthesis of pure nano sized β-tricalcium phosphate crystalline powders", Current Applied Physics 10 (2010) 68–71.

[100] J. Ando, "Phase Diagrams of $Ca_3(PO_4)_2$–$Mg_3(PO_4)_2$ System", Bulletin of the Chemical Society of Japan 31 (1958) 201-205.

[101] M. Bohner, J. Lemaitre, A.P. Legrand, J.B. d'Espinose de la Caillerie, P. Belgrand, "Synthesis, X-ray diffraction and solid-state $^{31}P$ magic angle spinning NMR study of α-tricalcium orthophosphate", Journal of Materials Science: Materials in Medicine 7 (1996) 457–463.

[102] H.S. Ryu, H.J. Youn, K.S. Hong, B.S. Chang, C.K. Lee, S.S. Chung, " An improvement in sintering property of β-tricalcium phosphate by addition of calcium pyrophosphate", Biomaterials 23 (2002) 909–914.

[103] T. Kanazawa, T. Umegaki, N. Uchiyama, ”Thermal crystallization of amorphous calcium phosphate to α-tricalcium phosphate”, Journal of Chemical Technology and Biotechnology 32 (1982) 399–406.

[104] U. Gburecka, O. Grolms, J.E. Barralet, L.M. Grover, R. Thull, “Mechanical activation and cement formation of β-tricalcium phosphate”, Biomaterials 24 (2003) 4123-4131.

[105] M. Mathew, L.W. Schroeder, B. Dickens, W.E. Brown, “The crystal structure of α-$Ca_3(PO_4)_2$”, Acta Crystallographica B 33 (1977) 1325-1333.

[106] C. Durucan, P.W. Brown, “α-Tricalcium phosphate hydrolysis to hydroxyapatite at and near physiological temperature”, Journal of Material Science: Materials in Medicine 11 (2000) 365–371.

[107] C. Durucan, P.W. Brown, “Reactivity of alpha-tricalcium phosphate”, Journal of Materials Science 37 (2002) 963–969.

[108] A. Bigi, E. Boanini, R. Botter, S. Panzavolta, K. Rubini, “α-Tricalcium phosphate hydrolysis to octacalcium phosphate: effect of sodium polyacrylate”, Biomaterials 23 (2002) 1849–1854.

[109] K. Kurashina, H. Kurita, A. Kotani, H. Takeuchi, M. Hirano, “In vivo study of a calcium phosphate cement consisting of α-tricalcium phosphate/ dicalcium phosphate dibasic/ tetracalcium phosphate monoxide”, Biomaterials 18 (1997) 147-151.

[110] E. Bonanini, S. Panzavolta, K. Rubini, M. Gandolfi, A. Bigi, “Effect of strontium and gelatin on the reactivity of α-tricalcium phosphate”, Acta Biomaterialia 6 (2010) 936-942.

[111] M.P. Ginebra, E. Fernandez, F.C.M. Driessens, J.A. Planell, “Modelling of the hydrolysis of α-tricalcium phosphate”, Journal of the American Ceramic Society 82 (1999) 2808-2812

[112] K. Udoh, M.L. Munar, M. Maruta, S. Matsuya, K. Ishikawa, “Effects of sintering temperature on physical and compositional properties of α-tricalcium phosphate foam”, Dental Materials Journal 29 (2010) 154-159.

[113] M.D. Vlad, E.V. Sindilar, M.L. Marinoso, I. Poeata, R. Torres, J. Lopez, M. Barraco, E. Fernandez, “Osteogenic biphasic calcium sulphate dihydrate/iron modified α-tricalcium phosphate bone cement for spinal applications: in vivo study”, Acta Biomaterialia 6 (2010) 607-616.

[114] G. Szabo, Z. Suba, K. Hrabak, "Autogenous bone versus beta-tricalcium phosphate graft alone for bilateral sinus elevations (2- and 3-dimensional computed tomographic, histologic, and histomorphometric evaluations): preliminary results", The International Journal of Oral and Maxillofacial Implants 16 (2001) 681–692.

[115] K.C.B. Yeong, J. Wang, S.C. Ng, "Fabricating densified hydroxyapatite ceramics from a precipitated precursor", Materials Letters 38 (1999) 208–213.

[116] R.S. Gilmore RS, J.L. Katz, "Elastic properties of apatites", Journal of Materials Science 17 (1982) 1131-1141.

[117] M.A. Lopez, R.F. Silva, F.J. Monteiro, J.D. Santos, "Microstructural dependence of Young's and shear moduli of $P_2O_5$ glass reinforced hydroxyapatite for biomedical applications", Biomaterials, 21 (2000) 749-754.

[118] L. Liang, P. Rulis, W.Y. Ching, "Mechanical properties, electronic structure and bonding of α- and β-tricalcium phosphates with surface characterization", Acta Biomaterialia 6 (2010) 3763-3771.

[119] Y. Harada, J.T. Wang, V.A. Doppalapudi, A.A. Willis, M. Jasty, W.H. Harris, M. Nagase, S.R. Goldring, "Differential effects of different forms of hydroxyapatite and hydroxyapatite/tricalcium phosphate particulates on human monocyte/macrophages in vitro", Journal of Biomedical Materials Research 31 (1996) 19–26.

[120] J. Le Huec, C. Le Huec, D. Clément, S. Aunoble, C. Tournier, M. Françoise Harmand, "A brief summary of 15 years of research on beta-tricalcium phosphates", Spine Arthroplasty Society Journal 3 (2009) 108-117.

[121] A. Ogose, T. Hotta, H. Hatano, H. Kawashima, K. Tokunaga, N. Endo, H. Umezu, "Histological examination of beta-tricalcium phosphate graft in human femur", Journal of Biomedical Materials Research 63 (2002) 601–604.

[122] N. Matsushita, H. Terai, T. Okada, K. Nozaki, H. Inoue, S. Miyamoto, K. Takaoka, "A new bone-inducing biodegradable porous β-tricalcium phosphate", Journal of Biomedical Materials Research 70 (2004) 450-458.

[123] P. Kasten, R. Luginbühl, M. van Griensven, T. Barkhausen, C. Krettek, M. Bohner, U. Bosch, "Comparison of human bone marrow stromal cells seeded on calcium-deficient hydroxyapatite, β-tricalcium phosphate and demineralized bone matrix", Biomaterials 24 (2003) 2593–2603.

[124] M. Nyan, T. Miyahara, K. Noritake, J. Hao, R. Rodriguez, S. Kuroda, S. Kasugai, "Molecular and tissue responses in the healing of rat calvarial defects after local application of simvastatin combined with alpha tricalcium phosphate", Journal of Biomedical Materials Research Part B: Applied Biomaterials 93 (2010) 65-73.

[125] I. Orly, M. Gregoire, J. Menanteau, M. Dard, "Effects of synthetic calcium phosphates on the 3H-thymidine incorporation and alkaline phosphatase activity of human fibroblasts in culture", Journal of Biomedical Materials Research 23 (1989) 1433–1440.

[126] P. Ducheyne, S. Radin, L. King, "The effect of calcium phosphate ceramic composition and structure on in vitro behavior: I. Dissolution", Journal of Biomedical Materials Research 27 (1993) 25–34.

[127] R.S. Spitzer, C. Perka, K. Lindenhayn, H. Zippel, "Matrix engineering for osteogenic differentiation of rabbit periosteal cells using α-tricalicum phosphate particles in a three-dimensional fibrin culture", Journal of Biomedical Materials Research, 59 (2002) 690-696.

[128] Hydroxyapatites-synthesis of hydroxyapatite powders, http://www.azom .com/arti cle.aspx?ArticleID=1519, last visited on 28th July 2011.

[129] G. Ma, X.Y. Liu, "Hydroxyapatite: Hexagonal or monoclinic?", Crystal Growth and Design 9 (2009) 2991-1994.

[130] R.Z. LeGeros, J.P. LeGeros, "Dense hydroxyapatite", In L.L. Hench, J. Wilson, An Introductuion To Bioceramics, World Scientific Press (1993) 139-180.

[131] Database of Ionic Radii, http://abulafia.mt.ic.ac.uk/shannon/radius.php? Element=F, last visited on 26th January 2011.

[132] B.S. Moonga, D.W. Dempster, "Zinc is a potent inhibitor of osteoclastic bone resorption in vitro", Journal of Bone and Mineral Research 10 (1995) 453-457.

[133] A. Ito, K. Ojima, H. Naito, N. Ichinose, T. Tateishi, "Preparation, solubility, and cytocompatibility of zinc-releasing calcium phosphate ceramics", Journal of Biomedical Materials Research 50 (2000) 178-183.

[134] E. Jallot, J.M. Nedelec, A.S. Grimault, E. Chassot, A. Grandjean-Laquerriere, P. Laquerriere, D. Laurent-Maquin, "STEM and EDXS characterisation of physico-chemical reactions at the periphery of sol–gel derived Zn-substituted hydroxyapatites during interactions with biological fluids", Colloids and Surfaces B: Biointerfaces 42 (2005) 205-210.

[135] S.L. Hall, H.P. Dimai, J.R. Farley, "Effects of zinc on human skeletal alkaline phosphatase activity in vitro", Calcified Tissue International 64 (1999) 163–172.

[136] A. Peretz, T.E. Papadopoulos, D. Wiltems, A. Hotimsky, N. Michiels, M. Siderova, P. Bergmann, J. Neve, "Zinc supplementation increases bone alkaline phosphatase in healthy men", Journal of Trace Elements in Medicine and Biology 15 (2001) 175-178.

[137] C. Ergun, T.J. Webster, R. Bizios, R.H. Doremus, "Hydroxylapatite with substituted magnesium, zinc, cadmium, and yttrium. I. Structure and microstructure", Journal of Biomedical Materials Research Part A 59 (2002) 305-311.

[138] L.J. Jha, S.M. Best, J.C. Knowles, "Preparation and characterization of fluoride-substituted apatites", Journal of Materials Science: Materials in Medicine 8 (1997) 185-191.

[139] H.W.Kim, Y.J. Noh, Y.H. Koh, H.E. Kim, "Enhanced performance of fluorine substituted hydroxyapatite composites for hard tissue engineering", Journal of Materials Science: Materials in Medicine 14 (2003) 899-904.

[140] M. Mousny, S. Omelon, L. Wise, E.T. Everett, M. Dumitriu, D.P. Holmyard, X. Banse, J.P. Devogelaer, M.D. Grynpas," Fluoride effects on bone formation and mineralization are influenced by genetics", Bone 43 (2008) 1067–1074.

[141] M.A. Rauschmann, T.A. Wichelhaus, V. Stirnal, E. Dingeldein, L. Zichner, R. Schnettler, V. Alt, "Nanocrystalline hydroxyapatite and calcium sulphate as biodegradable composite carrier material for local delivery of antibiotics in bone infections", Biomaterials 26 (2005) 2677-2684.

[142] M. Inoue, R.Z. LeGeros, M.Inoue, H. Tsujigiwa, H. Nagatsuka, T. Yamamoto, N. Nagai, "In vitro response of osteoblast-like and odontoblast-like cells to unsubstituted and substituted apatites", Journal of Biomedical Materials Research A 70 (2004) 585-593.

[143] Z.L. Zhu, H.Y. Yu, Q. Zeng, H.W. He, "Characterization and biocompatibility of fluoridated biphasic calcium phosphate ceramics", Applied Surface Science 255 (2008) 552–554.

[144] S. Kannan, A. Rebelo, J.M.F. Ferreira, "Novel synthesis and structural characterization of fluorine and chlorine co-substituted hydroxyapatites", Journal of Inorganic Biochemistry 100 (2006) 1692-1697.

[145] F. Wen, X. Zhao, H. Ding, H. Huo, J. Chen, "Hydrothermal synthesis and photoluminesent properties of $Sb^{3+}$-doped and ($Sb^{3+}$,$Mn^{2+}$)-co-doped calcium hydroxyapatite", Journal of Materials Chemistry 12 (2002) 3761–3765.

[146] E. Landi, A. Tampieri, M. Mattioli-Belmonte, G. Celotti, M. Sandri, A.Gigante, P. Fava, G. Biagini, "Biomimetic Mg- and Mg,$CO_2^{3-}$substituted hydroxyapatites: synthesis characterization and in vitro behaviour", Journal of the European Ceramic Society 26 (2006) 2593–2601.

[147] Z.P. Sun, B. Ercan, Z. Evis, T.J. Webster, "Microstructural, mechanical, and osteocompatibility properties of $Mg^{2+}$/$F^-$ -doped nanophase hydroxyapatite", Journal of Biomedical Materials Research A 94 (2010) 806-815.

[148] Z. Evis, B. Basar, Z.P. Sun, "Diametral strength testing of hydroxyapatites doped with yttrium and fluoride", Advances in Applied Ceramics 109 (2010) 383-388.

[149] V.P. Orlovskii, V.S. Komlev, S.M. Barinov, "Hydroxyapatite and hydroxyapatite-based ceramics", Inorganic Materials 38 (2002) 1159-1172.

[150] B. Chen, T. Zhang, J. Zhang, Q. Lin, D. Jiang, "Microstructure and mechanical properties of hydroxyapatite obtained by gel-casting process", Ceramics International 34 (2008) 359–364.

[151] E.C. Shors, R.E. Holmes, "Porous hydroxyapatite", In L.L. Hench, J. Wilson, An Introductuion To Bioceramics, World Scientific Press (1993) 180-222.

[152] A. Zamiri, S. De, "Mechanical properties of hydroxyapatite single crystals from nanoindentation data", Journal of the Mechanical Behaviour of Biomedical Materials, Article in press.

[153] A.Ito, K. Teraoka, S. Tsutsumi, T. Tateishi, "Single crystal hydroxyapatite: Preparation, composition and mechanical properties", In T. Kokubo, T. Nakamura, F. Miyaji, Bioceramics, Pergamon Press (1996) 189-192.

[154] O. Prokopiev, I. Sevostianov, “Dependence of the mechanical properties of sintered hydroxyapatite on the sintering temperature”, Materials Science and Engineering A 431 (2006) 218–227.

[155] S.J. Kalita, H.A. Bhatt, “Nanocrystalline hydroxyapatite doped with magnesium and zinc: Synthesis and characterization”, Materials Science and Engineering C 27 (2007) 837-848.

[156] M. Jelínek, T. Kocourek, K. Jurek, J. Remsa, J. Mikšovský, M. Weiserová, J. Strnad, T. Luxbacher, “Antibacterial properties of Ag-doped hydroxyapatite layers prepared by PLD method”, Applied Physics A 101 (2010) 615-620.

[157] M.C. Murad, I. Sopyan, C. Rohaida, Z. Ahmad, M. Reusmaazran, “Fabrication and characterization of strontium-doped hydroxyapatite bioceramics scaffolds for bone implant application: A preliminary study”, Advanced Materials Research 93-94 (2010) 401-404.

[158] W. Chen, S. Oh, A.P. Ong, N. Oh, Y. Liu, H.S. Courtney, M. Appleford, J.L. Ong, “Antibacterial and osteogenic properties of silver-containing hydroxyapatite coatings produced using a sol gel process”, Journal of Biomedical Materials Research Part A (2007)

[159] C. Capuccini, P. Torricelli, F. Sima, E. Boanini, C. Ristoscu, B. Bracci, G. Socol, M. Fini, I.N. Mihailescu, A. Bigi, “Strontium-substituted hydroxyapatite coatings synthesized by pulsed-laser deposition: In vitro osteoblast and osteoclast response”, Acta Biomaterialia 4 (2008) 1885–1893.

[160] S. C. Verberckmoes, G. J. Behets, L. Oste, A. R. Bervoets, L. V. Lamberts, M. Drakopoulos, A. Somogyi, P. Cool, W. Dorrine, M. E. De Broe, P. C. D’Haese, “Effects of Strontium on the Physicochemical Characteristics of Hydroxyapatite”, Calcified Tissue International (2004) 75:405–415.

[161] C. Paluszkiewicz, A. Slosarczyk, D. Pijocha, M. Sitarz, M. Bucko, A. Zima, A. Chroscicka, M. Lewandowska-Szumiel, “Synthesis, structural properties and thermal stability of Mn-doped hydroxyapatite”, Journal of Molecular Structure 976 (2010) 301–309.

[162] H. Marques da Silva, M. Mateescu, A. Ponche, C. Damia, E. Champion, G. Soares, K. Anselme, “Surface transformation of silicon-doped hydroxyapatite immersed in culture medium under dynamic and static conditions”, Colloids and Surfaces B: Biointerfaces 75 (2010) 349–355.

[163] T. J. Webster, C. Ergun, R.H. Doremus, R. Bizios, "Hydroxylapatite with substituted magnesium, zinc, cadmium, and yttrium. II. Mechanisms of osteoblast adhesion", Journal of Biomedical Research Part A 59 (2002) 312-317.

[164] Y. Li, C.P. Ooi, P.H.N. Cheang, "Synthesis and Characterization of Neodymium(III) and Gadolinium(III)-Substituted Hydroxyapatite as Biomaterials", International Journal of Applied Ceramic Technology 6 (2009) 501–512.

[165] T.J.Webster, E.A. Massa-Schlueter, J.L.Smith, E.B.Slamovich, "Osteoblast response to hydroxyapatite doped with divalent and trivalent cations", Biomaterials 25 (2004) 2111–2121.

[166] F.H. Martini, J.L. Nath, "Fundamentals of Anatomy and Physiology", Pearson (2009) 185-193.

[167] S.C. Cowin, "Bone Mechanics", CRC Press (1989) 97-157.

[168] J.D. Currey, "Bones: Structure and Mechanics", Princeton University Press (2002) 54-173.

[169] S. Weiner, H.D. Wagner, "The material bone: structure mechanical function relations", Annual Review of Materials Science 28 (1998) 271-298.

[170] Orthoteers, http://www.orthoteers.com/%28S%28xqggt12ov1dqeh451a1upjri%29%29/mainpage.aspx?section=16&article=606, last visited on 04 August 2010.

[171] W.S.S. Jee, "Integrated bone tissue physiology: anatomy and physiology", In S.C. Cowin, Bone Mechanics Handbook, CRC Press (2001) 21.

[172] Bone Tissue and Skeleton, http://stevebambas.com/AP%20220%20Bone%20Tissue.htm, last visited on 03 August 2010.

[173] A. Boskey, "Bone mineral crystal", Osteoporosis International 14 (2003) 16-21.

[174] S. Weiner, W. Traub, "Bone structure: from angstroms to microns", The Federation of American Societies for Experimental Biology Journal 8 (1992) 879-885.

[175] C.E. Brown, "Noninvasive analysis of bone mineral content", Bulletin of Magnetic Resonance 8 (1986) 78-83.

[176] R.K. Rude, “Magnesium homeostasis”, In: J.P. Bilezikian, L.G. Raisz, G.A. Rodan (Ed.), Principles of Bone Biology, Academic Press 1 (2002) 339-358.

[177] Logos, http://www.anl.gov/Media_Center/logos21-1/cadmium01.htm, last visited on 06 September 2010.

[178] F. Bronner, “Metals in bone”, In: J.P. Bilezikian, L.G. Raisz, G.A. Rodan (Ed.), Principles of Bone Biology, Academic Press 1 (2002) 359-369.

[179] B.D. Cullity, “Elements of X-ray Diffraction 2nd Edition”, Addison-Wesley Publishing Company (1978) 501.

[180] E. Landi, A. Tampieri, G. Celotti, S. Sprio, “Densification behaviour and mechanisms of synthetic hydroxyapatites”, Journal of the European Ceramic Society 20 (2000) 2377–2387.

[181] A.C. Larson, R.B. Von Dreele, “General Structure Analysis System (GSAS) Report LAUR (2000) 86-748”, http://www.ccp14.ac.uk/solution/gsas/index .html, last visited on 28th July 2011.

[182] C.B. Ponton, R.D. Rawlings, “Vickers indentation fracture toughness test part I: Review of literature and formulation of standardized indentation toughness equation”, Materials Science and Technology 5 (1989) 865-872.

[183] Z. Evis, “Synthesis and characterization of HA-inert ceramic composites and their coatings on biomaterilas”, Doctoral thesis, The Graduate Faculty of Engineering Science, Rensselaer Polytechnic Institute, (2003).

[184] A. Slosarczyk, J. Bialoskorski, “Hardness and fracture toughness of dense calcium phosphate-based materials”, Journal of Materials Science: Materials in Medicine 9 (1998) 103-108.

[185] W. Xue, K. Dahlquist, A. Banerjee, A. Bandyopadhyay, S. Bose, “Synthesis and characterization of tricalcium phosphate with Zn and Mg based dopants”, Journal of Materials Science: Materials in Medicine 19 (2008) 2669–2677.

[186] S.J. Kalita, M. Ferguson, “Fabrication of 3-D porous Mg/Zn doped tricalcium phosphate bone-scaffolds via the fused deposition modelling”, American Journal of Biochemistry and Biotechnology 2 2 (2006) 57-60.

[187] A. Bandyopadhyay, E.A. Withey, J. Moore, S. Bose, “Influence of ZnO doping in calcium phosphate ceramics”, Materials Science and Engineering C 27 (2007) 14–17.

[188] S.M. Toker, Z. Evis, A. Tezcaner, "Investigation of microstructure, microhardness and biocompatibility characteristics of yttrium and fluoride doped hydroxyapatite", 15th National Biomedical Engineering Meeting, Turkey (2010) 1-5.

[189] H. Qu, M. Wei, "Effect of fluorine content on mechanical properties of sintered fluoridated hydroxyapatite", Materials Science and Engineering C 26 (2006) 46 – 53.

[190] A. Bianco, I. Cacciotti, M. Lombardi, L. Montanaro, E. Bemporad, M. Sebastiani, "F-substituted hydroxyapatite nanopowders: Thermal stability, sintering behaviour and mechanical properties", Ceramics International 36 (2010) 313–322.

[191] K.A. Gross, L.M. Rodriguez-Lorenzo, "Sintered hydroxyfluorapatites. Part 2: mechanical properties of soild solutions determined by microindentation", Biomaterials 25 (2004) 1385-1394.

[192] K.A. Gross, K.A. Bhadang, " Sintered hydroxyfluorapatites. Part 3: sintering and resultant mechanical properties of sintered blends of hydroxyapatite and fluorapatite", Biomaterials 25 (2004) 1395-1405.

[193] S. Kannan, A. Rebelo, A.F. Lemos, A. Barba, J.M.F. Ferreira, "Synthesis and mechanical behaviour of chlorapatite and chlorapatite/β-TCP composites", Journal of the European Ceramic Society 27 (2007) 2287–2294.

[194] N. Zhanglei, L. Wenjun, C. Zhidong, Z. Hualei, H. Na, "Preparation, characterization, and performance of zinc-substituted hydroxyapatite", Bioinformatics and Biomedical Engineering, (iCBBE) 2011 5th International Conference on 10-12 May (2011) 1-4.

[195] Z. Evis, "Microstructural investigation of $Cu^{2+}$ doped nanohydroxyapatites", Materials Science and Technology 26 (2010) 630-632.

[196] Y. Tang, H.F. Chappell, M.T. Dove, R.J. Reeder, Y.J. Lee, "Zinc incorporation into hydroxylapatite", Biomaterials 30 (2009) 2864–2872.

[197] A. Slosarczyk, Z. Paszkiewicz, C. Paluszkiewicz, "FTIR and XRD evaluation of carbonated hydroxyapatite powders synthesized by wet methods", Journal of Molecular Structure 744-747 (2005) 657–661.

[198] M.H. Fathi, E.M. Zahrani, "Fabrication and characterization of fluoridated hydroxyapatite nanopowders via mechanical alloying", Journal of Alloys and Compounds 475 (2009) 408–414.

[199] E. Bertoni, A. Bigi, G. Cojazzi, M. Gandolfi, S. Panzavolta, N. Roveri, "Nanocrystals of magnesium and fluoride substituted hydroxyapatite", Journal of Inorganic Biochemistry 72 (1998) 29-35.

[200] Database of Ionic Radii, http://abulafia.mt.ic.ac.uk/shannon/radius.php ?orderby=Coord&dir=1&Element=OH, last visited on 26th January 2011.

[201] P. Rulis, L. Ouyang, W.Y. Ching, "Electronic structure and bonding in calcium apatite crystals: Hydroxyapatite, fluorapatite, chlorapatite, and bromapatite", Physical Review B 70 (2004) 155104-155112.

[202] S. Catros, F. Guillemot, E. Lebraud, C. Chanseau, S. Perez, R. Bareille, J. Amédée, J.C. Fricain, "Physico-chemical and biological properties of a nano-hydroxyapatite powder synthesized at room temperature", Ingenierie et Recherche Biomedicale 31 (2010) 226–233.

[203] A. Slosarczyk, Z. Paszkiewicz, C. Paluszkiewicz, "FTIR and XRD evaluation of carbonated hydroxyapatite powders synthesized by wet methods", Journal of Molecular Structure 744–747 (2005) 657–661.

[204] H. Ramesh, K. Parthipan, P.S. Rao, "EPR, FTIR, Powder XRD and Optical Absorption Studies of Cu(II) Ion in Triaqua (1,10-Phenanthroline-$k^2$N,N')(Sulfato-kO)Zinc(II)", Applied Magnetic Resonance 40 (2011) 513-524.

[205] H.U. Lee, Y.S. Jeong, S.Y. Park, S.Y. Jeong, H.G. Kim, C.R. Cho, "Surface properties and cell response of fluoridated hydroxyapatite/$TiO_2$ coated on Ti substrate", Current Applied Physics 9 (2009) 528–533.

[206] G. Cakmak, I. Togan, F. Severcan, "17β-Estradiol induced compositional, structural and functional changes in rainbow trout liver, revealed by FTIR spectroscopy: A comparative study with nonylphenol", Aquatic Toxicology 77 (2006) 53–63.

[207] N. Simsek Ozek, S. Tuna, A.E. Erson-Bensan, F. Severcan, "Characterization of microRNA-125b expression in MCF7 breast cancer cells by ATR-FTIR spectroscopy", Analyst 135 (2010) 3094–3102.

[208] A. Dogan, G. Siyakus, F. Severcan, "FTIR spectroscopic characterization of irradiated hazelnut (Corylus avellana L.)", Food Chemistry 100 (2007) 1106–1114.

[209] S. Garip, F. Bozoglu, F. Severcan, "Differentiation of mesophilic and thermophilic bacteria with Fourier transform infrared spectroscopy", Applied Spectroscopy 61 (2007) 186–192.

[210] S. Garip, A. Cetin Gozen, F. Severcan, "Use of Fourier transform infrared spectroscopy for rapid comparative analysis of Bacillus and Micrococcus isolates", Food Chemistry 113 (2009) 1301–1307.

[211] Infrared Spectroscopy, http://www.umsl.edu/~orglab/documents/IR/IR2.html, last visited on 21st June 2011.

[212] F. Freund, R.M. Knobel, "Distribution of fluorine in hydroxyapatite studied by infrared spectroscopy", Journal of the Chemical Society 6 (1977) 1136–1140.

[213] J. Kneipp, M. Beekes, P. Lasch, D. Naumann, "Molecular changes of preclinical scrapie can be detected by infrared spectroscopy", Journal of Neuroscience 22 (2002) 2989–2997.

[214] Y.J. Kwon, K. H. Kim, C. S. Lim, K.B. Shim, "Characterization of ZnO nanopowders synthesized by the polymerized complex method via an organochemical route", Journal of Ceramic Processing Research 3 (2002) 146-149.

[215] A. Bandyopadhyay, S. Bernard, W. Xue, S. Bose, "Calcium phosphate-based resorbable ceramics: Influence of MgO, ZnO, and $SiO_2$ dopants", Journal of the American Ceramic Society 89 (2006) 2675–2688.

[216] O. Gunduz, E.M. Erkan, S. Daglilar, S. Salman, S. Agathopoulos, F.N. Oktar, "Composites of bovine hydroxyapatite (BHA) and ZnO", Journal of Materials Science 43 (2008) 2536–2540.

[217] Y. Ramaswamy, C. Wu, H. Zhou, H. Zreiqat, "Biological response of human bone cells to zinc-modified Ca–Si-based ceramics", Acta Biomaterialia 4 (2008) 1487–1497.

[218] B. Basar, A. Tezcaner, D. Keskin, Z. Evis, "Improvements in microstructural, mechanical, and biocompatibility properties of nano-sized hydroxyapatites doped with yttrium and fluoride", Ceramics International 36 (2010) 1633–1643.

[219] C. Ratisoontorn, M. L. Seto, K. M. Broughton, M. L. Cunningham, "In vitro differentiation profile of osteoblasts derived from patients with Saethre–Chotzen syndrome", Bone 36 (2005) 627– 634.

[220] H. Kim, E.Lee, H. Kim, V. Salih, J.C. Knowles, "Effect of fluoridation of hydroxyapatite in hydroxyapatite polycaprolactone composites on osteoblast activity", Biomaterials 26 (2005) 4395–4404.

[221] Y. Wang, S. Zhang, X. Zeng, L.L. Ma, W. Weng, W. Yan, M. Qian, "Osteoblastic cell response on fluoridated hydroxyapatite coatings", Acta Biomaterialia 3 (2007) 191–197.

[222] K. Cheng, W. Weng, H. Wang, S. Zhang, "In vitro behavior of osteoblast-like cells on fluoridated hydroxyapatite coatings", Biomaterials 26 (2005) 6288–6295.

[223] H. Kim, Y. Kong, J.C. Knowles, "Fluor-hydroxyapatite sol–gel coating on titanium substrate for hard tissue implants", Biomaterials 25 (2004) 3351–3358.

[224] H. Eslami, M. Solati-Hashjin, M. Tahriri, "Effect of fluorine ion addition on structural, thermal, mechanical, solubility and biocompatibility characteristics of hydroxyapatite nanopowders", Advances in Applied Ceramics 109 (2010) 200-212.

[225] A. Ito, M. Otsuka, H. Kawamura, M. Ikeuchi, H. Ohgushi, Y. Sogo, N. Ichinose, "Zinc-containing tricalcium phosphate and related materials for promoting bone formation", Current Applied Physics 5 (2005) 402–406.

[226] S. Miao, K. Cheng, W. Weng, P. Du, G. Shen, G. Han, W. Yan, S. Zhang, "Fabrication and evaluation of Zn containing fluoridated hydroxyapatite layer with Zn release ability", Acta Biomaterialia 4 (2008) 441–446.

[227] C. Ohtsuki, M. Kamitakahara, T. Miyazaki, "Coating bone-like apatite onto organic substrates using solutions mimicking body fluid", Journal Of Tissue Engineering and Regenerative Medicine 1 (2007) 33–38.

[228] W.F. Neuman, M.W. Neuman, "The Chemical Dynamics of Bone Minerals", University of Chicago Press, Chicago, IL (1958) 23–38.

[229] S.B. Cho, K. Nakanishi, T. Kokubo, N. Soga, C. Ohtsuki, T. Nakamura, T. Kitsugi, T. Yamamuro, "Dependence of apatite formation on silica gel on its structure: effect of heat treatment", Journal of the American Ceramic Society 78 (1995)1769–1774.

[230] P. Siriphannon, Y. Kameshima, A. Yasumor, K. Okada, S. Hayashi, "Formation of hydroxyapatite on $CaSiO_3$ powders in simulated body fluid", Journal of the European Ceramic Society 22 (2002) 511–520.

[231] Y. Iimori, Y. Kameshima, K. Okada, S. Hayashi, "Comparative study of apatite formation on $CaSiO_3$ ceramics in simulated body fluids with different carbonate concentrations", Journal of Materials Science: Materials in Medicine 16 (2005) 73–79.

[232] C. Wu, Y. Ramaswamy, A. Soeparto, H. Zreiqat, “Incorporation of Ti into calcium silicate improved their chemical stability and biological property”, Journal of Biomedical Materials Research A 86 (2008) 402-410.

[233] X. Liu, P. Chu, C. Ding, “Surface modification of titanium, titanium alloys, and related materials for biomedical applications”, Materials Science and Engineering: R: Reports 47 (2004) 49–121.

[234] X. Wei, O. Ugurlu, A. Ankit, H. Yagci Acar, M. Akinc, “Dissolution behavior of Si,Zn-codoped tricalcium phosphates”, Materials Science and Engineering C 29 (2009) 126–135.

[235] I. Mayer, J.D.B. Featherstone, “Dissolution studies of Zn-containing carbonated hydroxyapatites”, Journal of Crystal Growth 219 (2000) 98-101.

[236] L. Courtheoux, J. Lao, J.M. Nedelec, E. Jallot, “Controlled bioactivity in zinc-doped sol-gel-derived binary bioactive glasses”, Journal of Physical Chemistry C 112 (2008) 13663–13667.

[237] D.G.A. Nelson, J.D.B. Featherstone, J.F. Duncan, T.W. Cutress, “Paracrystalline disorder of biological and synthetic carbonate-substituted apatites”, Journal of Dental Research 61 (1982) 1274-1281.

[238] J.D.B. Featherstone, D.G.A. Nelson, “The effect of fluoride, zinc, strontium, magnesium and iron on the crystal-structural disorder in synthetic carbonated apatites”, Australian Journal of Chemistry 33 (1980) 2363-2368.

[239] Y. Sogo, A. Ito, D. Yokoyama, A. Yamazaki, R.Z. LeGeros, “Synthesis of fluoride releasing carbonate apatites for bone substitutes”, Journal of Materials Science: Materials in Medicine 18 (2007) 1001–1007.

[240] N. Rameshbabu, T.S. Sampath Kumar, K. Prasad Rao, “Synthesis of nanocrystalline fluorinated hydroxyapatite by microwave processing and its in vitro dissolution study”, Bulletin of Materials Science 29 (2006) 611-615.

## APPENDIX A

### CALIBRATON CURVE FOR ALP ACTIVITY ASSAY

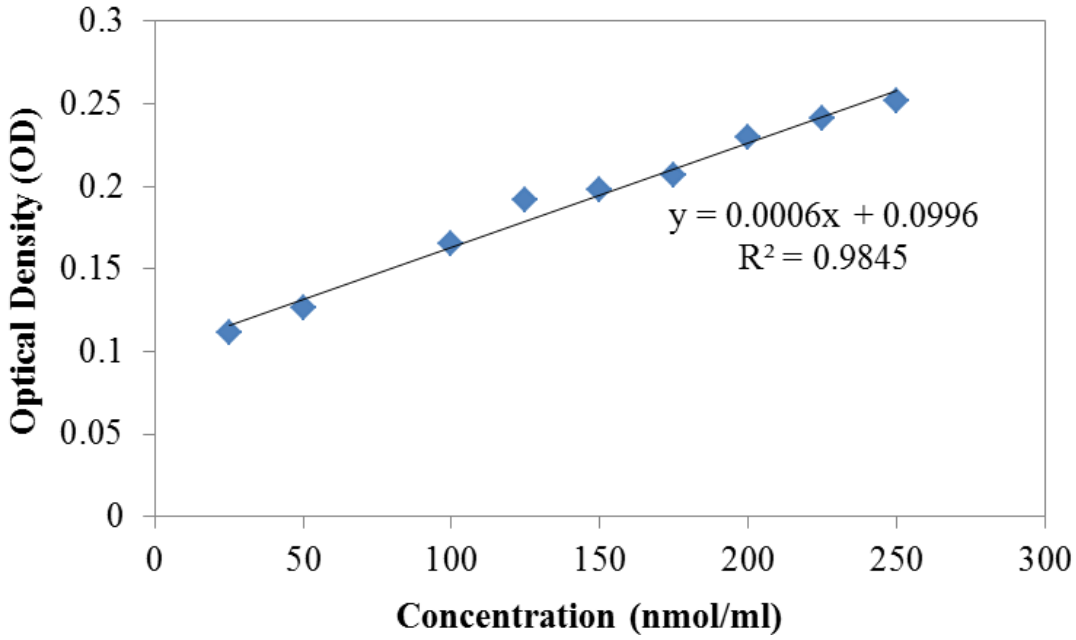


**Figure A.1.** The calibration curve of p-nitrophenol.

## APPENDIX B

## CALIBRATON CURVE FOR BCA ASSAY

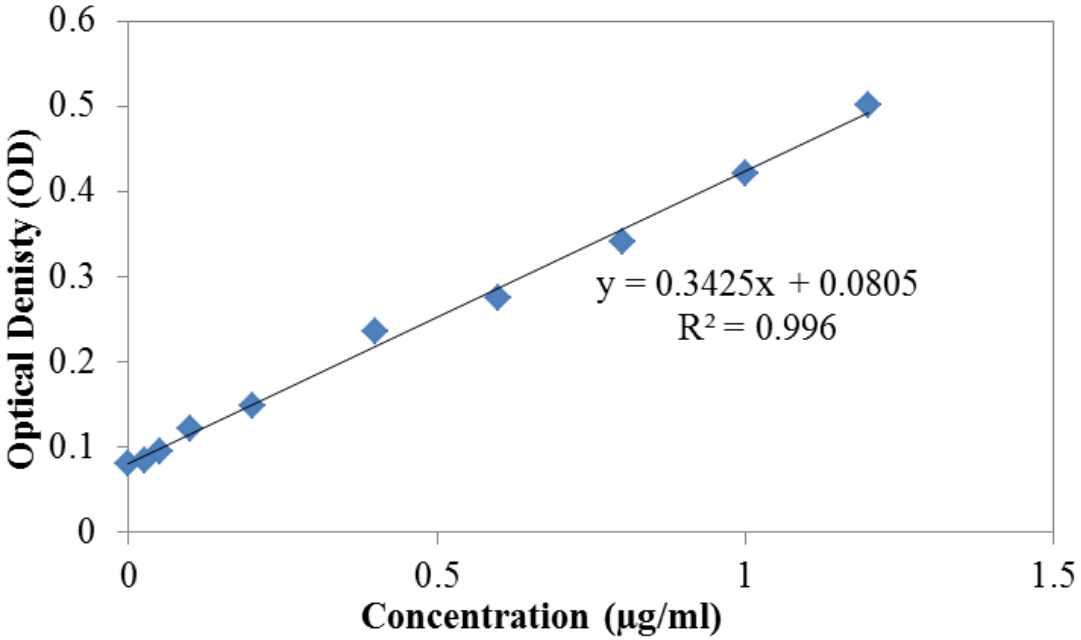


**Figure B.1.** The calibration curve of bovine serum albumin.